

PHASE CHANGE BEHAVIOUR OF LAURIC ACID IN A HORIZONTAL CYLINDRICAL LATENT HEAT ENERGY STORAGE SYSTEM

by

Chang Liu

Submitted in partial fulfilment of the requirements
for the degree of Master of Applied Science

at

Dalhousie University
Halifax, Nova Scotia
August 2012

© Copyright by Chang Liu, 2012

DALHOUSIE UNIVERSITY

DEPARTMENT OF MECHANICAL ENGINEERING

The undersigned hereby certify that they have read and recommend to the Faculty of Graduate Studies for acceptance a thesis entitled “Phase Change Behaviour of Lauric Acid in a Horizontal Cylindrical Latent Heat Energy Storage System” by Chang Liu in partial fulfilment of the requirements for the degree of Master of Applied Science.

Dated: August 13, 2012

Supervisor: _____

Readers: _____

DALHOUSIE UNIVERSITY

DATE: August 13, 2012

AUTHOR: Chang Liu

TITLE: Phase Change Behaviour of Lauric Acid in a Horizontal Cylindrical Latent Heat Energy Storage System

DEPARTMENT OR SCHOOL: Department of Mechanical Engineering

DEGREE: MASc CONVOCATION: October YEAR: 2012

Permission is herewith granted to Dalhousie University to circulate and to have copied for non-commercial purposes, at its discretion, the above title upon the request of individuals or institutions. I understand that my thesis will be electronically available to the public.

The author reserves other publication rights, and neither the thesis nor extensive extracts from it may be printed or otherwise reproduced without the author's written permission.

The author attests that permission has been obtained for the use of any copyrighted material appearing in the thesis (other than the brief excerpts requiring only proper acknowledgement in scholarly writing), and that all such use is clearly acknowledged.

Signature of Author

TABLE OF CONTENTS

LIST OF TABLES	viii
LIST OF FIGURES	ix
ABSTRACT	xv
LIST OF ABBREVIATIONS USED	xvi
ACKNOWLEDGEMENT	xvii
CHAPTER 1 : INTRODUCTION	1
1.1. Phase Change Materials.....	1
1.2. Various Geometries of Thermal Energy Storage Systems	5
1.2.1. Experimental Studies.....	5
1.2.2. Numerical Studies.....	10
1.3. Problem Statement.....	12
1.4. Scope of the Thesis.....	13
CHAPTER 2 EXPERIMENTAL PROCEDURES.....	14
2.1. Phase Change Material Selection	14
2.2. Heat Transfer Enhancement Technique	15
2.3. Experimental Setup.....	17
2.4. Procedure	21
2.5. Heat Transfer Fluid Properties	22
2.6. Experimental Uncertainty Analysis.....	22
2.6.1. Calibration of Probe Thermocouples	22
2.6.2. Method Description	23
2.6.3. Validation of Repeatability.....	25
2.6.4. Validation of Symmetry	25

2.6.5.	The Three-dimensional Effect	27
CHAPTER 3 EXPERIMENTAL RESULTS FOR STRAIGHT FIN		
CONFIGURATION.....		28
3.1.	Charging and Discharging of the PCM	28
3.1.1.	Charging	28
3.1.2.	Discharging.....	34
3.2.	Detailed Temperature Profiles.....	37
3.2.1.	Charging	37
3.2.2.	Discharging.....	39
3.2.3.	Solid-liquid Interface.....	41
3.3.	The Impact of HTF Inlet Temperature	42
3.4.	The Impact of HTF Flow Rates.....	47
3.4.1.	Charging	47
3.4.2.	Discharging.....	49
3.5.	Complete Charging and Discharging Time	52
3.6.	Thermal Response	54
3.7.	Energy Storage Capacity	55
3.7.1.	Theoretical Energy Storage	55
3.7.2.	Energy Supplied	56
3.7.3.	Heat Loss	56
3.7.4.	Experimental Uncertainty of Energy Stored	58
3.8.	Conclusion.....	59
CHAPTER 4 : NUMERICAL RESULTS FOR STRAIGHT FIN CONFIGURATION .		60
4.1.	Numerical Model Introduction	60
4.1.1.	Heat Conduction	61

4.1.2.	Natural Convection.....	61
4.1.3.	Phase Change Heat Transfer.....	62
4.1.4.	Boundary Conditions.....	63
4.1.5.	Mesh Convergence Study.....	66
4.2.	Numerical Results of Pure Conduction Models.....	69
4.2.1.	Numerical Results of Melting With Pure Conduction.....	69
4.2.2.	Numerical Results of Solidification with Pure Convection.....	72
4.3.	Numerical Results with Convection.....	73
4.3.1.	Numerical Results of Charging with Convection.....	74
4.3.2.	Numerical Results of Discharging.....	76
4.4.	Conclusion.....	79
CHAPTER 5 : EXPERIMENTAL AND NUMERICAL RESULTS FOR ANGLED FIN CONFIGURATION		80
5.1.	Detailed Temperature Profiles.....	80
5.1.1.	Charging	80
5.1.2.	Discharging.....	85
5.2.	Comparison with Straight Fins.....	85
5.3.	Numerical Results with Pure Conduction	87
5.4.	Conclusion.....	90
CHAPTER 6 : CONCLUSION AND RECOMMENDATIONS		91
6.1.	Conclusion.....	91
6.2.	Recommendations	93
REFERENCE.....		94
APPENDIX A CALIBRATIONS OF PROBE THERMOCOUPLES.....		101
APPENDIX B FLOWMETER ELECTRICAL CIRCUIT CONNECTING DIAGRAM		104

APPENDIX C EXAMPLE OF EXPERIMENTAL UNCERTAINTY OF ENERGY STORED	105
APPENDIX D PHOTOGRAPHS OF CHARGING AND DISCHARGING	106

LIST OF TABLES

Table 2.1: Thermophysical Properties of Lauric Acid (Yaws, 2003; Alfa Aesar)	15
Table 2.2: Properties of Water (Xydatasource; Incropera et al. 2005)	22
Table 2.3: Maximum uncertainties for experimental data	24
Table 3.1: Power output during discharging.....	55
Table 4.1: Heat transfer coefficients for charging	65
Table 4.2: Heat transfer coefficients for discharging.....	66
Table A.1: Calibration results of 10°C bath temperature	101
Table A.2: Calibration results of 20°C bath temperature	101
Table A.3: Calibration results of 30°C bath temperature	102
Table A.4: Calibration results of 40°C bath temperature	102
Table A.5: Calibration results of 50°C bath temperature	103
Table A.6: Calibration results of 60°C bath temperature	103

LIST OF FIGURES

Figure 1.1 Classification of phase change materials (Based upon Sharma et al., 2009)	2
Figure 2.1: DSC curve for lauric acid (Desgrosseilliers et al., 2011)	14
Figure 2.2: Orientations of longitudinal fins: a) straight fins; b) angled fins	16
Figure 2.3: Copper longitudinal fins added into lauric acid	16
Figure 2.4: Schematic of the experimental setup	17
Figure 2.5: The PCM Container with longitudinal copper fins	18
Figure 2.6: The positions of probe thermocouples	18
Figure 2.7: The positions of surface thermocouples	19
Figure 2.8: a) An example of attachable thermocouple; b) The compactDAQ data acquisition system	20
Figure 2.9: a) The flow meter from Omega (model FTB 4605); b) The constant water bath; c) The centrifugal pump from Grundfos; d) The insulation of the PCM container	20
Figure 2.10: Hart Scientific Model 7102 micro-bath	23
Figure 2.11: Validation of repeatability (HTF inlet temperature of 60°C, HTF flow rate 1L/min)	25
Figure 2.12: Validation of symmetry (HTF inlet temperature of 60°C, HTF flow rate 1L/min)	26
Figure 2.13: Validation of symmetry after 2 hours of charging (HTF inlet temperature 60°C, HTF flow rate 1L/min)	26
Figure 2.14: The attachable thermocouple temperature profile	27
Figure 3.1: Temperature profiles of T10 to T14 at a HTF inlet temperature of 50°C and HTF flow rate of 1L/min	29
Figure 3.2: Temperature profiles of T10 to T14 at a HTF inlet temperature of 50°C and HTF flow rate of 3.5L/min	29
Figure 3.3: Temperature profiles of T10 to T14 at a HTF inlet temperature of 50°C and HTF flow rate of 5.5L/min	30
Figure 3.4: Temperature profiles of T10 to T14 at a HTF inlet temperature of 55°C and HTF flow rate of 1L/min	31

Figure 3.5: Temperature profiles of T10 toT14 at a HTF inlet temperature of 55°C and HTF flow rate of 3.5L/min.....	31
Figure 3.6: Temperature profiles of T10 toT14 at a HTF inlet temperature of 55°C and HTF flow rate of 5.5L/min.....	32
Figure 3.7: Temperature profiles of T10 toT14 at a HTF inlet temperature of 60°C and HTF flow rate of 1L/min.....	33
Figure 3.8: Temperature profiles of T10 toT14 at a HTF inlet temperature of 60°C and HTF flow rate of 3.5L/min.....	33
Figure 3.9: Temperature profiles of T10 toT14 at a HTF inlet temperature of 60°C and HTF flow rate of 5.5L/min.....	34
Figure 3.10: Temperature profiles of T10 toT14 at a HTF inlet temperature of 9°C and HTF flow rate of 1.5L/min.....	35
Figure 3.11: Temperature profiles of T10 toT14 at a HTF inlet temperature of 9°C and HTF flow rate of 6.5L/min.....	36
Figure 3.12: Temperature profiles of T10 toT14 at a HTF inlet temperature of 9°C and HTF flow rate of 13L/min.....	36
Figure 3.13: Temperature profiles of higher quadrants at a HTF inlet temperature of 60°C and HTF flow rate of 1L/min	37
Figure 3.14: Temperature profiles of lower quadrants at a HTF inlet temperature of 60°C and HTF flow rate of 1L/min	38
Figure 3.15: Representation of the heat transfer enhancement by the fins as a function of the quadrant	39
Figure 3.16: Temperature profiles of higher quadrants at a HTF inlet temperature of 9°C and HTF flow rate of 8L/min	40
Figure 3.17: Temperature profiles of lower quadrants at a HTF inlet temperature of 9°C and HTF flow rate of 8L/min	40
Figure 3.18: Solid-liquid interface location during a) charging with a HTF inlet temperature 60°C, HTF flow rate 1L/min; b) discharging with a HTF inlet temperature 9°C, HTF flow rate 8L/min	42
Figure 3.19: HTF inlet temperature effect on T12 and T14 (50°C_1/min, 55°C_1L/min and 60°C_1/min).....	44

Figure 3.20: HTF inlet temperature effect on T11 and T13 (50°C_1/min, 55°C_1L/min and 60°C_1L/min)	44
Figure 3.21: HTF inlet temperature effect on T12 and T14 (50°C_3.5/min, 55°C_3.5 L/min and 60°C_3.5/min)	45
Figure 3.22: HTF inlet temperature effect on T11 and T13 (50°C_3.5/min, 55°C_3.5 L/min and 60°C_3.5/min)	46
Figure 3.23: HTF inlet temperature effect on T12 and T14 (50°C_5.5/min, 55°C_5.5 L/min and 60°C_5.5/min)	46
Figure 3.24: HTF inlet temperature effect on T11 and T13 (50°C_5.5/min, 55°C_5.5 L/min and 60°C_5.5/min)	47
Figure 3.25: HTF flow rate effect at T11 and T12 (55°C_1 L/min, 55°C_3.5 L/min and 55°C_5.5 L/min)	48
Figure 3.26: HTF flow rate effect at T13 and T14 (55°C_1 L/min, 55°C_3.5 L/min and 55°C_5.5 L/min)	49
Figure 3.27: HTF flow rate effect on T11 and T12	50
Figure 3.28: HTF flow rate effect on T11 and T13 (9°C_1 L/min, 9°C_6.5 L/min and 9°C_11.5 L/min)	51
Figure 3.29: HTF flow rate effect on T12 and T14 (9°C_1 L/min, 9°C_6.5 L/min and 9°C_11.5 L/min)	51
Figure 3.30: Melting time for various HTF inlet temperatures at different HTF flow rates	52
Figure 3.31: Solidification time for different HTF flow rates	53
Figure 3.32: Thermal responses for charging with a HTF inlet temperature of 55°C and HTF flow rate of 1 L/min, discharging with a HTF inlet temperature of 9°C and HTF flow rate of 11.5 L/min.....	54
Figure 3.33 Maximum heat storage capacities for various HTF inlet temperatures.....	56
Figure 3.34: Energy supplied, stored and heat loss at a HTF inlet temperature of 60°C, HTF flow rate 1 L/min.....	58
Figure 3.35: Uncertainty of energy stored with a HTF inlet temperature at 60°C, HTF flow rate 1 L/min	59
Figure 4.1: Geometry of the numerical model.....	60

Figure 4.2: Dynamic viscosity of lauric acid in numerical models	62
Figure 4.3: The specific heat of lauric acid in numerical models	63
Figure 4.4: Temperature profile of T11 with different amount of elements (simulation of pure conduction test with a HTF inlet temperature of 60°C and flow rate of 1 L/min)	67
Figure 4.5: Melting fraction of the PCM as a function of time for different amount of elements(simulation of pure conduction test with a HTF inlet temperature of 60°C and flow rate of 1 L/min)	68
Figure 4.6: Final mapped mesh of numerical model which consists of 4416 elements ...	68
Figure 4.7: The comparison of experimental and numerical temperature profiles during charging for T11 and T12 (HTF inlet temperature of 60°C, HTF flow rate of 1 L/min)	70
Figure 4.8: The comparison of experimental and numerical temperature profiles during charging for T13 and T14 (HTF inlet temperature of 60°C, HTF flow rate of 1 L/min)	71
Figure 4.9: The comparison of experimental and numerical temperature profiles during discharging for T11 and T12 (HTF inlet temperature of 9°C, HTF flow rate of 8 L/min)	72
Figure 4.10: The comparison of experimental and numerical temperature profiles during discharging for T13 and T14 (HTF inlet temperature of 9°C, HTF flow rate of 8 L/min)	73
Figure 4.11: The numerical temperature plots during charging for the straight fin configuration accounting for convection (HTF inlet temperature of 60°C, HTF flow rate of 1 L/min)	74
Figure 4.12: The comparison of temperature profiles between experimental and numerical results during charging (HTF inlet temperature of 60°C, HTF flow rate of 1 L/min)	76
Figure 4.13: The numerical temperature plots during solidification for the straight fin configuration accounting for convection (HTF inlet temperature of 9°C, HTF flow rate of 8 L/min)	77

Figure 4.14: The comparison of temperature profiles between experimental and numerical results during discharging (HTF inlet temperature of 9°C, HTF flow rate of 8 L/min)	78
Figure 5.1: The angled fins orientation.....	80
Figure 5.2: Temperature profiles of T10 toT14 at a HTF inlet temperature of 50°C and HTF flow rate of 1 L/min.....	81
Figure 5.3: Temperature profiles of T10 toT14 at a HTF inlet temperature of 50°C and HTF flow rate of 1 L/min.....	81
Figure 5.4: Temperature profiles of T10 toT14 at a HTF inlet temperature of 50°C and HTF flow rate of 1 L/min.....	82
Figure 5.5: Temperature profiles of T10 toT14 at a HTF inlet temperature of 50°C and HTF flow rate of 1 L/min.....	83
Figure 5.6: Temperature profiles of T10 toT14 at a HTF inlet temperature of 50°C and HTF flow rate of 1 L/min.....	84
Figure 5.7: Temperature profiles of T10 toT14 at a HTF inlet temperature of 50°C and HTF flow rate of 1 L/min.....	84
Figure 5.8: HTF flow rates effect on temperature profiles of T11-T14.....	85
Figure 5.9: Melting time comparison between straight fins and angled fins.....	86
Figure 5.10: Discharging time comparison between straight fins and angled fins.....	87
Figure 5.11: The comparison of experimental and numerical temperature profiles of T11 and T12 (charging)	88
Figure 5.12: The comparison of experimental and numerical temperature profiles of T13 and T14 (charging)	88
Figure 5.13: The comparison of experimental and numerical temperature profile of T11 to T14 (discharging)	89
Figure B.1: Diagram of the electrical circuit connecting flowmeter to DAQ system	104
Figure D.1: Photos taken during charging with a HTF inlet temperature of 60°C and HTF flow rate of 5.5L/min.....	106
Figure D.2: Photos taken during discharging with a HTF inlet temperature of 9°C and HTF flow rate of 13L/min.....	107

Figure D.3: Photos taken during discharging with a HTF inlet temperature of 9°C and HTF flow rate of 13L/min (continued)	108
---	-----

ABSTRACT

This work presents an experimental and numerical study of phase change behaviour in a horizontal cylindrical latent heat energy storage system (LHESS). Fins with two orientations, straight fins and angled fins, are added into the PCM to enhance heat transfer. The PCM used in this study is lauric acid which has desirable thermal properties for LHESS.

The experimental work concentrates on studying the heat transfer mechanism during phase change, impacts of the HTF inlet temperature and HTF flow rates. Moreover, heat transfer enhancement effectiveness of straight fins and angles fins is compared. Numerical model is simulated using COMSOL Multiphysics software package.

It is observed that conduction is the dominant heat transfer mechanism during the initial stage of charging, and natural convection plays a more important role afterwards. Conduction plays a major role during solidification. Complete melting time is affected by the HTF inlet temperature and HTF flow rates.

LIST OF ABBREVIATIONS USED

C_p	Heat capacity ($\text{J kg}^{-1}\text{K}^{-1}$)
D	Diameter (m)
g	Acceleration of gravity (m s^{-2})
h	Heat transfer coefficient ($\text{W m}^{-2}\text{K}^{-1}$)
k	Thermal conductivity ($\text{W m}^{-1}\text{K}^{-1}$)
L	Latent heat of fusion (J kg^{-1})
m	Mass (kg)
Q	Energy stored (J)
r	Radius (m)
T	Temperature ($^{\circ}\text{C}$)
t	Time (hours)
A	Area
V	Volume (m^3)
f	Friction factor
q''	Heat flux (W m^{-2})

Greek symbols

α	Thermal diffusivity (m^2s^{-1})
ΔT	Temperature difference ($^{\circ}\text{C}$)
μ	Dynamic viscosity (N s m^{-2})
ρ	Density (kg m^{-3})

Subscripts

f	Final
i	Initial
l	Latent
l	Liquid
in	Inlet
out	Outlet
n	Number
m	Melting
pcm	Phase change material
s	Sensible
s	Solid
T	Total
pl	Liquid phase
ps	Solid phase

Definitions of non-dimensional variables

Nu	Nusselt number (hD/k)
Pr	Prandtl number ($C_p\mu/k$)
Re	Reynold number ($\rho uD/\mu$)
Ste	Stefan number ($C_p\Delta T/L$)

ACKNOWLEDGEMENT

I would first like to thank my supervisor, Professor Dominic Groulx, who was always ready to help me. This thesis would not have been accomplished without his kindness, direction and support. Professor Groulx did not only guide me to complete my thesis, but also inspired me in so many ways. He is a dedicated supervisor and role model to us.

I wish to gratefully acknowledge the suggestion and encouragement of Professor Michael J. Pegg and Professor Lukas Swan, who provided valuable help for completing this thesis. I would also like to thank the Department of Mechanical Engineering for their excellent education.

My special thanks also go to members of LAMTE, Benjamin Sponagle, Robynne Murray, Louis Desgrosseilliers, and Farid Samara. It is an honor for me to work with such a great team.

I owe a particular debt of gratitude to my respectful parents, who I love the most in the world. The care, patience and love from my parents help me go through every challenge in life.

CHAPTER 1 : INTRODUCTION

Thermal energy storage (TES) has attracted research attention because of its application in bridging the gap between energy supply and demand in solar thermal systems (Lacroix et al., 1998; Banaszek et al., 1999; Sari et al., 2003; Liu et al., 2006). Current thermal energy storage systems can be categorized by the method they use to store energy such as sensible heat storage, latent heat storage and thermochemical heat storage (Abhat, 1983). Among all these energy storage methods, latent heat thermal energy storage systems show more potential due to their advantages of high energy storage density and almost constant temperature during phase change (Agyenim et al., 2010).

TES has been a main topic in research for the last 20 years. Experimental and numerical studies have been conducted focusing on thermal behaviour of phase change materials (PCMs), melting and solidification of PCMs, PCM containers, and convective heat transfer problems within PCMs. Zalba et al. (2003) reviewed the history of latent heat energy storage system (LHESS) including PCMs, the heat transfer mechanism and applications. Sharma et al. (2009) summarized the investigations of available TES systems focusing on thermal properties of various PCMs. Comprehensive information of TES systems and applications can be found in Dincer and Rosen's 2002 book.

Latent heat energy storage system (LHESS) uses phase change material as the energy storage medium: energy is stored during melting and released during solidification. Various applications are found in the open literature in the area of space heating (Halawa et al., 2010), space cooling (Badescu, 2003), domestic hot water systems (Stritih, 2003) and incorporating PCMs into building elements (Athienitis et al., 1997; Lee et al., 2000; Neeper, 2000; Pasupathy et al., 2008).

1.1. Phase Change Materials

LHESS makes use of the energy absorbed or released as a material changes phase. The energy stored is given by the following equation (Lane, 1983):

$$Q = \int_{T_i}^{T_m} mC_{ps}dT + ma_m\Delta h_m + \int_{T_m}^{T_f} mC_{pl}dT \quad (1.1)$$

Where Q is the energy stored (J), m is the mass of the PCM (kg), T is temperature, C_p is the specific heat of PCM, a_m is the PCM melted fraction, and Δh_m is the latent heat of fusion (J/kg).

The substance used in a LHES which is capable of storing and releasing a large amount of energy is the PCM. The selection of a proper PCM for a certain system should be done carefully, and the compromise between PCM melting temperature and practical temperature range of the designed system should be taken into account (Agyenim et al., 2010). Most of the research on PCM problems has been carried out within the temperature range of 0-65°C which is suitable for domestic heating and cooling (Agyenim et al., 2010).

Classification of PCMs

Abhat (1983) divided PCMs into three categories: organic, inorganic and eutectics. Sharma et al. (2009) extended Abhat's division with subcategories as shown in Fig 1.1.

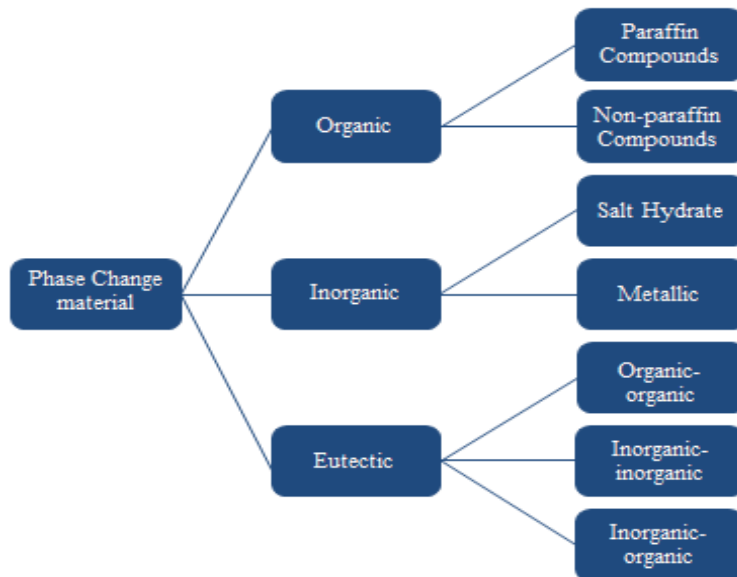


Figure 1.1 Classification of phase change materials (Based upon Sharma et al., 2009)

Paraffin Wax

Organic PCMs are generally chemically stable, melt congruently, do not suffer from supercooling, and are non-toxic with a high latent heat of fusion. Comparing with inorganic PCMs, organic PCMs have lower corrosiveness and higher stability which make them more suitable for industry applications, for instance, incorporating organic PCMs into building materials. Therefore, organic PCMs have been the focus of research in this field. They can be

further divided into paraffin and non-paraffin among which paraffin wax is the most widely studied and used (Zhang et al., 2006). Paraffin waxes are a family of straight chain alkanes. Their melting temperature and latent heat increase with the hydrocarbon chain length for various paraffin waxes (Kousksou et al., 2010).

However, paraffin wax has several disadvantages which are: moderately flammability, low thermal conductivity and may leak in liquid phase which limits its wide application in industry. In addition, it shows a tendency to infiltrate and soften some types of plastics which should be taken into account if a plastic container is proposed (Lane, 1983).

Non-paraffin PCMs

Non-paraffin organic PCMs consist of fatty acids, esters, alcohols and glycols (Hasnain, 1998). Among them, fatty acids are promising because of their applications in solar thermal systems (Feldman et al., 1989; Sari et al., 2003; Alkan et al., 2008). The most commonly used fatty acids are divided into six groups: caprylic, capric, lauric, myristic, palmitic and stearic with respectively 8 to 18 carbon atoms per molecule. Their melting points are in the range from 16°C and 65°C and freezing points between 17°C and 64°C, with a heat of fusion between 155 and 180 kJ/kg which is higher than paraffin waxes (Baetens et al., 2010).

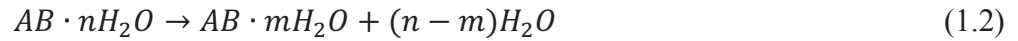
Thermal and physical properties of Glauber's salt and lauric acid were investigated by the Lab of Applied Multiphase Thermal Engineering of Dalhousie University (Desgrosseillier et al., 2011). Differential scanning calorimetry (DSC) curves were obtained and results proved lauric acid as a promising candidate for LHESS. Selected fatty acids, including stearic, palmitic, myristic and lauric acid were tested by Sari and co-workers (Sari et al., 2002; Sari et al., 2003; Sari et al., 2009). It was concluded that all fatty acids investigated in their experiments had shown good thermal stability which qualified them as PCMs for LHESS (Sari et al., 2003).

The main drawback of fatty acids which limits their application in solar thermal systems is their high cost, almost three times higher compared with paraffin wax (Alkan et al., 2008). One possible solution to this economic problem is encapsulating fatty acids into a supporting material

such as poly methyl methacrylate (Alkan et al., 2008). This technique decreased system volume, and the cost of the whole LHESS is consequently reduced.

Salt Hydrates

The most reviewed inorganic PCMs are salt hydrates. Salt hydrates are crystalline mixtures of water and inorganic salts, generally in the form of $AB \cdot nH_2O$. Melting salt hydrates usually involves two forms of reaction:



Which means salt hydrates usually either melts to a salt hydrate with fewer moles of water or into a salt and water (Sharma et al., 2009). For a comprehensive review of hydrated salts, one can consult the first chapter of Lane's book (1983) in which a wide range of melting temperature of various hydrated salts can be found.

Hydrated salts have many advantages including high latent heat of fusion, high thermal conductivity compared to paraffin waxes, small volume change during phase change, and are compatible with plastics (Sharma et al., 2009). However, the major problem of using hydrated salts as PCM is incongruent melting. This disadvantage reduces the suitability of hydrated salts for repeatable thermal cycles as PCM (Sharma et al., 2009). Most hydrated salts also suffer from supercooling problems, to which a possible solution is embedding a nucleating agent.

Detection of Solid-liquid Interface

During phase change in LHESS, the solid-liquid interface location needs to be monitored in order to determine the melting time and molten fractions. There have been several ways provided to monitor this solid-liquid interface. Direct visualization can be used when the PCM has optical clarity in the molten state such as *n*-eicosane (Jones et al., 2006). A photographic record was employed by Bathelt et al. (1980) during the melting of *n*-octadecane which was electrically heated by a horizontal cylindrical heat source.

There are also indirect methods available. Campbell et al. (1994) employed a real-time radioscopy method to study the melting and solidification of gallium. A more commonly adopted technique is inserting thermocouples into PCM and detecting the solid-liquid interface according to specific melting temperature of the PCM used in the system (Wang et al., 1999; Cho et al., 2000; Jones et al., 2006; Akgun et al., 2008; Bedecarrats et al., 2009; Baran et al., 2003).

1.2. Various Geometries of Thermal Energy Storage Systems

For the purpose of long-term thermal stabilities of TES, the size of the PCM container should be designed properly, for instance, corresponding to a typical eight-hour daytime charging mode. In that case, the certain amount of PCM stored in the container starts to melt in the morning and should achieve complete melting at the end of the afternoon so as to get maximum effectiveness of the LHESS system (Zivkovic and Fuji, 2003). Regarding the corrosive characteristic of a particular PCM, the material of the PCM container also needs to be carefully selected. For example, paraffin is compatible with most metals but have a tendency to soften some plastics (Dincer and Rosen, 2011).

In this literature review, experimental and numerical works on three main geometries of LHESS are analyzed: rectangular, cylindrical, and spherical.

1.2.1. Experimental Studies

Rectangular Geometry

The role of convection on close contact melting on a heated plate was investigated by Groulx and Lacroix (2007) and it was found that convection could reduce the melting rate by decreasing heat flux at the phase change interface.

Rectangular PCM containers are also used in building products which is an effective way to enhance thermal energy storage capacity of buildings. It was noted that PCM gypsum board used in a passive solar building can lead to a lower heating load and reduce maximum room temperature by approximately 4°C during the daytime (Athienitis et al., 1997). The thermal energy storage capacity of a wallboard with mixed PCMs showed twelve times higher

effectiveness than plain wallboard in a 3.5°C temperature interval (Feldman et al., 1995). Concrete incorporated with PCM successfully shifted heating and cooling load away from peak demand periods which resulted in a reduction in cost (Lee et al., 2000).

Another example of rectangular enclosure was a PCM-filled wall heated from the vertical side (Wang et al., 1999). It was noted that conduction was the dominant mechanism of heat transfer at the initial stage. As the melting progressed, the melting rate of the PCM (polyethylene glycol) on the top was faster than in the bottom. The reason of this phenomenon was a flow caused by buoyancy effect which also indicated convection played a role in the heat transfer process (Wang et al., 1999).

Inclined rectangular enclosure containing PCM was studied by Webb et al. (1986) and a three-dimensional flow pattern was detected. It was also found that the flow pattern was dependent on the inclined angle. The three-dimensional natural convective motion resulted in a higher melting rate because of more rapid energy transport to the phase change interface compared with the two-dimensional boundary layer (Webb et al., 1986).

Horizontal Cylindrical Geometry

Applications of LHESS using horizontal cylindrical systems can be found in solar water heater and electric cooling areas (Weng et al., 2010; Agyenim et al., 2009). Utility of PCM (tricosane) in an electronic cooling system can reduce by 46% the fan power consumption, compared with test systems without PCMs (Weng et al., 2010). The shape of solid-liquid interface of melting naphthalene was explored by Goldstein and Ramsy (1979) using a horizontal cylindrical heater. It was found that after the initial stage when pure conduction was the only heat transfer mechanism, the melted region was significantly thicker above the heater. A high heat flux rate was observed above the cylinder with an impinging plume.

Close contact melting and natural convection in a horizontal cylindrical capsule were experimentally studied by Saitoh and Kato (1993). It was shown that the contribution of close-contact heat transfer was reduced as Stefan number increased. Meanwhile, the natural convection effect in the melt region becomes more significant (Saitoh and Kato, 1993).

Employing multiple PCMs in LHEES system has been reported as an attractive heat transfer enhancement technique. The thermal conductivity of the PCM mixture can be increased by adding PCMs with higher thermal conductivity. Tetradecane, hexadecane and their binary mixtures proved to be excellent PCM candidates for district cooling (He et al., 2002; Kousksou et al., 2010).

Vertical Cylindrical Geometry

In vertical LHESS systems, better stability of PCM (myristic acid) was achieved in the radial direction rather than the axial direction (Sari et al., 2001). In addition, low inlet temperature of the heat transfer fluid (HTF) (water in this case) could increase the stability of PCM compared with the high inlet temperature of HTF (Sari et al., 2001). Kalaiselvam et al. (2008) noted that higher Stefan number results in rapid solidification. LHESS could be operated in three modes: charging only, discharging only and simultaneous charging/discharging modes. It was reported that combined operation was more feasible and practical for a heat pipe heat exchanger with latent heat storage (Liu et al., 2006).

Thermal characteristics of different PCMs have been investigated in vertical cylindrical LHESS. A technical grade paraffin wax, Rubitherm, was found to melt congruently, freeze without supercooling, and keep good stability after a number of charge and discharge cycles (He et al., 2002). Three paraffins were investigated in a cylindrical enclosure, namely *n*-tetradecane, *n*-pentadecane, a mixture of 60% *n*-tetradecane and 40% *n*-hexadecane. It was concluded that total solidification time depended on the Stefan number. Higher Stefan number led to rapid solidification and higher melting rates (Kalaiselvam et al., 2008). Apart from paraffin waxes, eutectic mixture was also tested in vertical cylindrical LHESS. A eutectic mixture of palmitic and stearic acids as PCM was proved to be a good PCM candidate in a two concentric vertical LHESS (Baran et al., 2003).

Not only does the geometry of the PCM container affect thermal storage performance, but also choosing a proper orientation of the PCM container is important. It was observed that the melting time of PCM (palmitic acid) can be reduced significantly by placing the PCM container in a

horizontal position rather than vertical (Hasan, 1994). Economic factors should be taken into account in LHESS design. Incorporating Rubitherm as PCM in energy storage tank helped reduce the initial capital cost, as well as increasing the cooling capacity of the existing system (He et al., 2002).

In order to enhance heat transfer rate, more complicated vertical LHESS were investigated. A spiral LHESS unit with paraffin wax PPW-20 as PCM was investigated; turbulence and centrifugal forces resulting from this geometry effectively enhanced heat transfer between PCM and air (Banaszek et al., 1999). Moreover, a packed bed column energy storage system was also reported to be efficient using small particle of granular phase change composites as PCM (Rady, 2009).

Spherical Geometry

Spherical geometry is preferred in encapsulation of PCMs in LHESS. The advantage of PCM encapsulation is twofold: the heat transfer area is increased and ease of packing into storage tanks (Chan et al., 2006; Eames et al., 2002).

In spherical enclosure, close contact melting was detected during the solid-liquid phase change (Assis et al., 2007). It was also found that decreasing the surface temperature of the PCM container and increasing the HTF flow rate would result in a larger solidified mass fraction of PCM (Chan et al., 2006; Bedecarrats et al., 2009). It was noted by Cho and Choi (2000) that the temperature of inlet heat transfer fluid could affect overall thermal performance of spherical LHESS. Moreover, to solve the problem of liquid leakage of paraffin waxes, Ye et al. (2000) performed a study of form-stable PCM called polyethylene paraffin compound which consisted of paraffin and a high density polyethylene as a supporting material. The mixture was found to be a proper candidate for LHESS in a low temperature range.

Spherical LHESS also has applications in cold energy storage; different PCMs for cold storage were investigated by Ismail et al. (2009). The PCMs employed were mixtures of water and various concentration of glycol. It was noted that increasing the glycol content in the PCM led to longer solidification time for all working temperatures. Moreover, increasing the diameter of the

spherical shell was also found to increase the PCM solidification time. Furthermore, Eames et al. (2002) studied the use of water as PCM in spherical enclosures in cooling systems of buildings. A novel method to measure the water-ice interface during freezing was described in this work. Horizontal systems combined with PCM encapsulation provide a promising way to enhance thermal conductivity of PCM. It was reported that the melting fraction of PCM (paraffin wax) was higher in smaller capsule. The reason is that it possessed thinner molten layers which lead to smaller thermal resistance (Regin et al., 2008).

Heat Transfer Enhancement Techniques

From quantities of studies subject to PCMs in LHESS, it is found that PCM shows great potential in improving the thermal capacity of TES. However, it is also observed that PCMs have relatively low thermal conductivity which reduces charging and discharging rate. In order to increase the heat transfer rate, heat transfer enhancement techniques are required in most systems. Taking paraffin waxes as an example, several attempts have been made focusing on increasing heat transfer areas of LHESS. For example, inserting metal matrix and other forms of metal structures into paraffin waxes lead to a significant enhancement of heat transfer rate. Besides, wrapping PCMs with spherical capsules is also an effective way to enhance heat transfer in LHESS (Tong et al., 1996; Ettouney et al., 2004; Ettouney et al., 2006; Ye et al., 2000).

As a common heat transfer enhancement technique, adding fins to LHESS has been studied by many researchers. It was observed that the shape of the fin had an effect on the performance of heat transfer enhancement. In a concentric tube heat exchanger with Erythritol as PCM, a longitudinal finned system was recommended rather than a circular finned system (Agyenim et al., 2009). Three reasons accounted for this conclusion: longitudinal fins possessed better charge performance, less supercooling, and a shorter melting time (Agyenim et al., 2009). Moreover, fins with thin walled hollow cylindrical steel structures and with bubble agitation were tested respectively to study heat transfer enhancement effect and results showed that both of them could improve thermal performance (Velraj et al., 1999). Other parameters of fins were also studied both numerically and experimentally. It was reported by Ismail et al. (2000) that fin thickness had a relatively small influence on the solidification time; while fin length and the number of fins strongly affected the complete solidification time.

Furthermore, it was noted that heat transfer rate was increased by embedding an aluminum matrix in LHESS in which paraffin wax was used as the PCM (Tong et al., 1996). It was also noted that Nusselt number was tripled by submerging metal screens and metal spheres in the PCM in a double pipe LHESS (Ettouney et al., 2004). The trade-off of the system was a 2% reduction of the total thermal load.

1.2.2. Numerical Studies

Predicting the behaviour of phase change is difficult because of the inherent non-linear nature at moving interfaces (Dutil et al., 2011). Three sets of numerical solutions to LHESS were summarized by Dutil et al. (2011): namely fixed grid; adaptive mesh; and first law and second law of thermodynamics method.

Rectangular Geometry and Spherical Geometry

Numerical studies of rectangular LHESS could be divided into two categories: heat transferred from below and heat transferred from the side of the system (Ho et al., 1996; Zivkovic et al. 2003; Gong et al., 1998; Sarris et al., 2004).

Free and forced convection have gained research attention in numerical studies of LHESS. Hamdan et al. (1996) reported a numerical study of heat transfer in a rectangular enclosure heated from one side. Within the melted region, the dominant mode of heat transfer was found to be convection. However, in the area very close to the solid surface at the bottom, convection can be neglected as conduction is the dominant mode.

A finite element method combined with a fixed grid primitive method was used to explore convection-dominated melting in a rectangular cavity heated from below (Gong et al., 1998). It was concluded that the heat transfer rate can be improved significantly by inverting the PCM container at an appropriate stage in the melting process (Gong et al., 1998). The Rayleigh number and Stefan number had effects on the heat transfer enhancement in Gong's study. In Sarris et al. (2004) study, an energy storage tank with PCM heated by a strip from below was investigated numerically. It was reported that the Rayleigh number had a significant effect of on

heat transfer and the Nusselt number was expressed as a function of Rayleigh number, heated strip width to tank length ratio, and tank aspect ratio (Sarris et al., 2004).

Moreover, the finite difference method was also applied for numerical study of LHESS. It was found that the geometry of a shallow rectangular composite cell was suitable for effective thermal protection applications (Ho et al., 1996).

Several researchers have investigated LHESS in spherical geometry numerically. Benmansour et al. (2006) developed a two-dimensional separate phase formulation in a numerical analysis of a cylindrical packed bed LHESS. Veerappan et al. (2009) investigated the phase change behaviour of a PCM mixture inside spherical enclosures to identify a suitable thermal storage material. Ismail and Henriquez (2000) presented a numerical study of the solidification of PCM enclosed in a spherical shell. It was found that increasing the diameter of the spherical shell led to a longer solidification time.

Cylindrical Geometry

Compared with rectangular geometry, a cylindrical PCM container might be less efficient under certain circumstances. A mathematical model based on an enthalpy formulation was developed by Zivkovic et al. (2001). It was found that the cylindrical container required almost double the melting time compare by a rectangular container, which had the same volume and heat transfer area. It was suggested that heat transfer enhancement techniques should be introduced in the cylindrical LHESS due to the low thermal conductivity of the PCM (Eason and Ayhan, 1996).

Heat transfer mechanism was studied in a cylindrical tube heat exchanger with PCM. Numerical results showed that at the beginning of the process, heat was transferred by conduction from the tube wall to the solid phase PCM through a relatively thin liquid layer. As the melting progressed, natural convection in the liquid became the dominant heat transfer mode (Shmueli et al., 2010).

Models based on the first law of thermodynamics were developed in cylindrical LHESS. A numerical model with an enthalpy-porosity formulation investigating the melting of PCM in a

cylindrical tube was conducted by Shmueli et al. (2010). An enthalpy-based method was employed by Esen and co-workers (1998) in a cylindrical latent heat storage tank as part of a domestic heating system. It was reported that the whole melting time of PCM depended not only on thermal and geometric parameters, but also on the thermophysical properties of the PCM.

Jones et al. (2006) performed an experimental and numerical study exploring the thermal characteristics of n-eicosane as PCM in a cylinder. Based on results from the experiment, a Stefan number of 0.1807 was recommended, which was also the best option for numerical benchmarking.

Latent heat storage unit of the shell and tube LHESS were discussed numerically in detail by many researchers. Lacroix (1993) developed a theoretical model to predict the transient behaviour of a shell and tube heat storage unit. This phase change problem was solved with an enthalpy-based method. Gong et al. (1997) presented a physical model of a shell-and-tube LHESS containing PCM. Numerical results indicated that introducing the hot and cold fluid from the same end of the storage system could achieve better performance. El-Dessouky et al. (1997) developed a second law analysis for various PCMs in LHESS, and the water-wax mixture was reported to have the maximum second law effectiveness.

1.3. Problem Statement

An obstacle to taking advantage of solid-liquid phase change in LHESS is the typically low thermal conductivity of PCMs. Various attempts have been made by researchers to enhance heat transfer in LHESS. However, due to the characteristics of each particular PCM, there can be a significant difference between the nature of heat transfer which requires specific corresponding design of heat transfer enhancement method. Therefore, a deeper understanding of heat transfer processes is necessary to take better advantage of the high latent heat of fusion of PCMs. In the open literature, there are few experimental research work looking at horizontal cylindrical LHESS integrated with lauric acid as the PCM, giving rise to the necessity of this work.

The research presented in this thesis concentrates a study of the phase change heat transfer

occurring within the LHESS, especially the determination of the impact of natural convection on the total heat transfer. The objectives of this work are as follows:

- Characterization of phase change behaviour of lauric acid;
- Testing of various experimental parameters (flow rates, HTF inlet temperature);
- Heat transfer enhancement resulting in the use of straight or angled fins.

1.4. Scope of the Thesis

The literature review as well as the objectives of the research work were presented in this chapter. Chapter 2 presents the experimental setup and procedures used to study charging and discharging processes inside the LHESS. The method applied to calculate the experimental uncertainty is also described in this Chapter 2.

Chapters 3 and 4 present experimental and numerical results in the first fin orientation (straight fins). The effect of heat transfer fluid (HTF) inlet temperature and HTF flow rates are discussed. The amount of energy stored and released is also presented. The dominant heat transfer mechanism during various stages of charging and discharging are determined. Experimental and numerical results are compared to identify heat transfer characteristics in lauric acid.

In Chapter 5, the results obtained using the second fin orientation (angled fins) are presented. Comparisons between the two fin orientations are conducted. Conclusions and recommendation for future work are discussed in Chapter 6.

Appendix A shows calibration results for probe thermocouples and Appendix B presents electrical circuit between the turbine flow meter and the LabView program. An experimental uncertainty analysis for energy stored during charging is shown in Appendix C. Photographs taken during charging and discharging can be found in Appendix D.

CHAPTER 2 EXPERIMENTAL PROCEDURES

2.1. Phase Change Material Selection

Previous work on PCM selection has been conducted by the Lab of Applied Multiphase Thermal Engineering at Dalhousie University. Based on data collected from an existing solar domestic hot water (SDHW) system in Halifax, the desirable melting temperature ranges was determined to be 42°C to 48°C and solidification temperature range to be 35°C to 40°C (Desgrosseilliers et al., 2011).

After filtering several PCMs, lauric acid was suggested as a suitable PCM which has minimal supercooling, chemical stability, non-corrosiveness and reasonable cost (CAD \$16.50/kg for non bulk quantities). The differential scanning calorimetry (DSC) curve of lauric acid is presented in Fig. 2.1. Thermophysical properties of lauric acid are displayed in Table 2.1. The melting and solidification temperature is observed as 42.5°C experimentally (Desgrosseilliers et al., 2011).

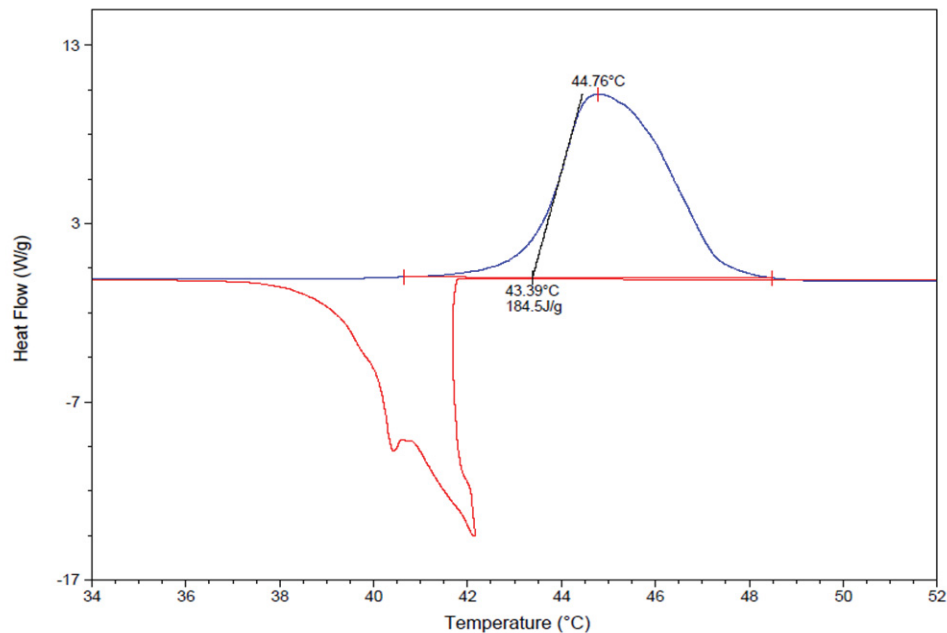


Figure 2.1: DSC curve for lauric acid (Desgrosseilliers et al., 2011)

Table 2.1: Thermophysical Properties of Lauric Acid (Yaws, 2003; Alfa Aesar)

Molecular Weight	200.31 (kg/kmol)
Density of solid at 20°C	950 (kg/m ³)
Density of liquid at 45°C	873 (kg/m ³)
Fusion temperature	44 (°C)
Latent heat of fusion	182 (kJ/kg)
Specific heat solid/liquid	2.4/2.0 (kJ/kg·K)
Thermal conductivities solid/liquid	0.150 (W/m·K) / 0.148(W/m·K)
Dynamic viscosity	0.008* (Pa·s)
Thermal diffusivity of solid	6.5×10 ⁻⁵ (m ² /s)
Thermal diffusivity of liquid	8.48×10 ⁻⁵ (m ² /s)

* Data obtained near the fusion temperature

2.2. Heat Transfer Enhancement Technique

As mentioned in the literature review section, as a common heat transfer enhancement technique, adding fins to LHESS has been studied by many researchers (Groulx and Ogoh, 2010, Agyenim et al., 2009; Velraj et al., 1999). Natural convection has been proven to be the dominant heat transfer mode after the initial melting stage of the PCM. A higher melting fraction was detected at the top portion of rectangular LHESS (Wang et al., 1999), cylindrical LHESS (Saitoh and Kato, 1993) and spherical LHESS (Chan et al., 2006).

Horizontal fins extending from the vertical heated wall were studied by Lacroix et al. (1997). It was reported that the melting rate was nearly independent of fin numbers for shorter fins. It was also noted that after the melting front passed the tip of the fins, no heat transfer enhancement was detected compared to the no-fin case. As a consequence, fewer longer fins were recommended for optimised heat transfer enhancement.

The thickness of fins on the heat transfer enhancement effect was also studied (Shatikian et al. 2005). It was observed that thin fins might experience a certain temperature gradient while thick fins can help provide a uniform temperature along the length. However, the fins should not be so thick as to reduce the PCM volume significantly or overly increase the weight of the LHES.

Based on the general conclusions listed above, four longitudinal fins with a thickness of 2 mm are selected for this work. Fins are located on the outer surface of a copper pipe perpendicular to the surface and parallel to the flow direction, extending towards the radial direction. More details on the fins can be found in section 2.3. Instead of investigating the length and number of fins, this research focuses on the effect of geometric arrangements. Emphasis was put on the orientation of the fins; the side views of the two tested fin orientations are shown in Fig. 2.2: the first orientation is referred to as straight fins and the second one as angled fins.

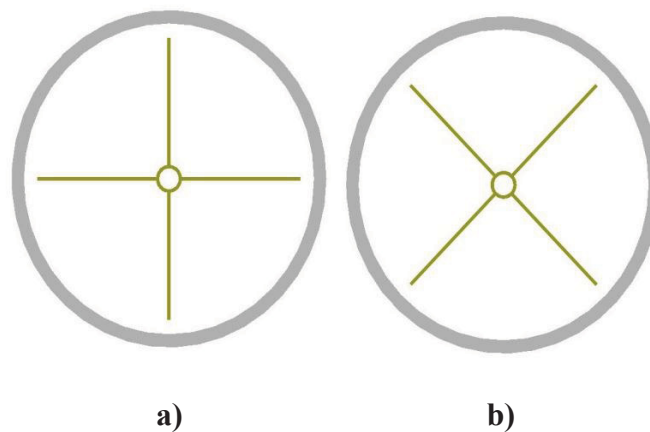


Figure 2.2: Orientations of longitudinal fins: a) straight fins; b) angled fins



Figure 2.3: Copper longitudinal fins added into lauric acid

2.3. Experimental Setup

The experimental setup is a loop consisting of hot water bath, circulation pump, flow meter, PCM testing section and data acquisition system. A schematic presenting the experimental setup is shown in Fig. 2.4.

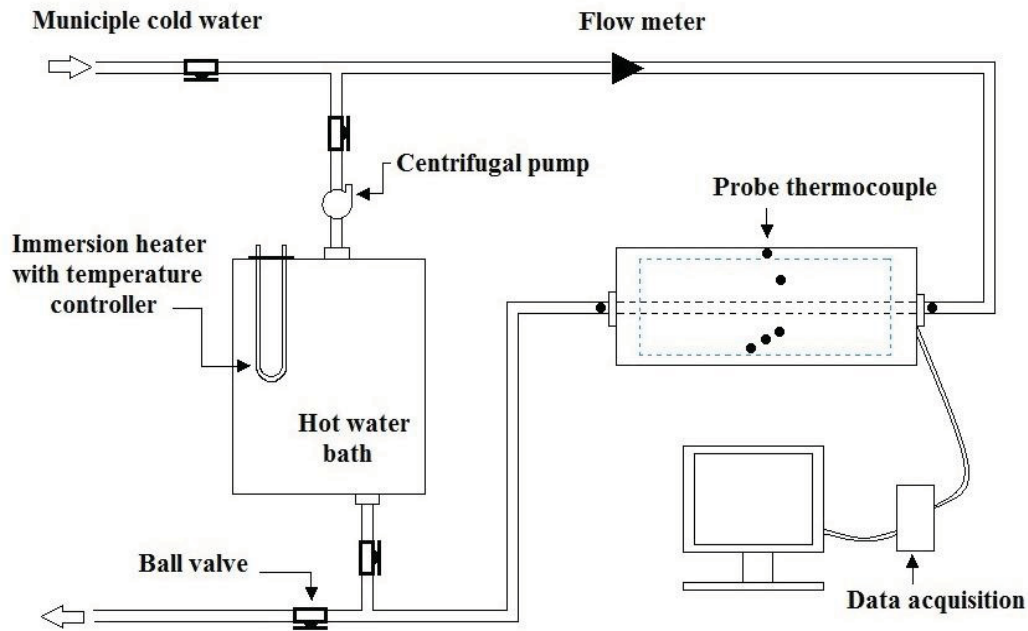


Figure 2.4: Schematic of the experimental setup

In the testing section, a cylindrical acrylic container is filled with PCM and probe thermocouples are inserted inside the PCM to monitor temperatures. The cylinder is 12" long and has a 6" outside diameter, a 1/4" thickness, and is transparent for the convenience of visualization (Fig. 2.5). A 1/2" copper pipe passes through the container center. Water passes through the copper pipe to transfer energy. All fins are made of copper which extend outwards from the pipe, only leaving a 1/4" gap between them and the container wall.

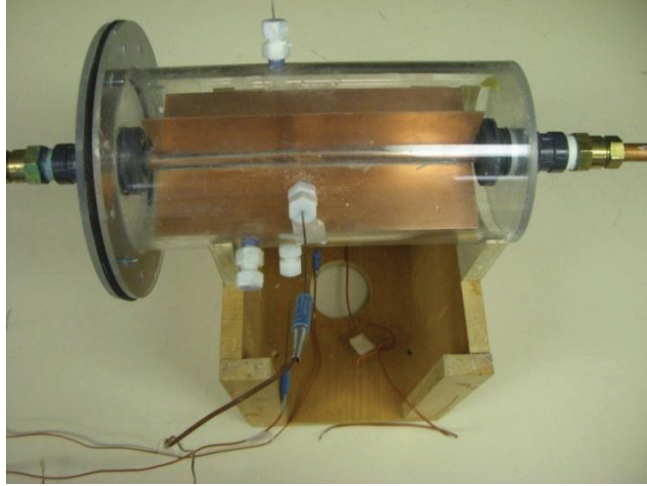


Figure 2.5: The PCM Container with longitudinal copper fins

In this setup, seven type-T probe thermocouples (probe diameter is 0.0625 inch with ungrounded junction) and nine type-T attachable surface thermocouples are connected to a National Instruments 16-channel thermocouple module (NI9213) CompactDAQ data acquisition system (Fig. 2.8b). Five holes, 0.5 inch in diameter, were drilled in the Plexiglas cylinder radially to support threads for probe thermocouples. These holes are sealed with silicone cement to prevent leakage.

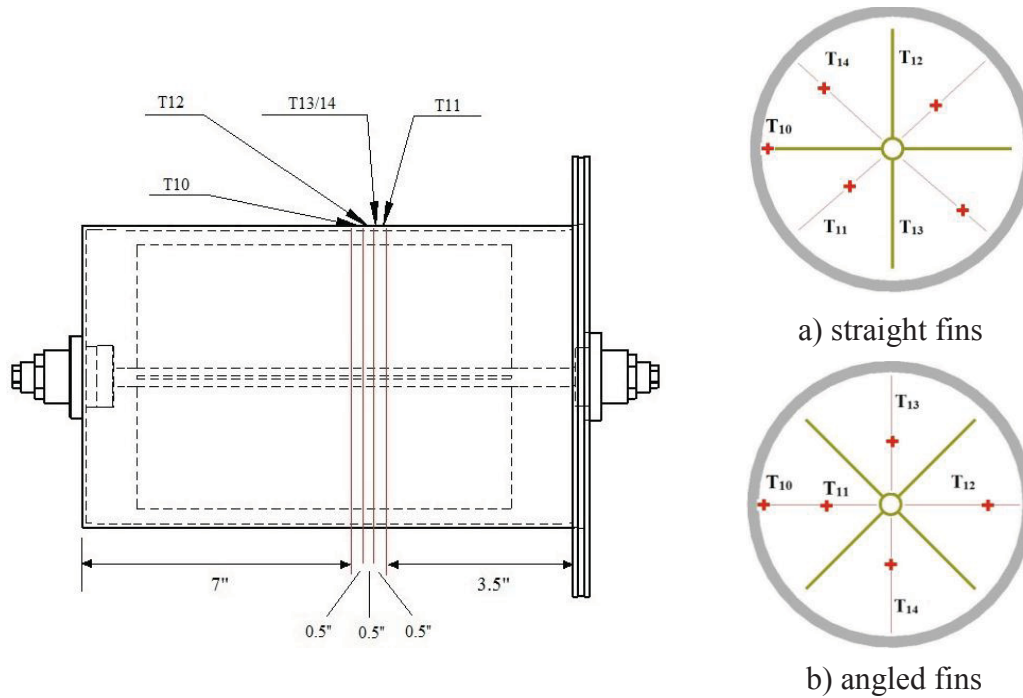


Figure 2.6: The positions of probe thermocouples

Two probe thermocouples (T15 and T16) are inserted at the water inlet and outlet positions inside the copper pipe, and the other five thermocouples (T10 to T14) are placed inside the container. Temperatures were recorded using LabView at a time interval of 30 seconds. Probes T11 to T14 are set to be at different locations in each quadrant delimited by the fins in order to record more temperature inside the PCM. T10 is in the middle of the gap between the end of the fin and the cylinder wall (the gap is $\frac{1}{4}$ inch wide). An example of probe thermocouple locations is shown in Fig. 2.6 where thermocouples are presented by red crosses. The length inside the container is determined by deducting the thickness of the PCM container and the length exposed from the total probe length (6").

Nine type-T surface thermocouples are attached on the four fins to provide additional temperature information (Fig. 2.7 and Fig. 2.8a).

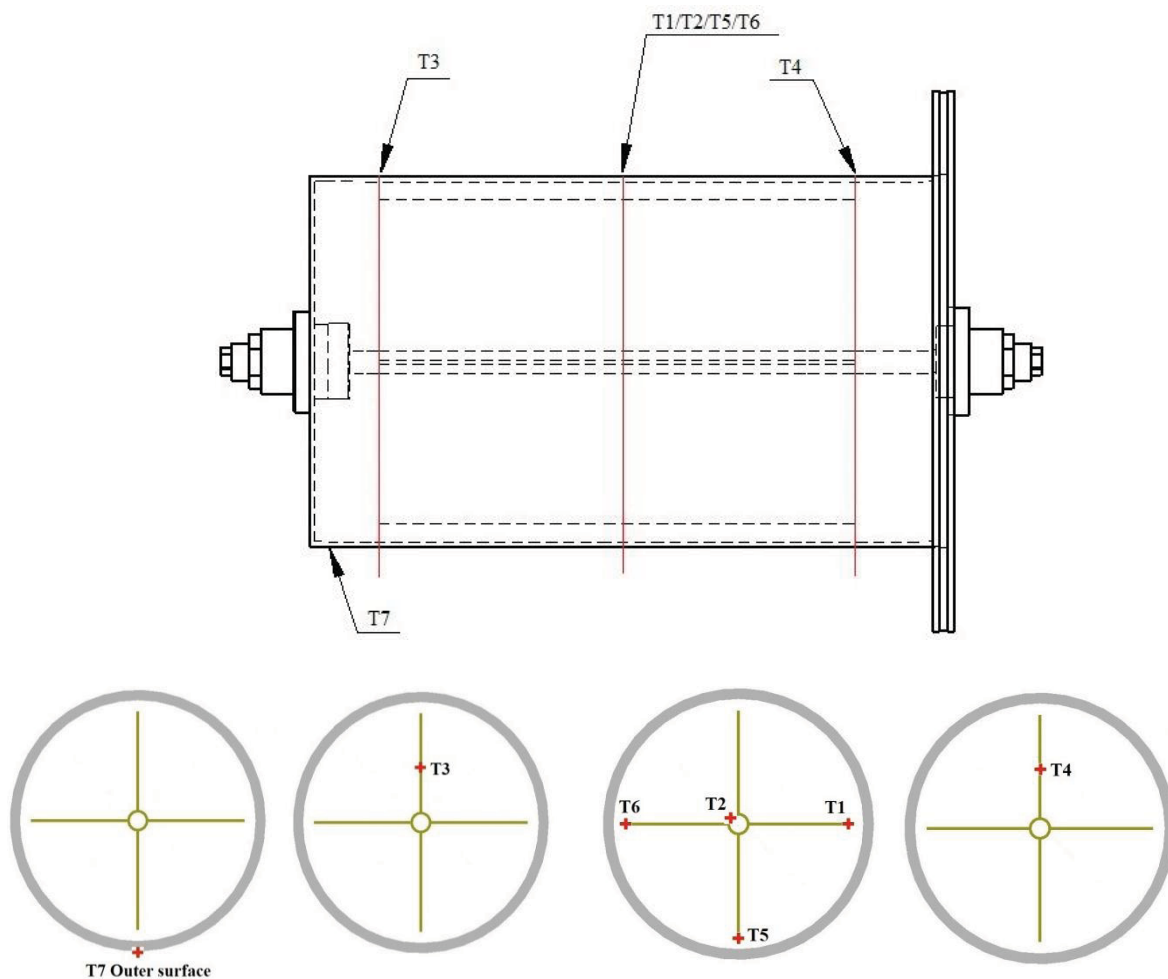
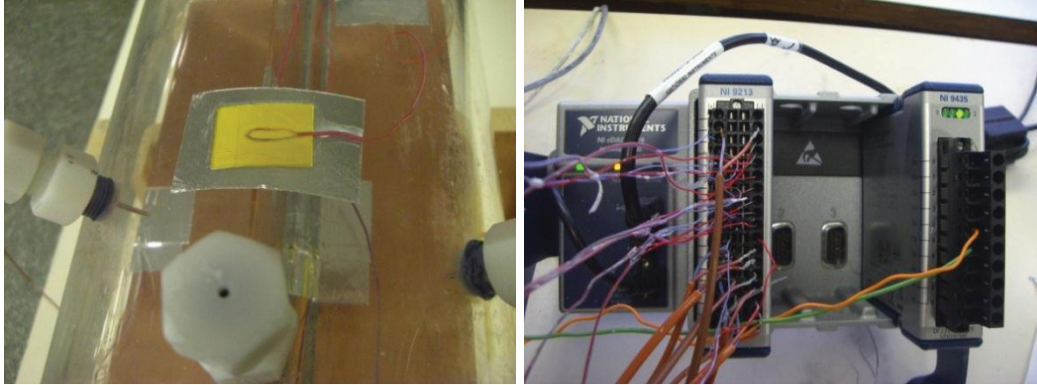
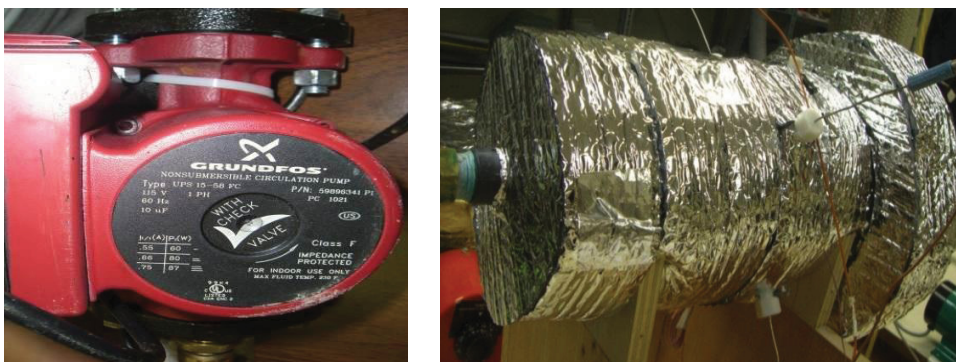
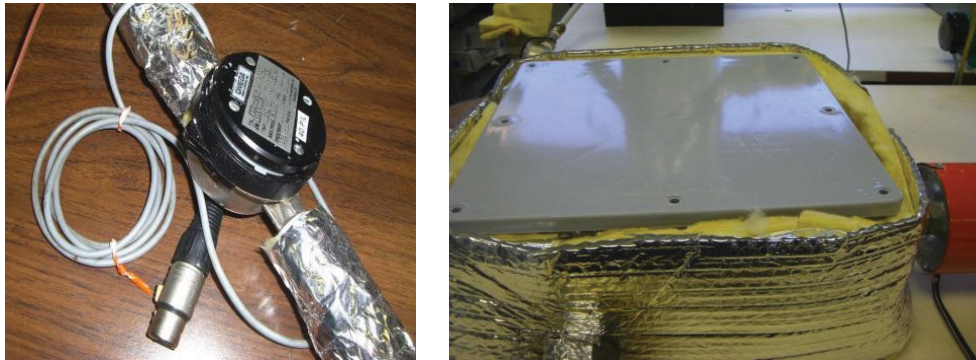


Figure 2.7: The positions of surface thermocouples



a) b)
Figure 2.8: a) An example of attachable thermocouple; b) The compactDAQ data acquisition system



a) b) c) d)
Figure 2.9: a) The flow meter from Omega (model FTB 4605); b) The constant water bath; c) The centrifugal pump from Grundfos; d) The insulation of the PCM container

A pulse counter flow meter from Omega (model FTB 4605, Fig. 2.9a) is connected to a counter/pulse generation module (NI9435, Fig. 2.8b) on the DAQ system and also read by LabView. In the charging loop, a 500 W emersion heater (model TSP02793) is used to keep the hot water at a constant temperature in the water bath (Fig. 2.9b), and water is circulated by a centrifugal pump from Grundfos (model UPS 15-58 FS, Fig. 2.9c). The hot water bath, pipes and PCM container are insulated by two layers. The first layer is glasswool with a thickness of 0.3 cm; the second layer is Reflectix bubble insulation (Fig. 2.9d).

2.4. Procedure

Charging

Before the experiment, liquid lauric acid at 50°C was poured into the cylindrical container. Considering the thermal expansion effect of the PCM, when the container was filled with lauric acid in the liquid state, the container was sealed. This led to approximately 10% of vacancy (by observation) at the top of the container after all the PCM was solidified.

For each test run, the PCM was cooled down to approximately 10°C before starting to circulate hot water. This procedure provided a base line for comparison. After this step, the water tank was heated by an immersion heater until the desired temperature was achieved, and this was followed by energizing the circulation pump. It took 8 to 15 minutes to achieve the desired inlet water temperature because of the cold water in the loop. Three hot HTF temperatures were tested: 50°C, 55°C, and 60°C. The charging time varied between 6 to 24 hours for each test.

In order to get temperature information in various locations inside the container, experiments are repeated with identical experimental parameters. For each repeated test, the probe thermocouples T11 to T14 are placed at different depth.

Discharging

Municipal cold water was used in an open loop to discharge the system. The flow rate of cold water varied from 1 L/min to 13 L/min in each testing group. The temperature of municipal cold water was approximately 9°C with high temperature stability (within $\pm 3^\circ\text{C}$).

2.5. Heat Transfer Fluid Properties

The temperature-dependent properties of the HTF (water) are shown in Table 2.2. There is no significant change of properties over a temperature range of 9-60°C for density, thermal conductivity and specific heat. However, dynamic viscosity and Prandtl number of water varies greatly over this temperature range.

Table 2.2: Properties of Water (Xydatasource; Incropera et al. 2005)

Properties /Temperature	9°C	50°C	55°C	60°C
Density (kg/m^3)	999.84	987.70	989.95	983.20
Thermal conductivity ($\text{W/m}\cdot\text{K}$)	0.585	0.641	0.646	0.652
Dynamic viscosity ($10^{-6}\text{N}\cdot\text{s/m}^2$)	1343	560	515	477
Specific heat ($\text{kJ/kg}\cdot\text{K}$)	4.198	4.180	4.182	4.184
Prandtl number	9.68	3.06	3.33	3.65

2.6. Experimental Uncertainty Analysis

2.6.1. Calibration of Probe Thermocouples

Probe thermocouples are calibrated using the Hart Scientific Model 7102 micro-bath (Fig. 2.10). The Hart Scientific micro-bath which has a 48 mm diameter and a 140 mm deep tank filled with silicone oil. The calibration bath is stable to $\pm 0.015^\circ\text{C}$ at a temperature of -5°C and $\pm 0.03^\circ\text{C}$ at a temperature of 121°C .



Figure 2.10: Hart Scientific Model 7102 micro-bath

During the calibration, probe thermocouples were labelled with numbers and divided into two groups in order to ensure sufficient space between each other. T10 to T13 were tested in the first group and T14 to T16 were tested in the second group. In each test, tested thermocouples were immersed into the oil at the same depth and thermocouple readings were recorded by Labview program.

Since the temperature range of the PCM used in this work was 10°C to 60°C, the procedure was repeated in six sets: 10°C, 20°C, 30°C, 40°C, 50°C, and 60°C. In each testing round, the bath temperature was first set to be 10°C, and after 30 minutes when the bath was stabilized, readings were recorded. The temperature was then raised to 20°C and the procedure was repeated. In total, five rounds were performed. Part of the calibration results are presented in the following section 2.6.2 and more detailed results are presented in Appendix A.

2.6.2. Method Description

There are two kinds of experimental errors in this work: precision errors and bias errors. Precision errors, also called random errors, usually result from fluctuating experimental conditions (Mills and Chang, 2004). Precision errors in this work include fluctuation of room temperature, fluctuation of power input, and other unpredicted precision errors.

Bias errors which are also called systematic errors have many sources. Some instruments have a bias error associated with hysteresis or local nonlinearity in the instrument response (Mills and Chang, 2004). Apart from apparent bias errors caused by measuring instrument, there are also hidden bias errors. For instance, a surface thermocouple will not read accurate temperature results without a good thermal contact. In this work, the primary experimental errors are bias errors which come from the measuring instruments: the flow meter and thermocouples.

For the energy stored and recovered from the LHESS, energy is calculated as following:

$$\dot{Q} = \dot{m}c_p(T_{in} - T_{out}) \pm u_{\dot{Q}} \quad (2.1)$$

The c_p of water is assumed to be a constant. Therefore, the measurement errors are calculated using the following equations:

$$u_{\dot{Q}} = c_p \sqrt{\left(\frac{\partial \dot{Q}}{\partial \dot{m}} u_{\dot{m}}\right)^2 + \left(\frac{\partial \dot{Q}}{\partial T_{in}} u_{T_{in}}\right)^2 + \left(\frac{\partial \dot{Q}}{\partial T_{out}} u_{T_{out}}\right)^2} \quad (2.2)$$

This experimental uncertainty analysis will be conducted in Chapter 3 to specify the error range of energy stored during charging. The maximum uncertainties of various experimental data are presented in Table 2.3.

Table 2.3: Maximum uncertainties for experimental data

Measurement	Units	Maximum error
Volumetric flow rate of water	m ³ /kg	± 2%
Temperature of T ₁₀	°C	± 0.42°C
Temperature of T ₁₁	°C	± 0.37°C
Temperature of T ₁₂	°C	± 0.40°C
Temperature of T ₁₃	°C	± 0.39°C
Temperature of T ₁₄	°C	± 0.35°C
Temperature of water inlet T ₁₅	°C	± 0.27°C
Temperature of water outlet T ₁₆	°C	± 0.32°C

2.6.3. Validation of Repeatability

In order to validate the repeatability of the experiment, two tests under the same condition were conducted with a HTF inlet temperature of 60°C and HTF flow rate of 1L/min. Figure 2.11 shows the temperature recorded in both tests which validates the repeatable nature of the experiment.

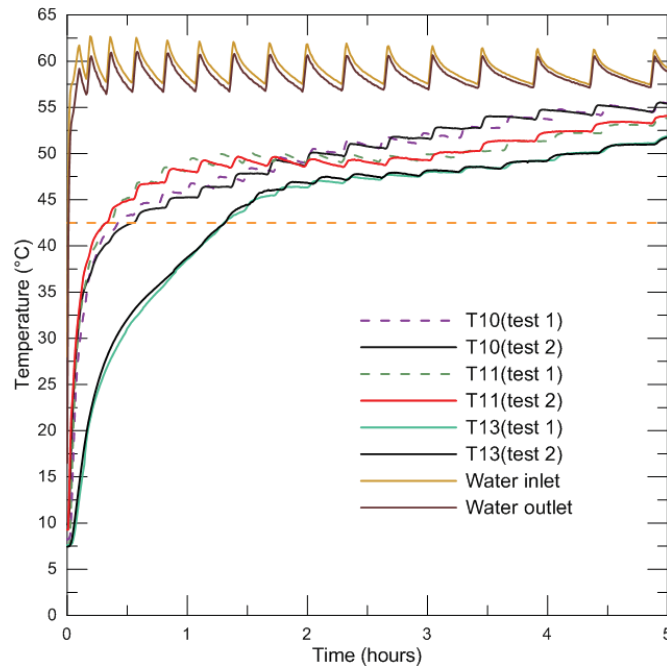


Figure 2.11: Validation of repeatability (HTF inlet temperature of 60°C, HTF flow rate 1L/min)

2.6.4. Validation of Symmetry

The symmetry assumption is investigated by comparing temperature profiles recorded by T11 to T14. In this test, T11 and T13 are placed at the same depth into lauric acid in each lower quadrant. T12 and T14 are placed at the same depth into lauric acid in each upper quadrant. The HTF inlet temperature in this test is 60°C, and the HTF flow rate is 1L/min. Temperature profiles of T11 to T14 are shown in Fig. 2.12.

The temperature differences between T11 and T13, T12 and T14 are within experimental error. The error might be caused by slight measurement error of probe length inside PCM. In addition, taking the uncertainty of thermocouple into consideration, the temperature difference falls into a

reasonable error range. A photograph (Fig.2.13) was taken after two hours of charging during this test, symmetry is observed in the system.

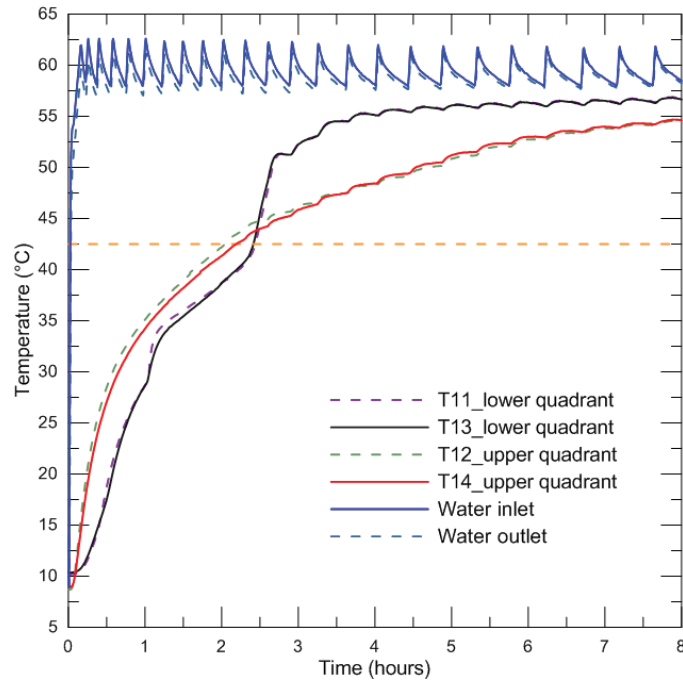


Figure 2.12: Validation of symmetry (HTF inlet temperature of 60°C, HTF flow rate 1L/min)

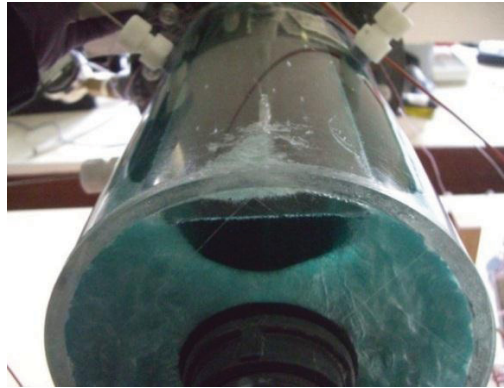


Figure 2.13: Validation of symmetry after 2 hours of charging (HTF inlet temperature 60°C, HTF flow rate 1L/min)

2.6.5. The Three-dimensional Effect

Temperature gradient along the fin axial direction is investigated. T3 and T4 are located at two ends of the fin, with T3 at the water inlet side and T4 at the water outlet side. From Fig. 2.14, the temperature profile indicates no significant gradient in the axial direction.

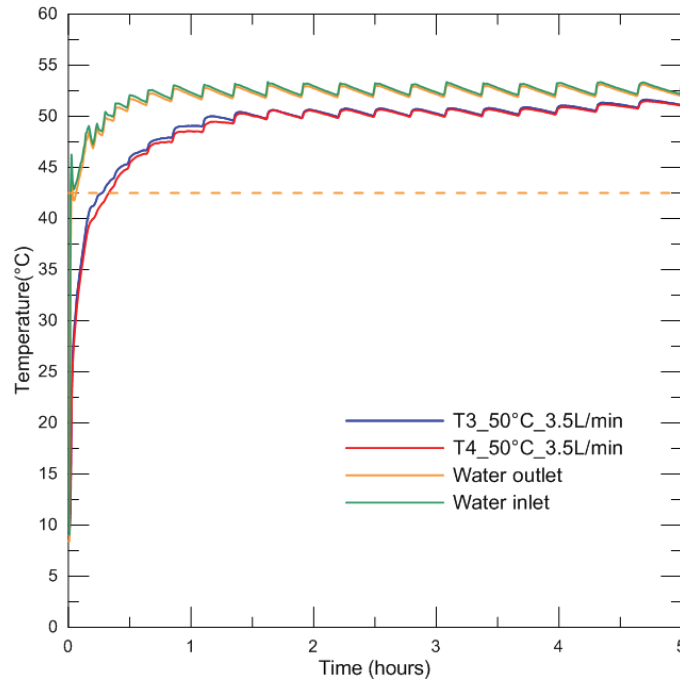


Figure 2.14: The attachable thermocouple temperature profile

Therefore, in this experimental study, assumption is made that phase change of lauric acid in this LHESS can be presented as a two-dimensional system in the radial and angular directions. Moreover, the end-wall effect is negligible. Under this assumption, the difference of probe locations (T10 to T14) along the axial direction is neglected. Moreover, the numerical model of this work can also be simplified to a two-dimensional model.

CHAPTER 3 EXPERIMENTAL RESULTS FOR STRAIGHT FIN CONFIGURATION

A series of tests were conducted to explore the melting and solidification mechanism of lauric acid with two sets of fin orientation as shown in section 2.3: the first orientation is referred to as straight fins and the second one as angled fins. Experimental results from straight fins are presented in this chapter.

The temperature profiles inside the PCM container which help determine the dominant heat transfer mechanism during different stages of phase change are presented. The effects of varying two primary experimental parameters, the HTF inlet temperature and the HTF flow rate, are studied. Energy stored during charging is presented with the experimental uncertainty analysis.

3.1. Charging and Discharging of the PCM

3.1.1. Charging

Temperature profiles of probe thermocouples at various HTF inlet temperatures and HTF flow rates are presented in this section to obtain an understanding of the heat transfer mechanism inside lauric acid during charging. In order to clearly show the location of each probe thermocouple, an indicator is included on the top right corner of each figure to show the distance away from the central pipe. Besides, in each figure, the melting/solidification temperature is marked as an orange dotted line.

Figures 3.1 to 3.3 present temperature profiles of probe thermocouples T10 to T14 at a HTF inlet temperature of 50°C with three different HTF flow rates. Detailed analysis of temperature profiles will be presented in section 3.2. It is generally observed from Figs 3.1 to 3.3 that increasing the HTF flow rate can reduce the complete charging time for the LHESS. The impact of HTF flow rates will be further discussed in section 3.4. The complete charging time and discharging time will be shown in section 3.5.

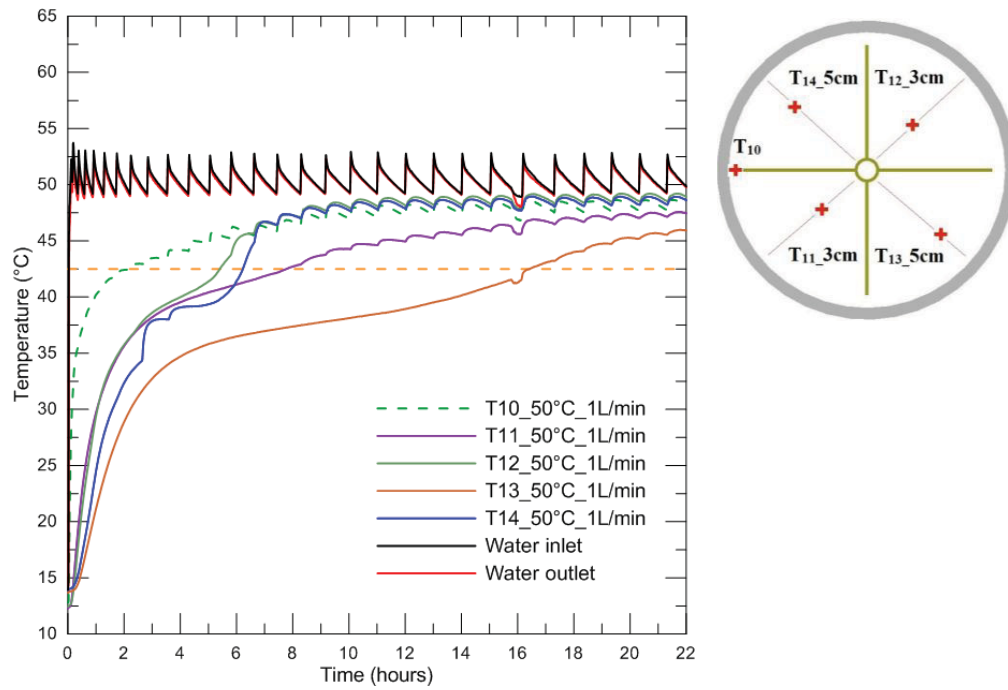


Figure 3.1: Temperature profiles of T10 to T14 at a HTF inlet temperature of 50°C and HTF flow rate of 1L/min

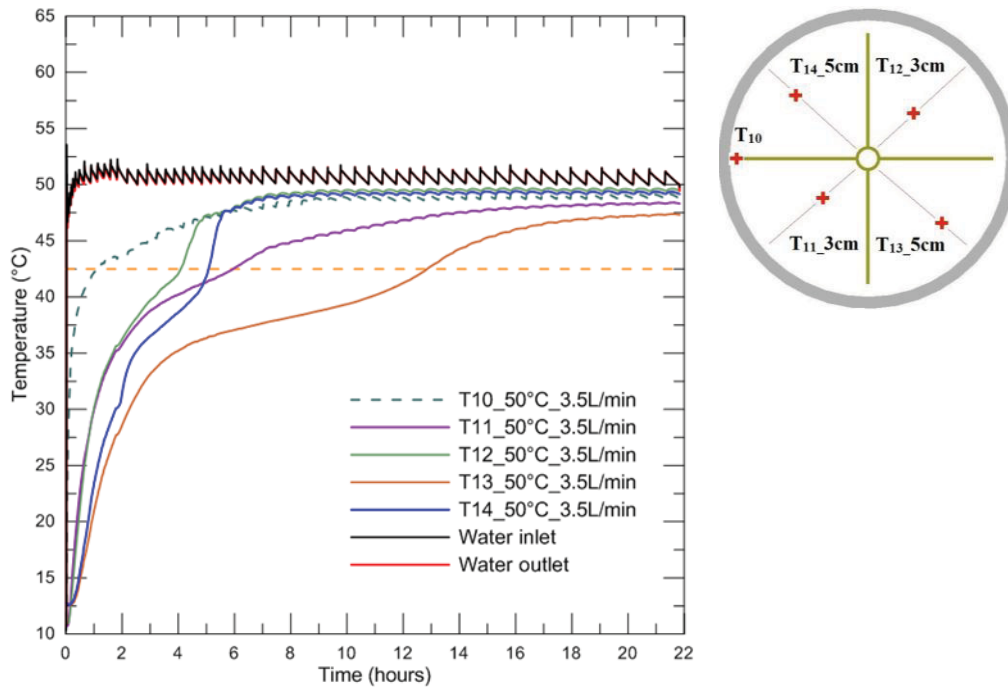


Figure 3.2: Temperature profiles of T10 to T14 at a HTF inlet temperature of 50°C and HTF flow rate of 3.5L/min

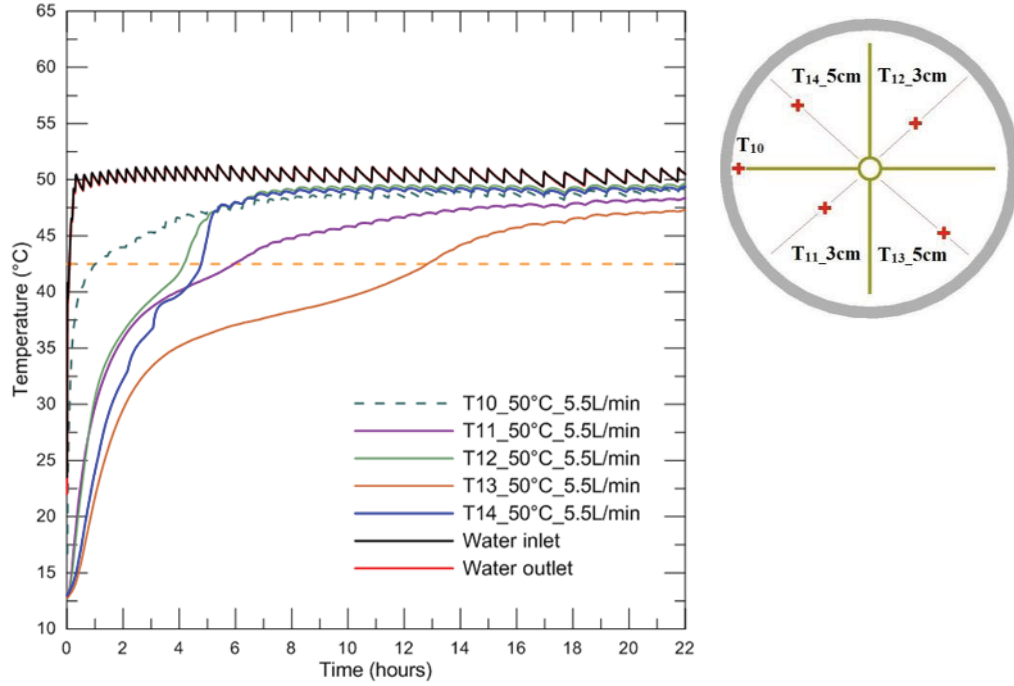


Figure 3.3: Temperature profiles of T10 to T14 at a HTF inlet temperature of 50°C and HTF flow rate of 5.5L/min

Figures 3.4 to 3.6 present temperature profiles of probe thermocouples T10 to T14 at a HTF inlet temperature of 55°C with three different HTF flow rates. It is noted that the complete charging time is reduced compared with Figs 3.1 to 3.3, which have lower HTF inlet temperature.

It is also found that at the same distance away from the central pipe, higher quadrants and lower quadrants have different temperature profiles. In higher quadrants, faster melting and higher temperatures are achieved which is caused by the natural convection effect. Hot melted PCM is displaced upwards because of buoyancy effect, and relatively cold PCM descends to the bottom. Detailed discussion of the impact of HTF inlet temperature will be presented in section 3.3.

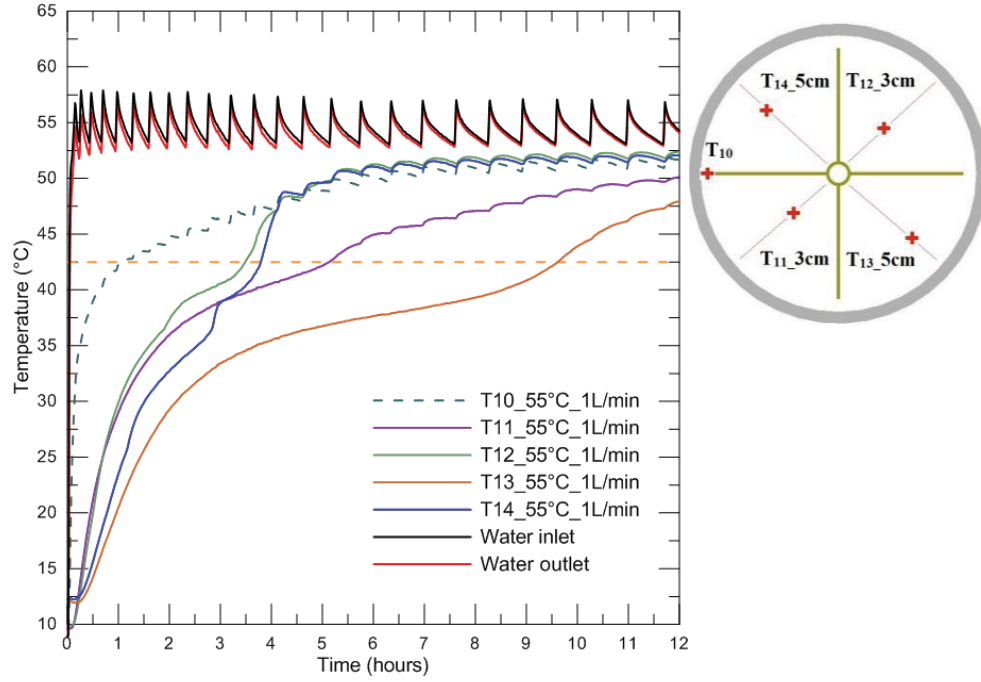


Figure 3.4: Temperature profiles of T10 to T14 at a HTF inlet temperature of 55°C and HTF flow rate of 1L/min

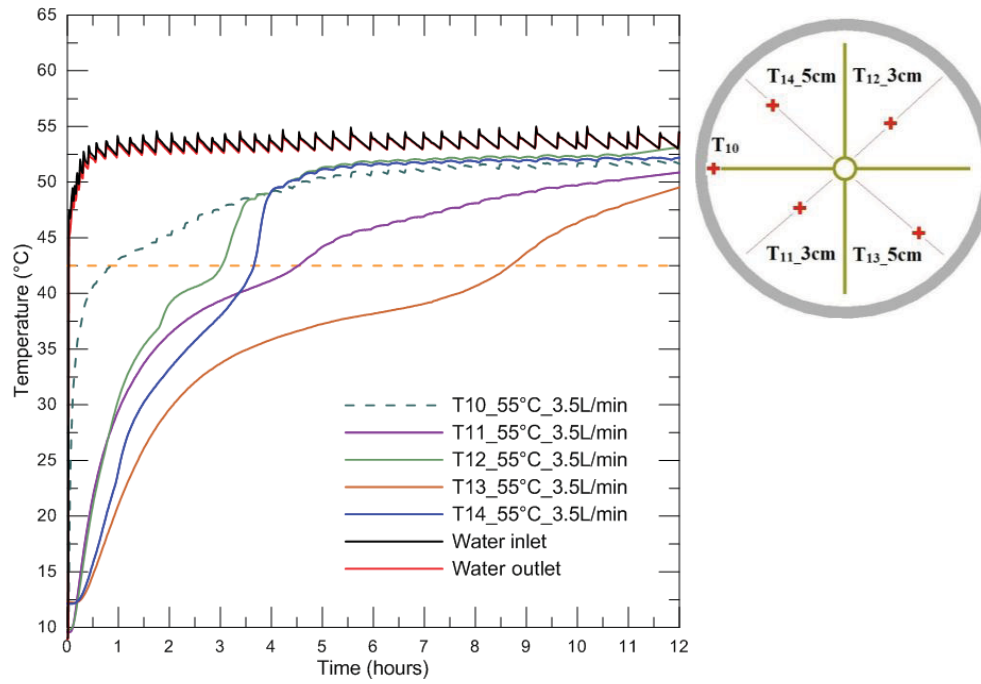


Figure 3.5: Temperature profiles of T10 to T14 at a HTF inlet temperature of 55°C and HTF flow rate of 3.5L/min

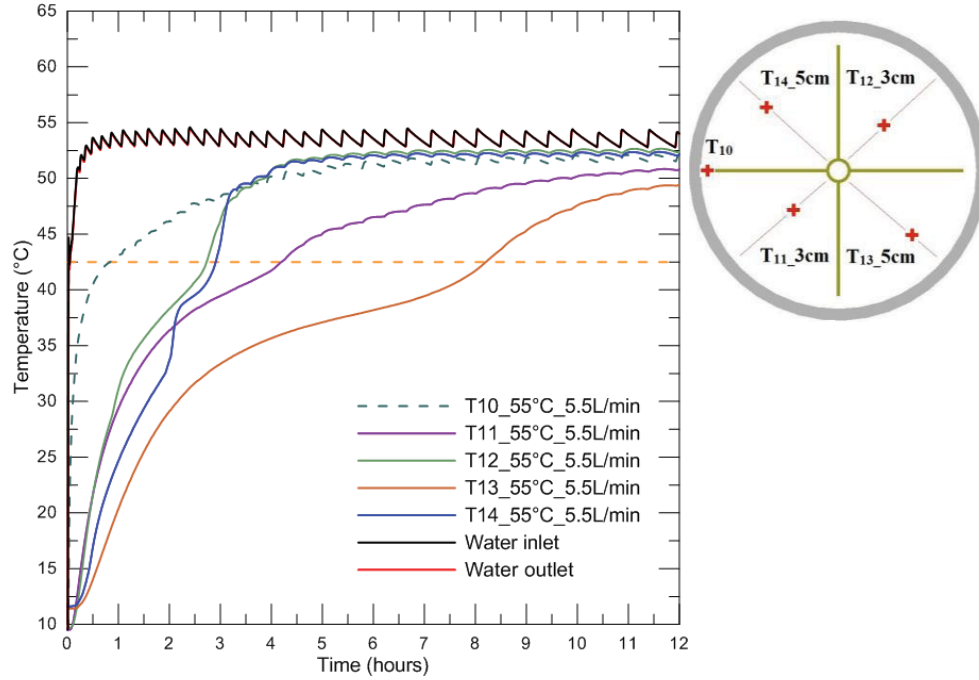


Figure 3.6: Temperature profiles of T10 to T14 at a HTF inlet temperature of 55°C and HTF flow rate of 5.5L/min

Figures 3.7 to 3.9 present temperature profiles of probe thermocouples T10 to T14 at a HTF inlet temperature of 60°C with three different HTF flow rates. It is noted that the complete charging time is reduced significantly compared with tests with lower HTF inlet temperatures (50°C and 55°C). It is also found that natural convection is more intense in the upper quadrants compared with lower quadrants. Further discussion of the intensity of natural convection in each quadrant will be presented in section 3.2.

For various HTF inlet temperatures, a dimensionless number, Stefan number is introduced. Stefan number is defined as the ratio of sensible heat to latent heat in phase change problems. It is given by the following formula:

$$Ste = \frac{c_p \cdot \Delta T}{L} \quad (3.1)$$

Where c_p is the specific heat of the PCM, ΔT is the temperature difference between HTF inlet temperature and the melting temperature of the PCM, L is the latent heat of the PCM. For three hot HTF inlet temperatures during charging, 50°C, 55°C, and 60°C, the Stefan number are

namely 0.091, 0.151 and 0.212. For discharging, which only has one HTF inlet temperature of 9°C, the Stefan number is 0.442.

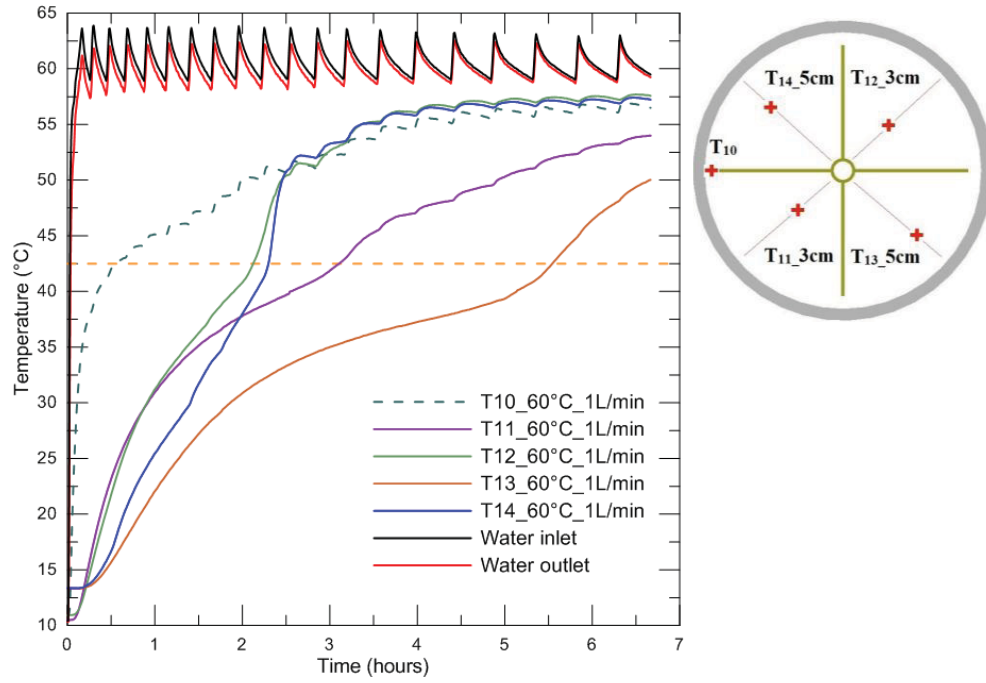


Figure 3.7: Temperature profiles of T10 to T14 at a HTF inlet temperature of 60°C and HTF flow rate of 1L/min

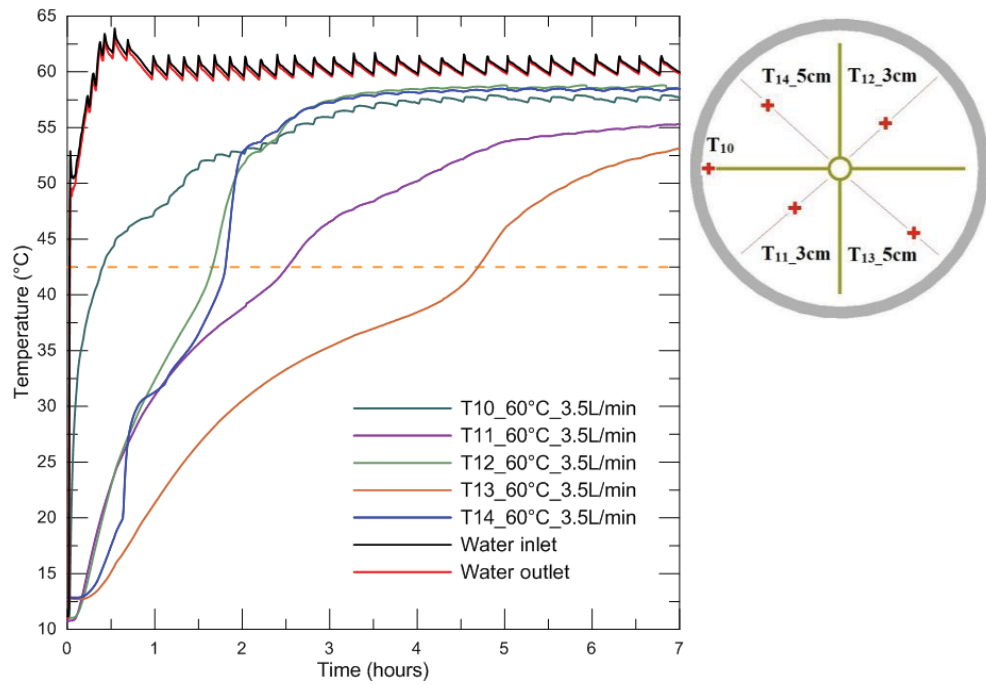


Figure 3.8: Temperature profiles of T10 to T14 at a HTF inlet temperature of 60°C and HTF flow rate of 3.5L/min

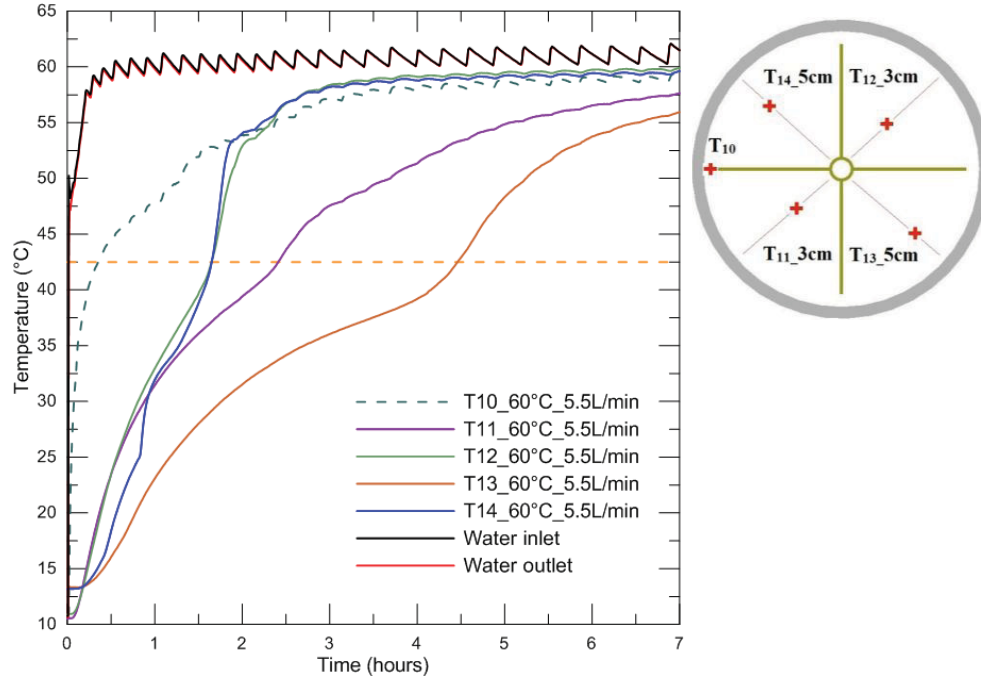


Figure 3.9: Temperature profiles of T10 to T14 at a HTF inlet temperature of 60°C and HTF flow rate of 5.5L/min

3.1.2. Discharging

Temperature profiles of probe thermocouples T10 to T14 during discharging are shown in Figs. 3.10 to 3.12 with various HTF flow rates. During solidification, solid lauric acid forms on the heat transfer surfaces including the central pipe and fins. As discharging progresses, the solidification front moves outwards from the heat transfer areas and more solid lauric acid is formed. It is seen that the temperatures at similar distances from the central pipe have similar profiles regardless of them being in the upper or lower quadrant. This points to the fact that natural convection, which in this case would be stronger in the lower quadrant, does not play a role during discharging. Moreover, once solidified on the copper fins, natural convection cannot exist in the solid PCM, which limits the impact of natural convection even more. The discharging process is then conduction-dominated.

It is also noticed that at 5 cm from the central pipe, the temperature of lauric acid decreases more rapidly in the higher quadrant compared to the lower quadrant. This can be explained because of the approximately 10% vacancy found in the upper quadrant.

Moreover, increasing the HTF flow rate from 1.5L/min to 13L/min does not significantly reduce the complete discharging time. In other words, the impact of HTF flow rate on discharging is minimal. The reason is solid lauric acid is formed on the heat transfer surfaces which increases the thermal resistance on the PCM side and also limits the natural convection during discharging.

Because of the isothermal nature of phase change, temperature plateaus are expected in temperature profiles. Further discussion of temperature plateaus can be found in section 3.2. Moreover, the impact of HTF flow rates on discharging is included in section 3.4.

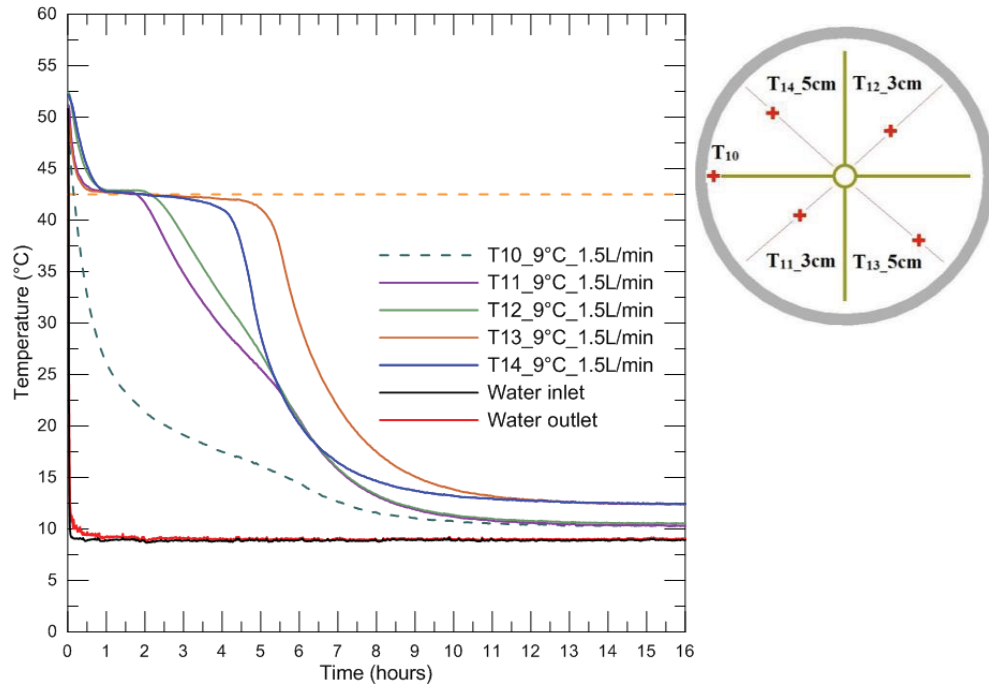


Figure 3.10: Temperature profiles of T10 to T14 at a HTF inlet temperature of 9°C and HTF flow rate of 1.5L/min

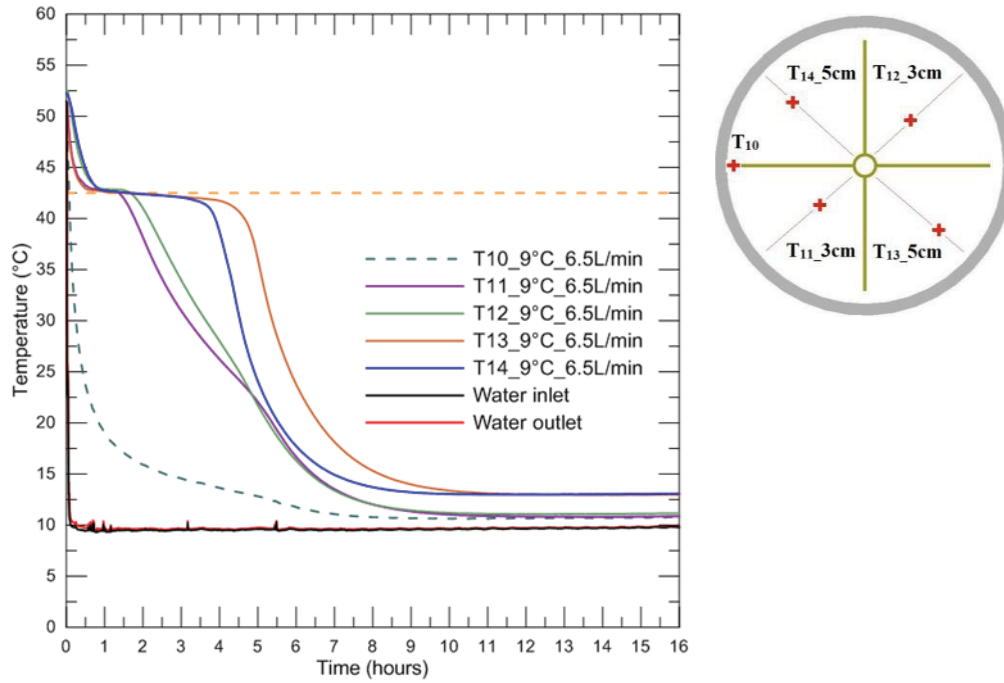


Figure 3.11: Temperature profiles of T10 to T14 at a HTF inlet temperature of 9°C and HTF flow rate of 6.5L/min

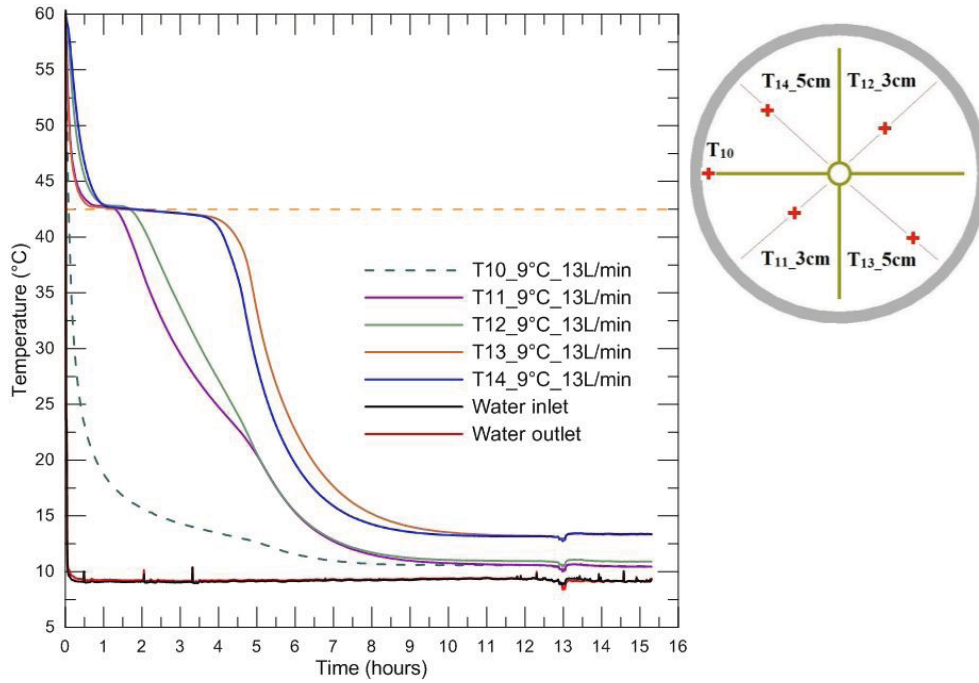


Figure 3.12: Temperature profiles of T10 to T14 at a HTF inlet temperature of 9°C and HTF flow rate of 13L/min

3.2. Detailed Temperature Profiles

3.2.1. Charging

Temperature profiles, with probe thermocouples at various locations inside the PCM, and a HTF inlet temperature of 60°C and flow rate of 1 L/min are shown in Figs. 3.13 and 3.14, which presents the higher quadrant and lower quadrant respectively. Those results were obtained by running the same experiment multiple times, varying the position of the probes from one experiment to the other.

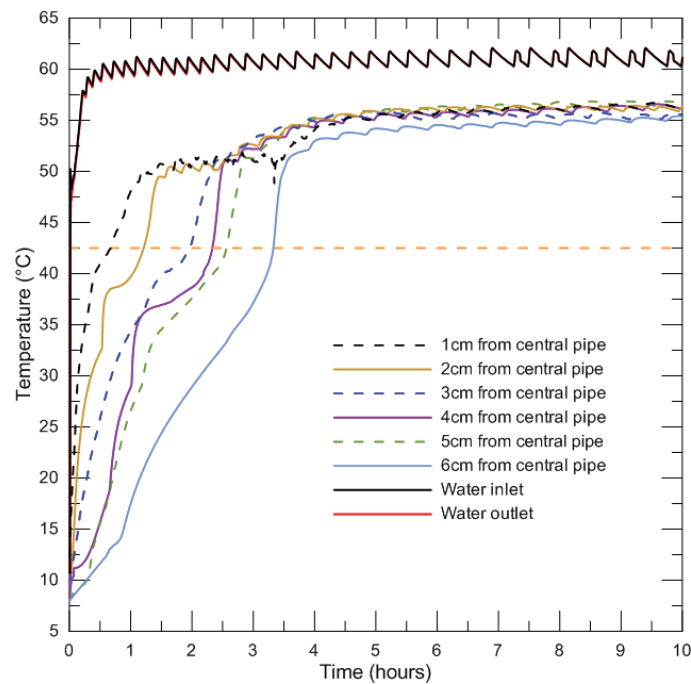


Figure 3.13: Temperature profiles of higher quadrants at a HTF inlet temperature of 60°C and HTF flow rate of 1L/min

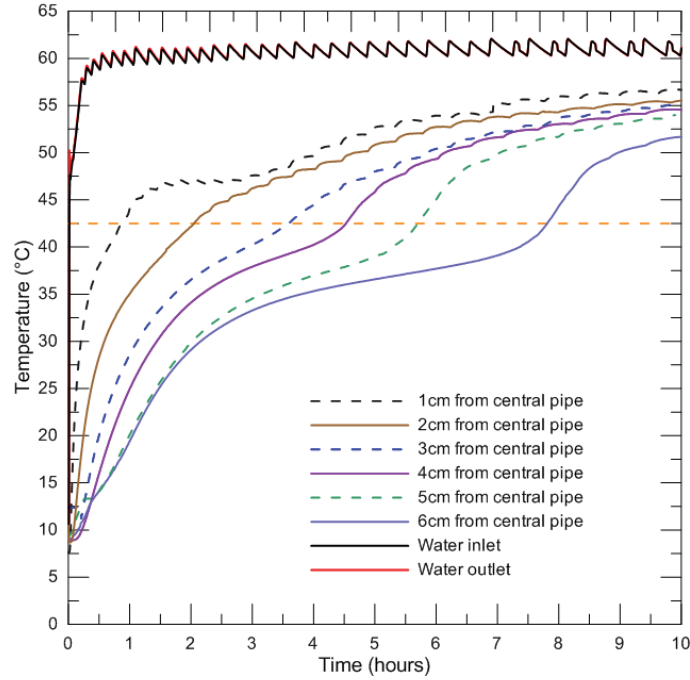


Figure 3.14: Temperature profiles of lower quadrants at a HTF inlet temperature of 60°C and HTF flow rate of 1L/min

It is found from Figs. 3.13 and 3.14 that heat conduction is the dominant heat transfer mode at the initial stage of charging which can be partially validated from the linear temperature profile at the beginning of the charging process. In order to validate this statement from another point of view, a numerical model with pure conduction was created and results are compared in section 4.2.1.

As charging progresses, more liquid PCM is formed around the heat transfer surfaces. Natural convection starts to play a more important role. This effect can be deduced by comparing temperature profiles in the higher and lower quadrants. In the higher quadrant (Fig. 3.13), lauric acid tends to melt faster than in the lower quadrants. For the points at 6cm away from the central pipe, the time required for reaching the melting point is 3.3 hours and 7.8 hours, respectively for higher and lower quadrants. There are two fins from which natural convection can provide heat transfer enhancement in higher quadrants compared with only one fin in lower quadrants (Fig. 3.15). Moreover, because of the presence of natural convection, heat is displaced upwards which enhances the heat transfer rate in higher quadrants. Consequently, for lauric acid in higher

quadrants, it takes less time to melt and a higher temperature is observed compared with the same location in lower quadrants. As a conclusion, after the initial stage of melting, natural convection becomes the dominant heat transfer mode.

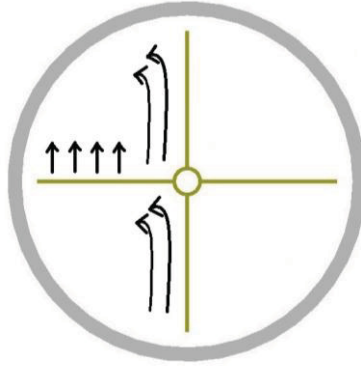


Figure 3.15: Representation of the heat transfer enhancement by the fins as a function of the quadrant

The fluctuations of temperature profiles of water inlet and outlet are caused by the on-of regulation of the electrical heater. The intensity of temperature fluctuation varies for each test and the reason is possible instability of the room temperature and power input. This problem can be solved by increasing the water bath volume to have a larger thermal mass and switch to a more precisely temperature controlled heater.

3.2.2. Discharging

Temperature profiles in the higher quadrant and lower quadrant during discharging are shown in Figs 3.16 and 3.17 for a HTF inlet temperature of 9°C and the HTF flow rate of 8L/min.

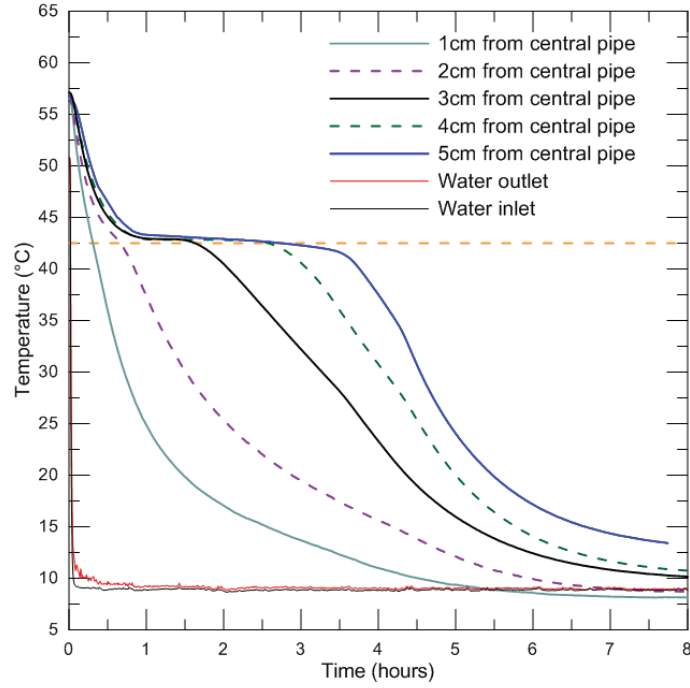


Figure 3.16: Temperature profiles of higher quadrants at a HTF inlet temperature of 9°C and HTF flow rate of 8L/min

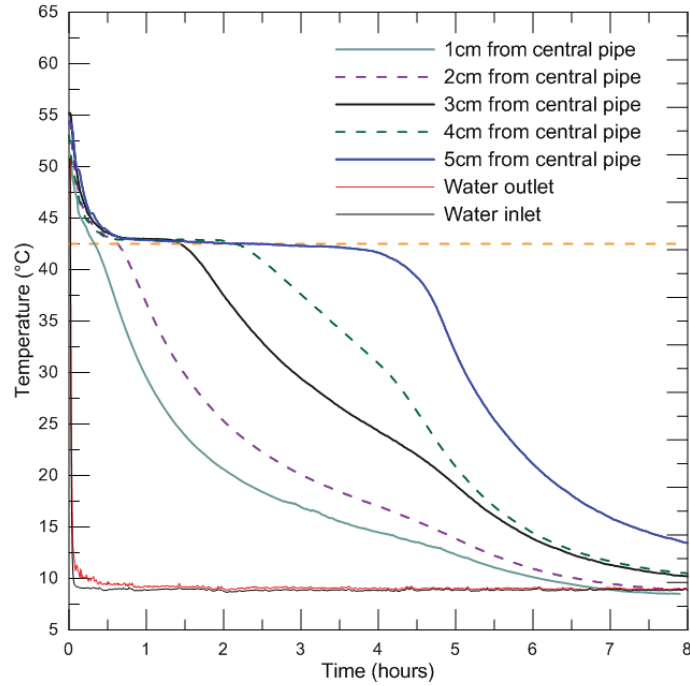


Figure 3.17: Temperature profiles of lower quadrants at a HTF inlet temperature of 9°C and HTF flow rate of 8L/min

No temperature plateau is observed for radial positions of 1cm and 2cm from the central pipe. One reason is that heat is extracted from the PCM rapidly at locations close to the central pipe

where cold HTF fluid pass through. Another reason is the possible delayed response from thermocouples; because of slight volume changes during solidification, leading to a void between the tip of the thermocouple and the PCM, hence poor thermal contact could cause a response delay. For locations farther away from the central pipe, temperature plateaus are clearly observed which reflects the isothermal nature of liquid-solid phase change.

Comparing Figs. 3.16 and 3.17, it is noted that lauric acid at the same location in higher and lower quadrants has similar melting temperature profiles. In addition, only small difference is observed for the melting time between higher and lower quadrants, which is different from what was observed for the charging process presented in section 3.2.1. The reason for the similar solidification pattern is that heat conduction is the dominant heat transfer mode during solidification of lauric acid. When cold HTF passes through the central pipe, solid PCM is formed on the surface of the pipe and later on fins. As discharging progresses, solid PCM accumulates on those surfaces; natural convection cannot be present in the solid PCM and therefore does not contribute to heat transfer enhancement. During charging, melted PCM around heat transfer surfaces is free to move, and the natural convection effect becomes more intense as more PCM is melted.

Therefore, the dominant heat transfer mode during discharging is heat conduction. This conclusion can be further validated comparing to a numerical model with pure conduction in section 4.2.2.

3.2.3. Solid-liquid Interface

From the results presented in the preceding two subsections, the solid-liquid interface position as a function of time can be inferred. Figure 3.18 presents the solid-liquid interface positions during charging and discharging. Figure 3.18 (a) validates the different intensity of natural convection between higher and lower quadrants.

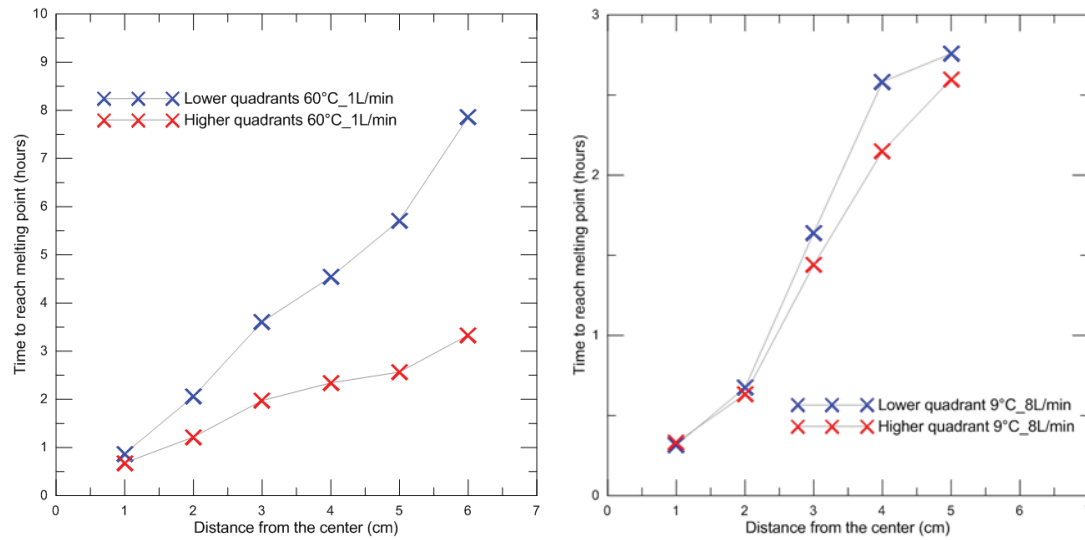


Figure 3.18: Solid-liquid interface location during a) charging with a HTF inlet temperature 60°C, HTF flow rate 1L/min; b) discharging with a HTF inlet temperature 9°C, HTF flow rate 8L/min

It is found in Fig. 3.18a) that during charging there is a clear difference in the solid-liquid interface position between higher and lower quadrants. The solid-liquid interface in higher quadrants moves faster which indicates a higher heat transfer rate compared with lower quadrants. This is a direct proof of the role of natural convection. However, in discharging process, the progression of the solid-liquid interface in both quadrants is similar which proves pure conduction dominates the discharging process.

3.3. The Impact of HTF Inlet Temperature

As mentioned at the beginning of this chapter, two primary experimental parameters are tested: HTF inlet temperature and HTF flow rate. In order to study the impact of HTF inlet temperature, tests at the same HTF flow rate are conducted and compared to eliminate the impact of HTF flow rates. A testing temperature range of 42.5°C to 60°C is first determined. There are two factors which limits this temperature range. First, the melting temperature of lauric acid is 42.5°C which requires the testing temperature to be above 42.5°C. Second, the maximum operation temperature of the PVC pipe is 60°C. Three temperatures are chosen in this range which also insures reasonable melting time for the tests.

Three hot HTF inlet temperatures were tested: 50°C, 55°C, and 60°C with a HTF flow rate of 1L/min. Figure 3.19 presents temperature profiles of T12 and T14. For T12 which is placed at the higher quadrant, a notable sharp rise of the temperature profile is observed after reaching the melting temperature. It can be explained that natural convection effect is more intense in the upper quadrants where two fins provide more heat transfer area. The time required for T12 to reach melting point are 1.9 hours and 5.3 hours respectively for HTF inlet temperatures of 60°C and 50°C.

Figure 3.20 presents temperature profiles of T11 and T13 which are situated at each lower quadrant. Being 2cm farther away from the central pipe than T11, T13 required extra time to reach the melting temperature. It is also found that for the same distance from the central pipe at upper and lower quadrants, faster melting and higher temperature are achieved in the higher quadrants. This validates the fact that natural convection is more intense in the upper quadrants.

Therefore, the impact of increasing HTF inlet temperature is reducing the complete charging time and achieving higher temperature in the higher quadrants. This can be explained by the following convection heat transfer equation,

$$q'' = hA(T_{HTF} - T_{pipe,wall}) \quad (3.2)$$

Where q'' is the heat flux transferred to the PCM from the HTF, h is the convection heat transfer coefficient, T_{HTF} and $T_{pipe,wall}$ are the temperature of the HTF and the copper pipe wall respectively. A higher HTF inlet temperature will lead to a higher temperature difference between the PCM and water. More heat is transferred to the LHESS per unit time. The increased heat transfer caused by the larger temperature difference promotes faster melting at the beginning of charging. This results in more liquid PCM sooner, which in turn leads to a faster onset of natural convection.

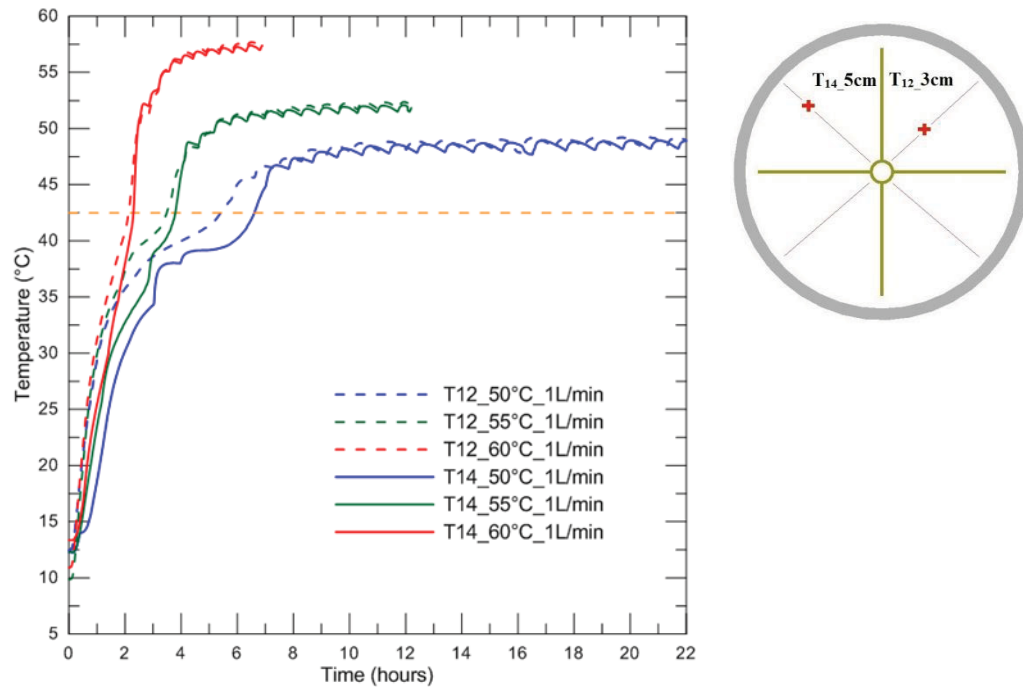


Figure 3.19: HTF inlet temperature effect on T12 and T14 (50°C_1/min, 55°C_1L/min and 60°C_1/min)

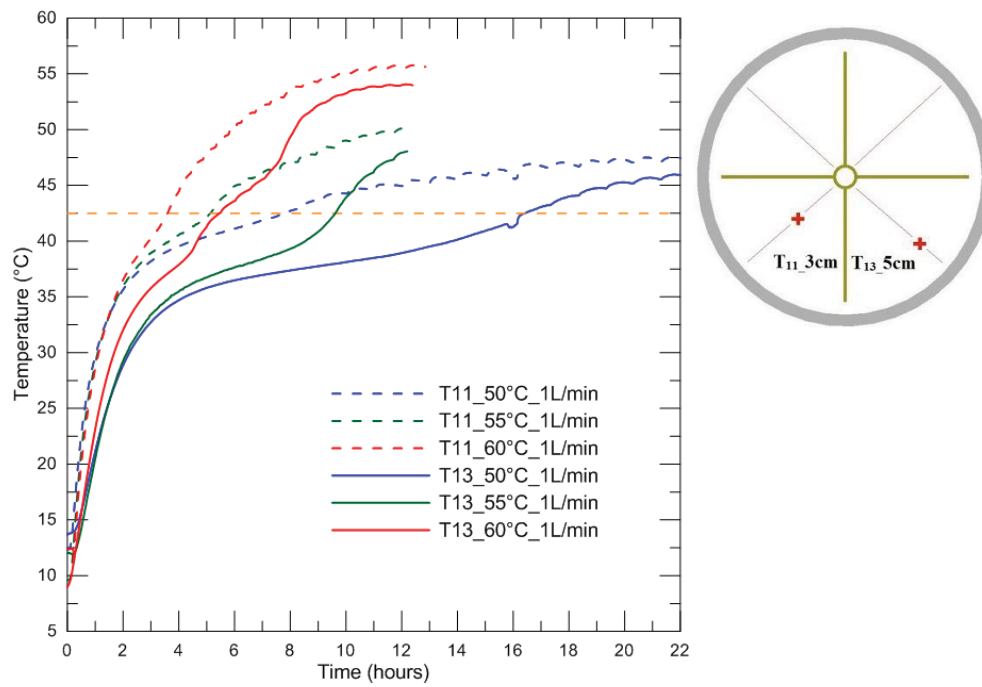


Figure 3.20: HTF inlet temperature effect on T11 and T13 (50°C_1/min, 55°C_1L/min and 60°C_1L/min)

Figures 3.21 to 3.24 show temperature profiles of T11 to T14 in each quadrant at different HTF inlet temperatures with a HTF flow rate of 3.5L/min and a HTF flow rate of 5.5L/min. Increasing HTF inlet temperature leads to a higher driven temperature difference between lauric acid and HTF. The total time required for complete melting is affected by this driven temperature difference. A higher HTF inlet temperature reduced the complete charging time.

The same trend as observed in the previous tests (1 L/min) is observed here, only on a smaller time scale at a HTF flow rate of 3.5 and 5.5 L/min.

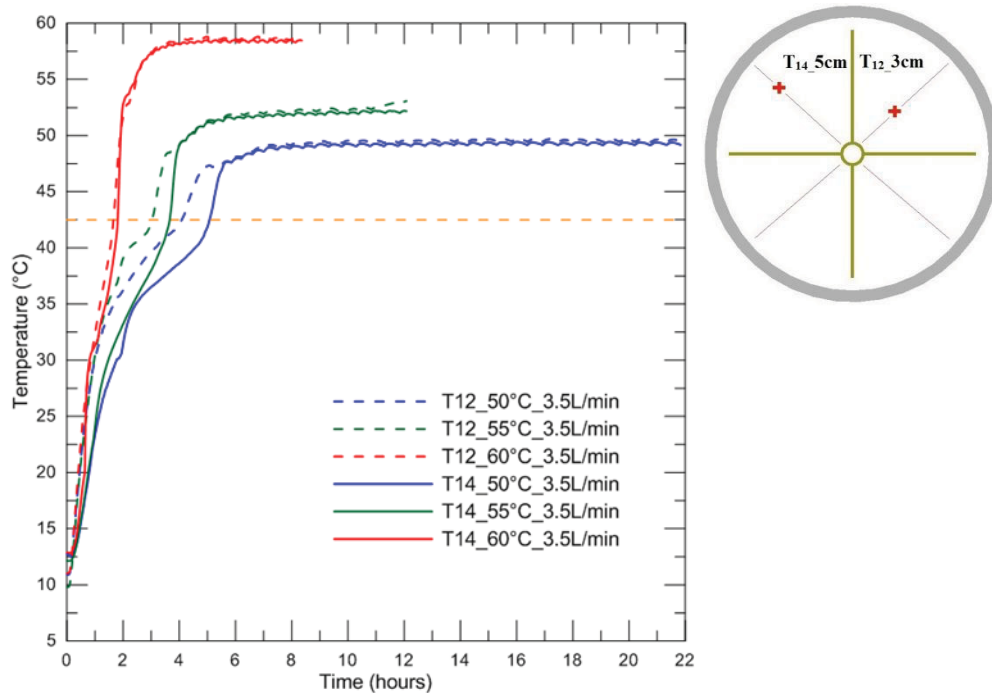


Figure 3.21: HTF inlet temperature effect on T12 and T14 (50°C_3.5/min, 55°C_3.5 L/min and 60°C_3.5/min)

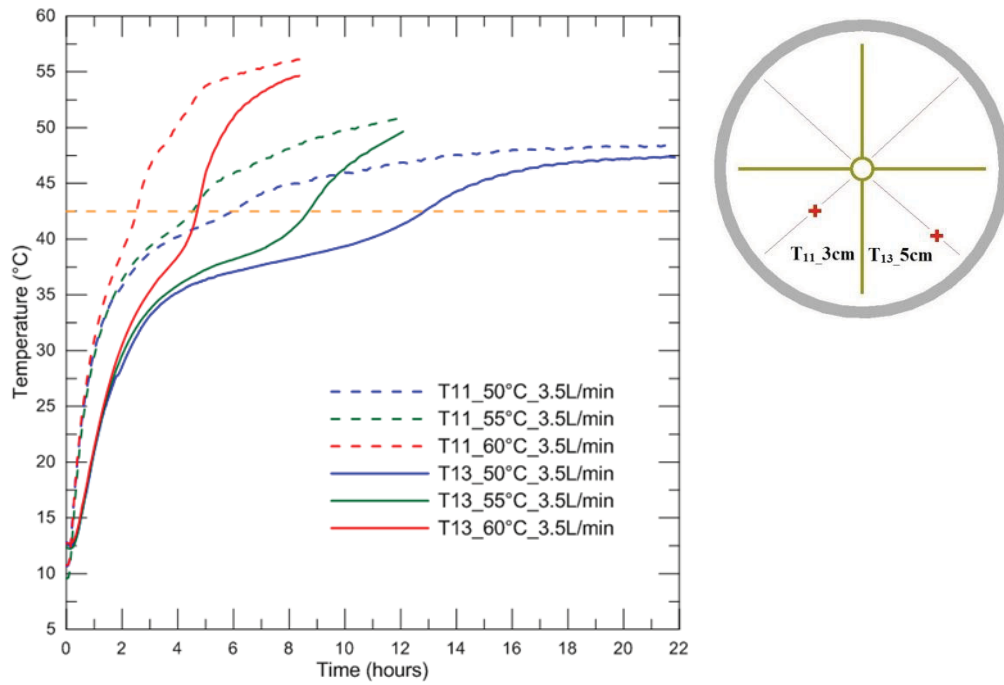


Figure 3.22: HTF inlet temperature effect on T11 and T13 (50°C_3.5/min, 55°C_3.5 L/min and 60°C_3.5/min)

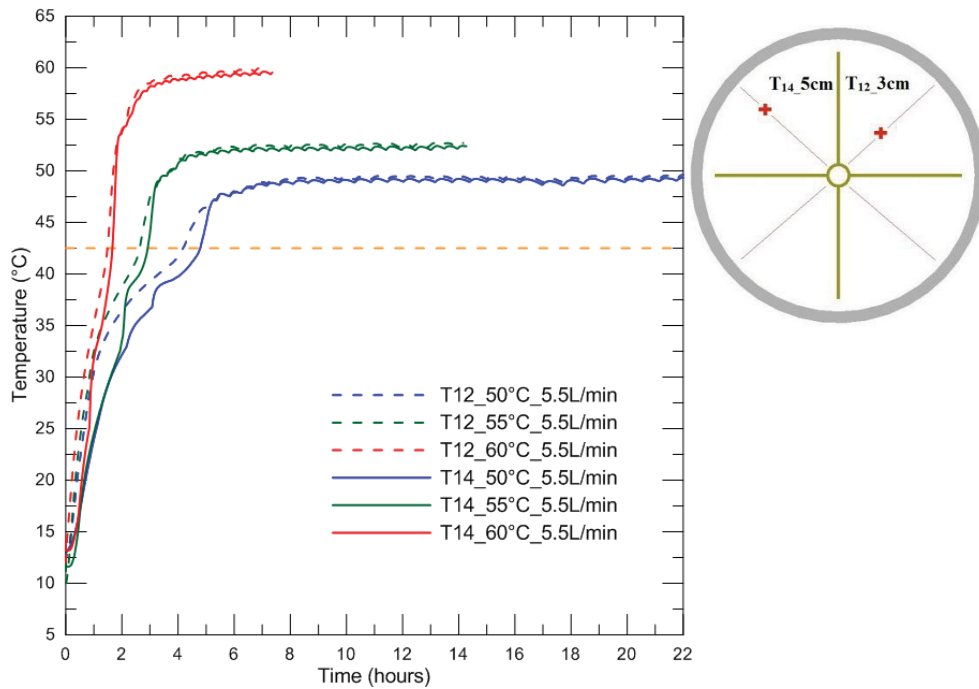


Figure 3.23: HTF inlet temperature effect on T12 and T14 (50°C_5.5/min, 55°C_5.5 L/min and 60°C_5.5/min)

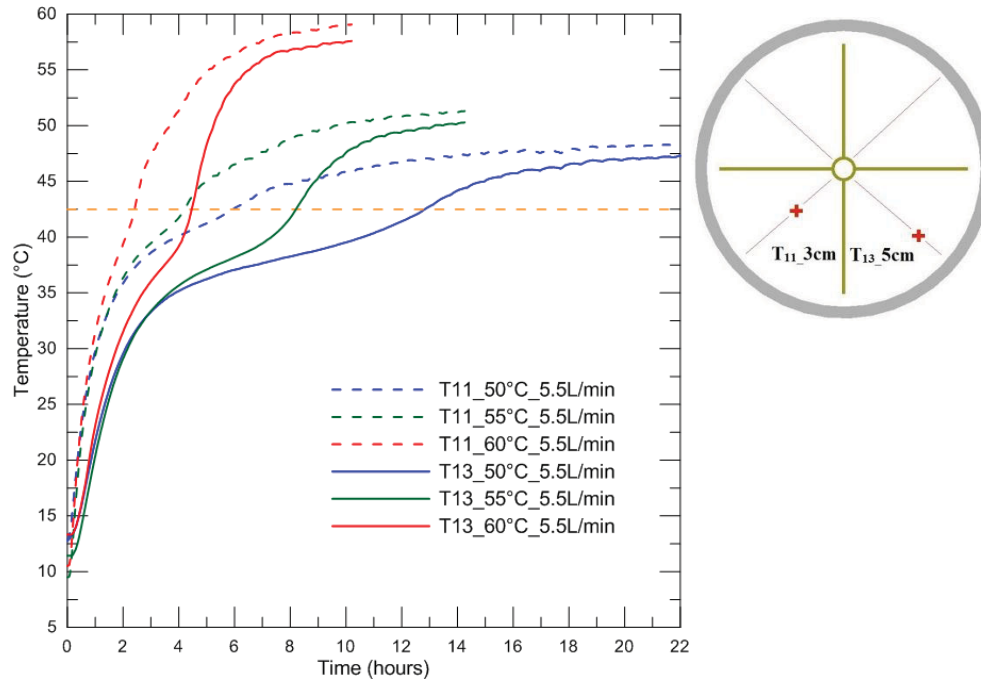


Figure 3.24: HTF inlet temperature effect on T11 and T13 (50°C_5.5/min, 55°C_5.5 L/min and 60°C_5.5/min)

3.4. The Impact of HTF Flow Rates

3.4.1. Charging

In order to study the HTF flow rate impact on melting of lauric acid, three tests were conducted with HTF inlet temperature of 55°C which are presented in Figs. 3.25 and 3.26.

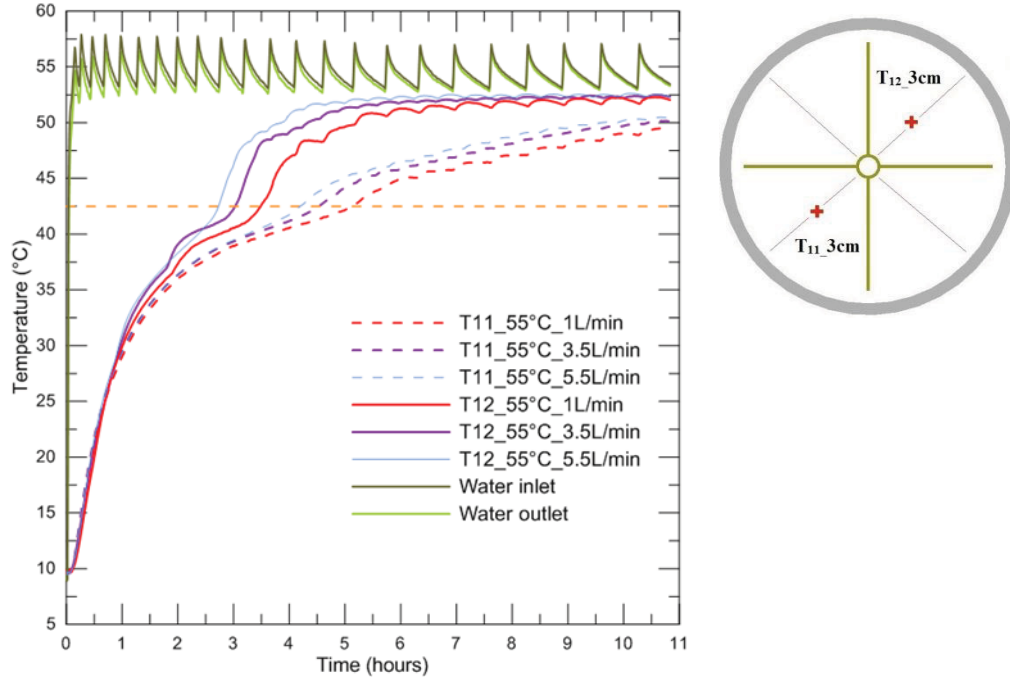


Figure 3.25: HTF flow rate effect at T11 and T12 (55°C_1 L/min, 55°C_3.5 L/min and 55°C_5.5 L/min)

It is noted that at the initial stage of melting, which is conduction-dominant, increasing the HTF flow rate does not have any effect on heat transfer rate. The temperature profiles are independent of HTF flow rate at this stage. Afterwards, when natural convection starts to enhance heat transfer and more phase change occurs, increasing the HTF clearly leads to a slightly faster melting rate. The reason is that higher forced convection coefficient (see Table 4.1) is achieved on the HTF side by increasing the HTF flow rate. Although the largest thermal resistance exists in the PCM side, the thermal resistance on the HTF side is reduced. The PCM close to heat transfer surfaces melts faster which results in an earlier onset of natural convection which increases the melting rate inside the PCM.

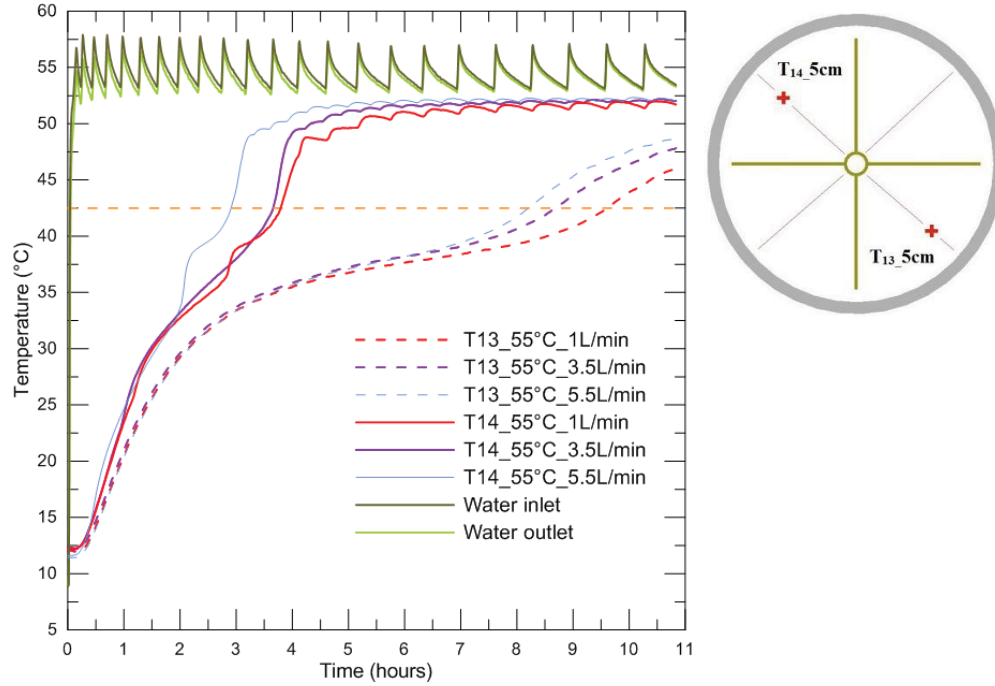


Figure 3.26: HTF flow rate effect at T13 and T14 (55°C_1 L/min, 55°C_3.5 L/min and 55°C_5.5 L/min)

3.4.2. Discharging

Various HTF flow rates for discharging were tested from 1 L/min to 12 L/min (Fig. 3.27). It is noticed that the HTF flow rate has a fairly small effect on the temperature profiles. T11 and T12 have almost the same temperature profile which indicates that natural convection does not play a significant role during discharging.

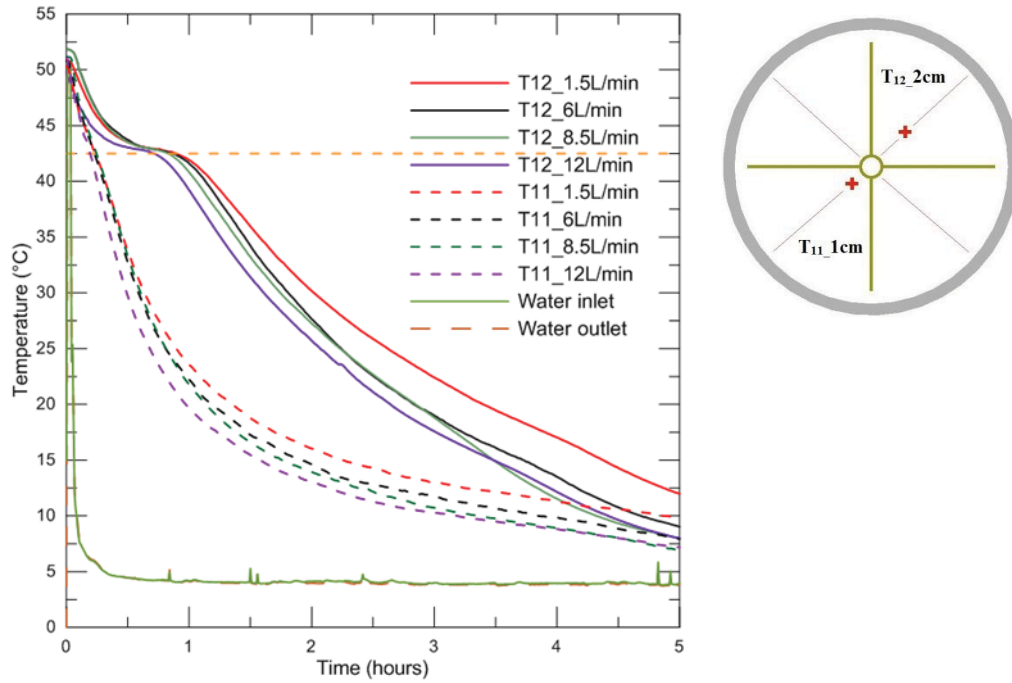


Figure 3.27: HTF flow rate effect on T11 and T12

Figures 3.28 and 3.29 show HTF flow rate effects on discharging at other locations. A temperature plateau is observed at all thermocouples. It is also found that discharging rate is higher before reaching solidification, and the rate is decreased after all PCM is solidified. The reason is as solidification progresses, the temperature difference between lauric acid and HTF decreased which slow down the discharging rate.

The observed solidification temperature for lauric acid in this study is 42.5°C which indicates that no supercooling is present during discharging.

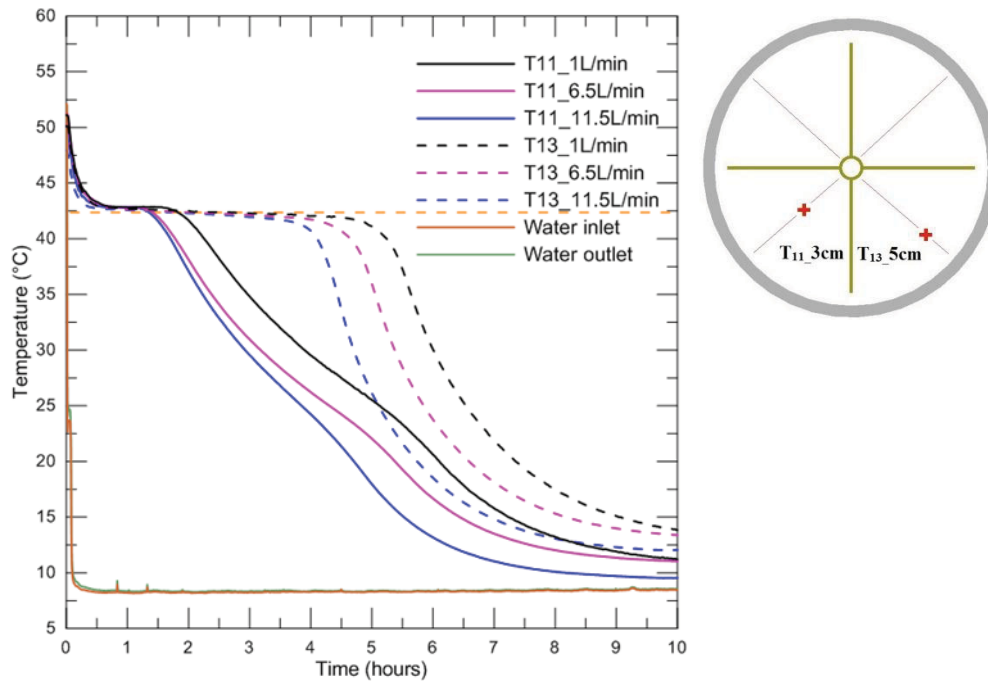


Figure 3.28: HTF flow rate effect on T11 and T13 (9°C_1 L/min, 9°C_6.5 L/min and 9°C_11.5 L/min)

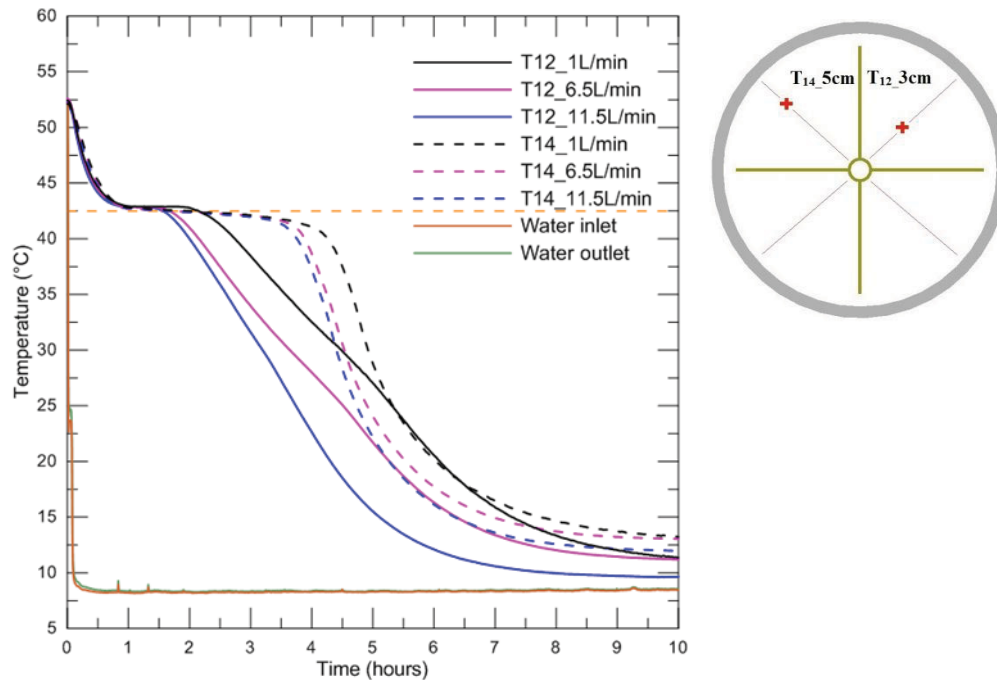


Figure 3.29: HTF flow rate effect on T12 and T14 (9°C_1 L/min, 9°C_6.5 L/min and 9°C_11.5 L/min)

3.5. Complete Charging and Discharging Time

The total time required for complete melting varies for different HTF flow rates and HTF inlet temperatures. The melting time of nine tests which all started at the same temperature (10°C) are presented in Fig. 3.30.

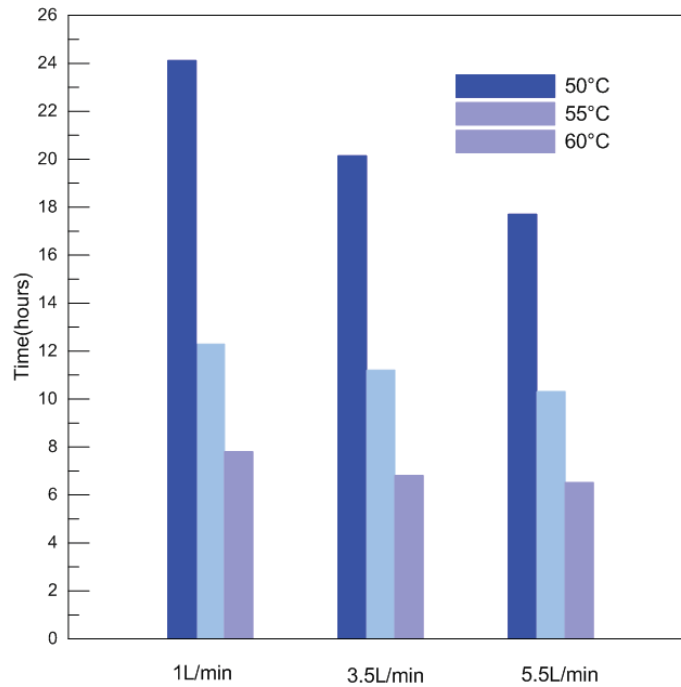


Figure 3.30: Melting time for various HTF inlet temperatures at different HTF flow rates

It is noted that for a HTF inlet temperature of 60°C, complete melting time is in a range of six to eight hours for HTF flow rates between 1 L/min to 5.5 L/min. More time is needed for HTF inlet temperatures of 50°C and 55°C.

For a HTF inlet temperature of 50°C which is only a slightly higher temperature than the melting point, the complete melting time for 1 L/min HTF flow rate is 24.1 hours. For the same HTF flow rate but a different HTF inlet temperature (60°C), the complete charging time is reduced to eight hours.

In the experiments, it is observed that a small portion of lauric acid at the bottom of the lower quadrants takes approximately one extra hour to melt which increases the complete charging

time of this LHESS. The reason is natural convection effect displaces the heat to the upper region of the lower quadrants. This leads to less heat available to melt the PCM at the very bottom part of the container.

The driving temperature difference between PCM and HTF is relatively high, and this driving temperature difference is the dominant contributing factor in determining the complete melting time. Increasing HTF flow rate results in a higher heat transfer coefficient which leads to more energy transferred to PCM. However, the HTF flow rate has less impact on the total melting time in comparison of driving temperature difference between the PCM and the HTF.

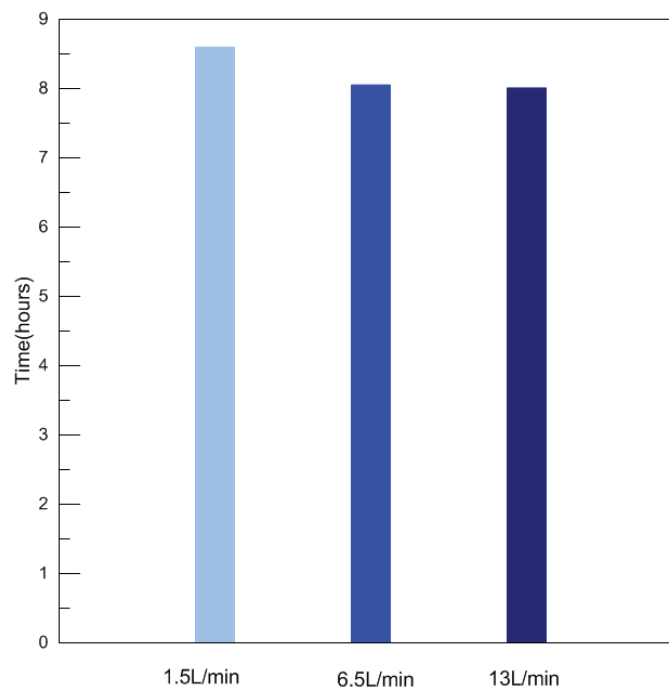


Figure 3.31: Solidification time for different HTF flow rates

Figure 3.31 shows solidification time for three HTF flow rates at the same HTF inlet temperature of 9°C. The solidification time does not change greatly by varying HTF flow rates. This also validates the statement that during discharging, HTF flow rates have minimal impact on temperature profile and discharging time.

3.6. Thermal Response

In order to study the phase change behavior right after charging, a full charging and discharging process was performed in the same test. Municipal cold water was used to discharge the LHESS right after it achieved complete melting. The results are presented in Fig. 3.32.

At the beginning of discharging, the temperatures of T10 to T14 decrease rapidly. The reason is the discharging process begins at around 60 °C which indicates liquid state of all lauric acid. When municipal cold water is circulated in the LHESS, the large temperature difference acting as a driving force dissipates sensible heat from lauric acid rapidly. The calculated power output during the discharging process is shown in Table 3.1. It is noticed that before solidification, the discharging rate is highest. The reason is higher temperature difference between cold water and the PCM. Then the discharging rate slowed down as this temperature difference decreased. The PCM solidifies at a temperature of 42.5 °C which indicates no supercooling for the discharging process. After phase change, the temperature at those locations decreases rapidly again because only sensible heat is extracted from the PCM.

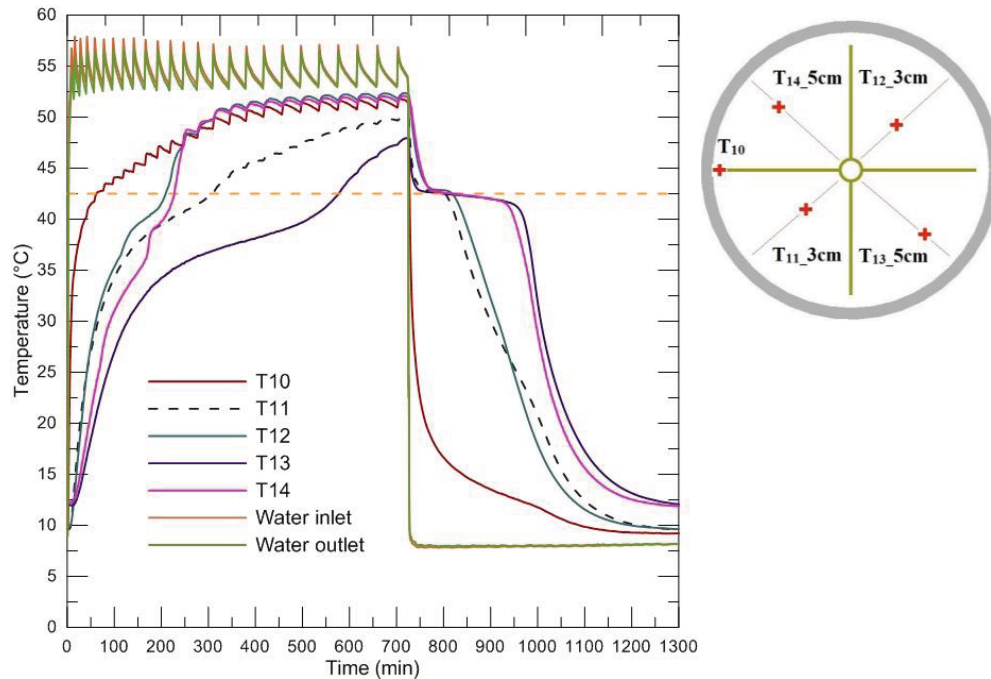


Figure 3.32: Thermal responses for charging with a HTF inlet temperature of 55°C and HTF flow rate of 1 L/min, discharging with a HTF inlet temperature of 9°C and HTF flow rate of 11.5 L/min

Table 3.1: Power output during discharging

Temperature range	Energy type	Energy amount (kJ)	Time (mins)	Power (W)
60-42.5°C	sensible heat	171.36	40	71.4
42.5 °C	latent heat	742.56	220	56.3
42.5-9 °C	sensible heat	367.2	300	14.7

3.7. Energy Storage Capacity

3.7.1. Theoretical Energy Storage

The maximum thermal energy storage capacity of this LHESS includes sensible heat and latent heat. The initial temperature of PCM is 10°C for all charging tests, and sensible heat storage can be calculated as

$$q_{sensible} = m_{pcm} \cdot c_p \cdot \Delta T \quad (3.3)$$

where m_{pcm} is the total mass of lauric acid in the LHESS (4.08 kg), c_p is the specific heat of lauric acid (W/mK), ΔT is the temperature difference between the initial temperature and final temperature of lauric acid.

Latent heat storage capacity can be calculated by applying the following equation,

$$q_{latent} = m_{pcm} \times L \quad (3.4)$$

where L is the latent heat of fusion of lauric acid. The latent heat capacity is 742.56 kJ in this system. Total theoretical thermal energy storage capacities for three hot HTF inlet temperatures are shown in Fig. 3.33, and in each case the final temperature of PCM is the same as the HTF inlet temperature. Calculation for sensible heat and latent heat is shown in Table 3.1.

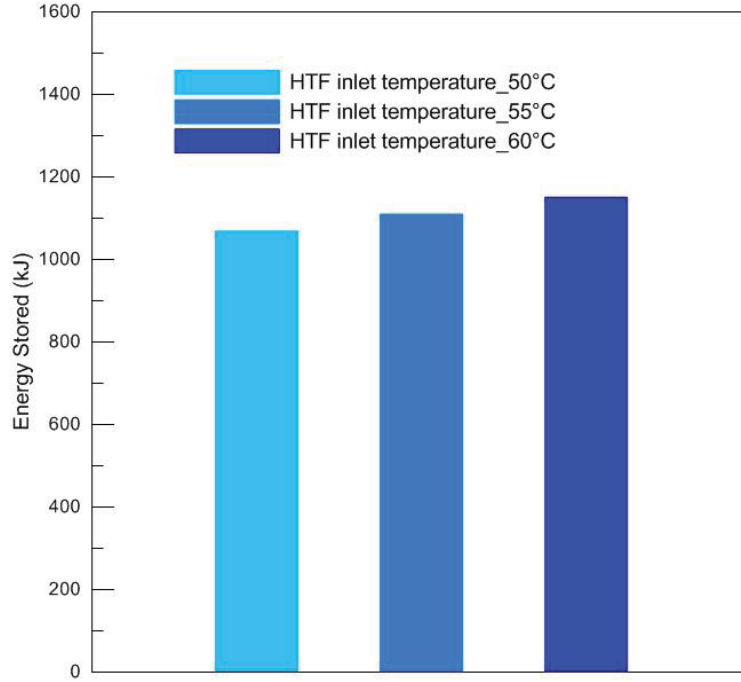


Figure 3.33 Maximum heat storage capacities for various HTF inlet temperatures

3.7.2. Energy Supplied

Energy is transferred to PCM by water which flows through the copper pipe in the center of the container. The total energy supplied to the system can be calculated using the following equations,

$$\dot{q}_s = \dot{m}_{water} \cdot c_p \cdot (T_{in} - T_{out}) \quad (3.5)$$

$$q_{total} = \sum_{i=0}^n t_n \dot{q}_s \quad (3.6)$$

Where \dot{q}_s is energy supplied every second (J/s), \dot{m}_{water} is mass flow rate of PCM (kg/s), q_{total} is total energy supplied (J), t_n is the time interval during experimental tests (s). Temperatures of water inlet and outlet are recorded by T15 and T16 respectively.

3.7.3. Heat Loss

The PCM container is insulated with glass wool and Reflectix bubble insulation. However, the operating temperature of HTF is between 50 to 62°C which is higher than the room temperature (20°C). Heat loss then is calculated as follows:

$$q'' = k_{plexiglas} \frac{\Delta T}{L} \quad (3.7)$$

$$q_{loss} = q'' \times A \times t_{total} \quad (3.8)$$

Where q'' is the heat flux (W/m^2), $k_{plexiglas}$ is the thermal conductivity of the plexiglas which is 0.17 W/mK (goodfellow.com), ΔT is the measured temperature difference between T6 and T7 (in a typical range of 0.5 to 3°C), L is the thickness of the plexiglas which is 0.00635 m , q_{loss} is the total heat loss (W), A is the area of PCM container which is 0.146 m^2 .

An example of energy supplied for an HTF inlet temperature of 60°C and a flow rate of 1 L/min is shown in Fig. 3.34. For the same test, the heat loss is also presented in Fig. 3.34. It is noted that heat loss rate is more rapid as time increases. This occurred due to the fact that PCM container was heating up during this time, therefore the temperature difference between LHESS system and ambient air was increased. However, during charging, the heat loss is less than an order of magnitude of energy supplied, it is reasonable to neglect heat loss.

During the first half of melting process (the complete melting time is seven hours), the amount of energy supplied increases linearly. Afterwards, the increase rate slows down until fully melted. The reason is heat loss increases at the final stage of charging which is seen from Fig. 3.34. After seven hours, lauric acid is completely melted and energy supplied for LHESS serves for two purposes: increasing the sensible heat of liquid lauric acid and balancing heat losses to the ambient.

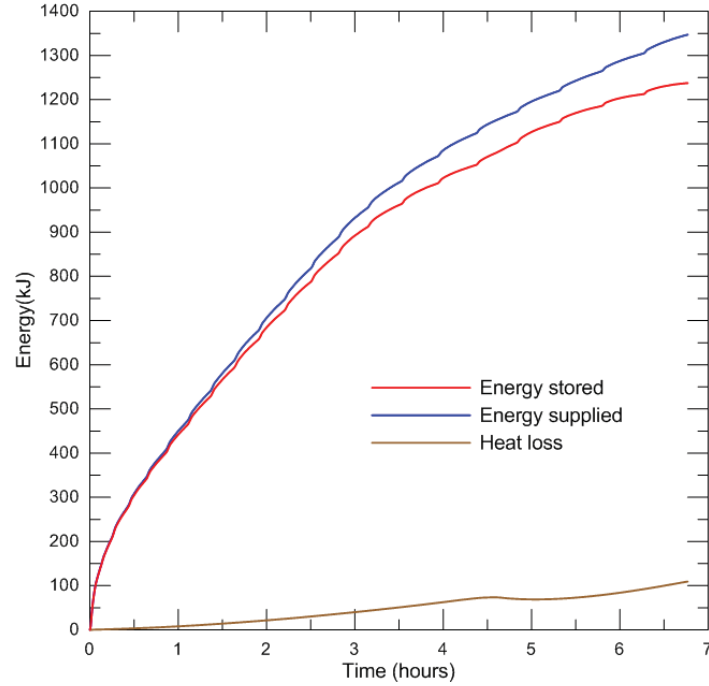


Figure 3.34: Energy supplied, stored and heat loss at a HTF inlet temperature of 60°C, HTF flow rate 1 L/min

3.7.4. Experimental Uncertainty of Energy Stored

Energy stored in the LHESS is calculated by deducting the total heat loss from the total energy supplied. An experimental uncertainty analysis was conducted for the same test presented in Fig. 3.35. The experimental uncertainty of the total energy stored is calculated using the method described in section 2.6.1 leading to an uncertainty of $\pm 49\%$. The primary reason for this large uncertainty is temperature difference between the water inlet and water outlet is quite small (less than 1°C) compared with thermocouple readings (between 50°C to 60°C after stabilization).

In order to quantify the experimental uncertainty from another point of view, theoretical energy storage is calculated by adding up theoretical sensible heat storage and theoretical latent heat storage. In Fig. 3.35, the total energy supplied experimentally (including heat loss) is presented as the solid blue line while the stored energy (excluding heat loss) is shown as the solid green line. The theoretical energy storage is compared with experimental results and excellent agreement is found. As a consequence, the experimental results are validated.

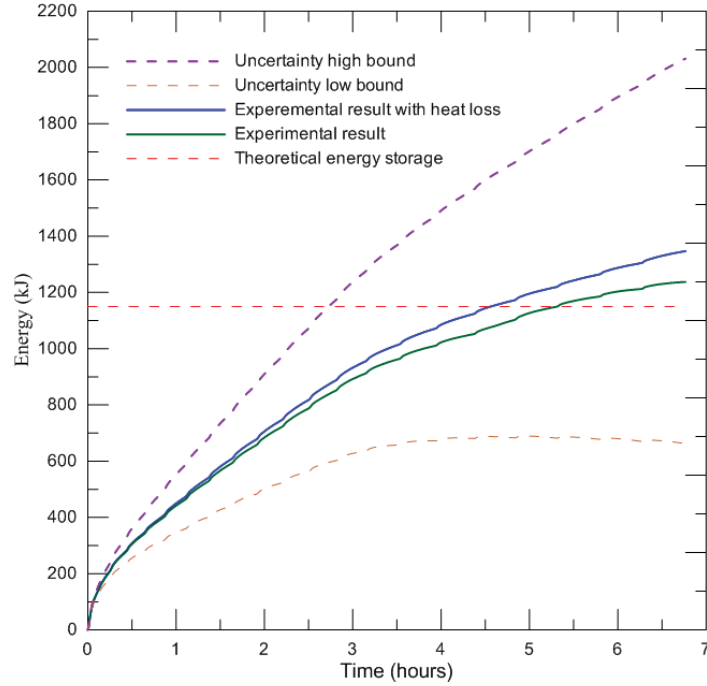


Figure 3.35: Uncertainty of energy stored with a HTF inlet temperature at 60°C, HTF flow rate 1 L/min

3.8. Conclusion

In conclusion, it is found that natural convection plays a major role during charging. Faster melting and higher temperatures are achieved in higher quadrants compared to lower quadrants. During discharging, solid lauric acid accumulates on the heat transfer surfaces which limit natural convection. The dominant heat transfer mechanism during discharging is conduction.

It is also observed that the melting time is directly affected by the HTF inlet temperature; the higher the temperature is, the shorter time it takes to complete melting. During charging, increasing HTF flow rate can increase the heat transfer rate and reduces the complete melting time, but this impact on charging time is minimal. However, for discharging time, changing HTF flow rates have minimal impact.

CHAPTER 4 : NUMERICAL RESULTS FOR STRAIGHT FIN CONFIGURATION

4.1. Numerical Model Introduction

COMSOL Multiphysics 4.2a is used to simulate phase change processes inside a model representing a 2D slice of the cylindrical LHESS used for the experimental work. The geometry of the numerical model is shown in Fig. 4.1. Because of the validated symmetry assumption, only half of the cylindrical system is needed. All the properties of lauric acid can be found in Chapter 2. Properties of copper are already present in COMSOL's built-in materials library. The insulation in the numerical model is limited to the ¼” acrylic plastic (green part in Fig. 4.1). All COMSOL models are simulated using a Dell Precision T1600 workstation with 4 GB of memory and running an Intel Quad Core Xeon processor at 3.10 GHz.

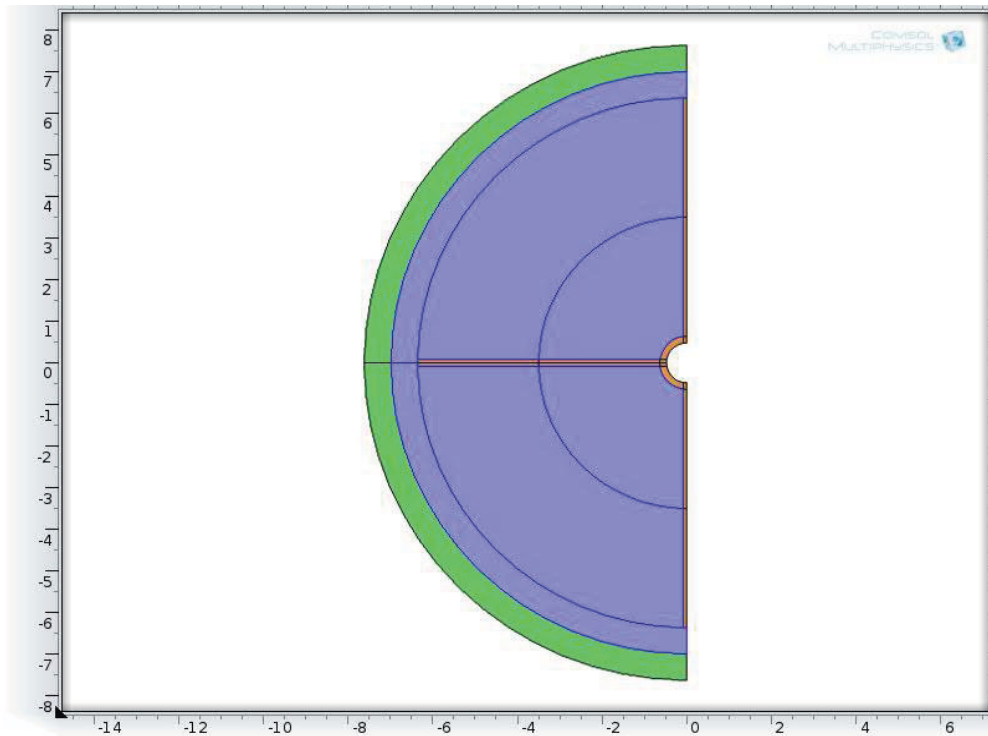


Figure 4.1: Geometry of the numerical model

The following assumptions were made to simplify the numerical model:

1. Liquid lauric acid is newtonian and incompressible;
2. The flow is two dimensional;

3. Heat transfer at the solid-liquid interface is not strongly affected by thermal expansion of the PCM during melting;
4. The flow caused by natural convection flow is laminar.

The heat transfer and laminar flow physics were used in COMSOL to simulate the thermo fluid and phase change processes. There are three heat transfer mechanisms that must be considered in such system: conduction, natural convection and phase change heat transfer.

4.1.1. Heat Conduction

At the onset of PCM melting, heat is transferred from the hot surface (central pipe and fins) to the PCM in its solid phase by heat conduction. Heat conduction is also present in the copper fins and in the solid PCM. The energy equation for this process is:

$$\rho c_p \frac{\partial T}{\partial t} = k \nabla^2 T \quad (4.1)$$

where ρ is the density of the material, c_p is the specific heat, k is the thermal conductivity and T is the temperature. A time derivative is found in that equation since this problem is transient in nature.

4.1.2. Natural Convection

When enough PCM material has melted, liquid PCM will start circulating between the hot fins and the liquid-solid interface, giving rise to natural convection heat transfer. From this point on, the shape of the liquid-solid interface will be determined by the effect and magnitude of natural convection in the liquid melt.

In order to model convection only in the liquid PCM, the dynamic viscosity μ was input as a piecewise, continuous second derivative function centered on T_m (Fig. 4.2). This accounted for the viscosity of the liquid PCM in the melted region and forced the solid PCM to remain fixed by having a solid viscosity 10^8 times larger than the liquid one (Murray and Groulx, 2011).

A volume force was also added to the model to provide the driving force for natural convection in the liquid PCM using the following equation:

$$F = g\rho\alpha(T - T_0) \quad (4.2)$$

where g is gravity, α is the thermal expansion coefficient for lauric acid, T_0 is the reference temperature at which the density is selected in the Boussinesq approximation and T is the local temperature in the liquid PCM.

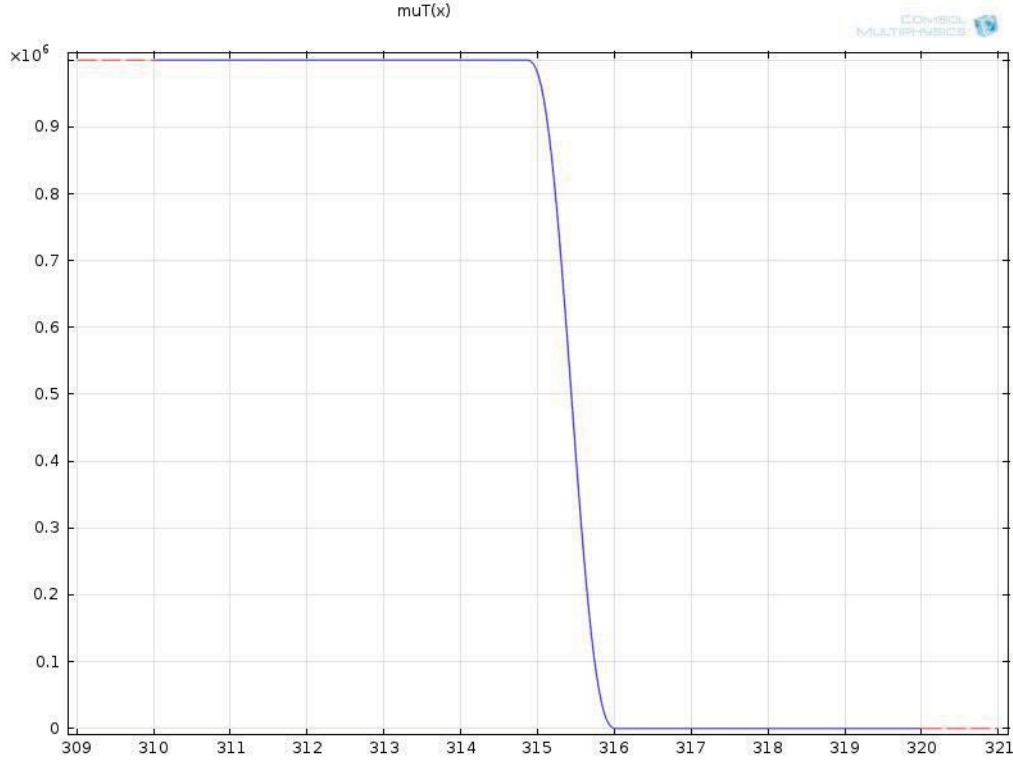


Figure 4.2: Dynamic viscosity of lauric acid in numerical models

4.1.3. Phase Change Heat Transfer

A large amount of energy must be provided to melt a PCM. In order to account for this latent heat present over the melting temperature range of the PCM, the specific heat of the PCM is modified using a piecewise function, following the method presented by Ogoh and Groulx (2010).

In this numerical model, lauric acid is taken to melt between the temperature of 315 and 316 K and it has a latent heat of fusion of 182 kJ/kg. The lauric acid specific heat is then modified over this 1 K melting temperature range to account for the total amount of latent heat required to melt

the material. To do so, the following equation is manually input into the model for the specific heat of lauric acid (Fig. 4.3):

$$C_p = \begin{cases} C_{ps} = 2.4 \text{ kJ/kg} & T \leq 315 \text{ K} \\ C_p = [(C_{ps} + C_{pl})/2 + L]/\Delta T = 184.2 \text{ kJ/kg} & 315 \text{ K} < T < 316 \text{ K} \\ C_{pl} = 2.4 \text{ kJ/kg} & T \geq 316 \text{ K} \end{cases} \quad (4.3)$$

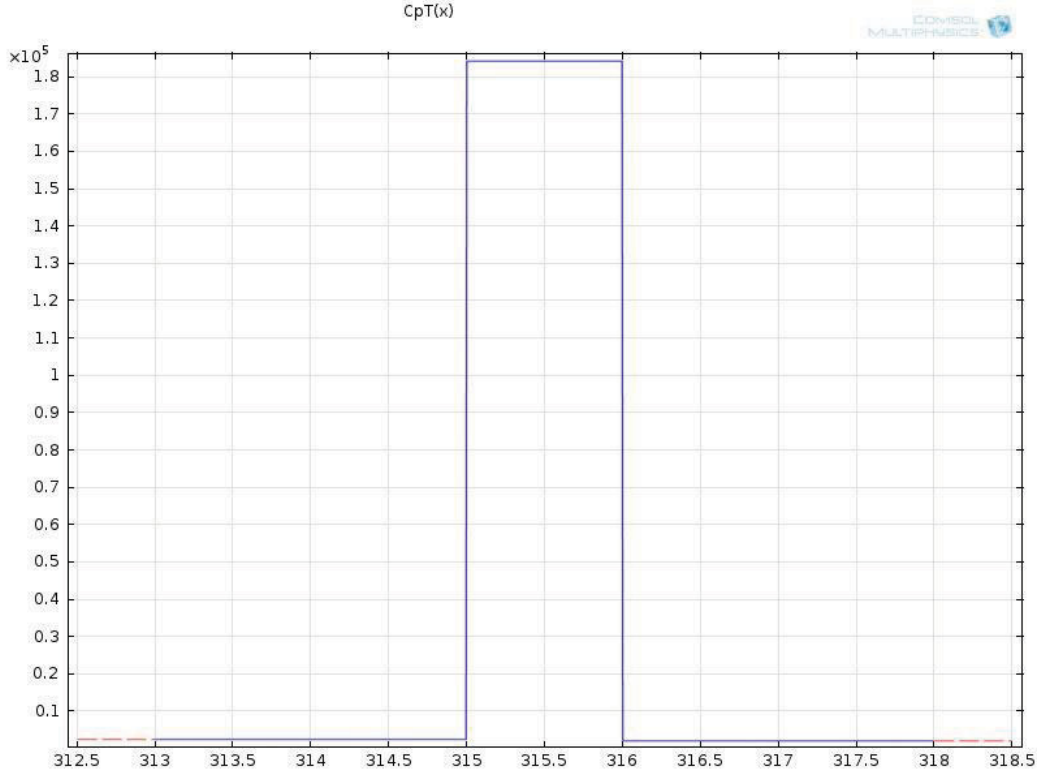


Figure 4.3: The specific heat of lauric acid in numerical models

4.1.4. Boundary Conditions

In this model, the boundary condition on the outside surface is insulated. This is a simplifying assumption, but with the small amount of heat losses from the system (see Chapter 3), results obtained will still be highly representative. Two boundary conditions were applied on the inner surface of the pipe. The first boundary condition used is constant temperature, with the hot HTF inlet temperature used. The other boundary condition used is a convective heat flux; this constant heat flux corresponds to the forced convection heat transfer from the hot HTF fluid, as in the experiments. Parameters needed to calculate the heat transfer coefficient are shown as following:

$$Re_d = \frac{4\dot{m}}{\pi \cdot D \cdot \mu} \quad (4.4)$$

where Re_d is the Reynolds number, \dot{m} is the mass flow rate of HTF, D is the diameter of the central pipe, and μ is the viscosity of HTF. A correlation developed by Gnielinski is used to calculate the Nusselt number,

$$Nu = \frac{(f/8)(Re_d - 1000) \cdot Pr}{1 + 12.7 \times (f/8)^{0.5} \times (Pr^{\frac{2}{3}} - 1)} \quad (4.5)$$

$$\left[\begin{array}{l} 0.5 \leq Pr \leq 2000 \\ 3000 \leq Re_d \leq 5 \times 10^6 \end{array} \right]$$

where Nu is the Nusselt number, f is the friction factor of the pipe, Pr is the Prandtl number of water. A single correlation has been developed for friction number calculation of a smooth pipe for turbulent flow (Incropera et al., 2005):

$$f = (0.790 \ln Re_d - 1.64)^{-2} \quad (4.6)$$

$$[3000 \leq Re_d \leq 5 \times 10^6]$$

For laminar flow ($Re_D < 3000$), the following equation can be used (Incropera et al., 2005):

$$f = 0.316 Re_D^{-0.25} \quad (4.7)$$

The assumption of a smooth pipe was used since the Re_D encountered are small enough that the impact of low surface roughness would not affect the calculated f significantly.

The heat transfer coefficient h is then found from:

$$h = Nu \frac{k}{D} \quad (4.8)$$

Heat transfer coefficients for charging and discharging are presented in Table 4.1 and Table 4.2. The average temperature of municipal cold water is 9°C during the tests and heat transfer coefficients for discharging are calculated based on water properties at this average temperature.

Table 4.1: Heat transfer coefficients for charging

HTF inlet temperature flow rate	Re_D	f	Nu	h (W/m ² ·K)
50°C_1 L/min	2865.88	0.043	15.26	770
50°C_3.5 L/min	10030.59	0.031	58.03	2929
50°C_5.5 L/min	15762.36	0.028	86.36	4359
55°C_1 L/min	3116.30	0.045	18.39	935
55°C_3.5 L/min	10907.05	0.031	64.84	3298
55°C_5.5 L/min	17139.65	0.027	96.33	4900
60°C_1 L/min	3364.56	0.043	20.84	1109
60°C_3.5 L/min	11775.96	0.030	72.09	3701
60°C_5.5 L/min	18505.08	0.026	107.05	5496

Table 4.2: Heat transfer coefficients for discharging

HTF inlet temperature flow rate	Re_D	f	Nu	h (W/m ² ·K)
9°C_1 L/min	1197.68	0.063	3.08	142
9°C_2 L/min	2395.36	0.049	18.63	858
9°C_3 L/min	3593.04	0.042	31.81	1465
9°C_4 L/min	4790.73	0.039	43.93	2023
9°C_5 L/min	5988.41	0.036	55.39	2551
9°C_6 L/min	7186.09	0.0346	66.39	3058
9°C_7 L/min	8383.77	0.033	77.04	3549
9°C_8 L/min	9581.46	0.031	87.42	4027
9°C_9 L/min	10779.14	0.030	97.56	4494
9°C_10 L/min	11976.82	0.0291	107.52	4952
9°C_11 L/min	13174.51	0.029	117.30	5403
9°C_12 L/min	14372.19	0.028	126.94	5847

4.1.5. Mesh Convergence Study

A mapped mesh was used for better control of the element shape and size. A convergence study was performed in order to determine the optimum number of elements needed to minimize simulation time and maintain the highest level of accuracy. Simulations with different distribution of elements in mapped mesh were performed. The temperature of T11, located 3 cm away from the lower quadrant, is shown in Fig. 4.4 and the melting fraction of lauric acid is present in Fig. 4.5.

Results show that an amount of elements above 456 all have high accuracy level for this model with pure conduction. For numerical models with both conduction and convection, more complicated modules are used and more parameters are included. Therefore, a finer mesh to simulate models with convection is required for higher accuracy. However, finer mesh will requires a longer computational time. For instance, a model with a HTF inlet temperature of 60°C and HTF flow rate of 1 L/min was simulated with both conduction and convection (4416 elements). It took approximately seven days for this numerical simulation to achieve complete melting which is considered as a reasonable computational time. Taking the computational time into consideration, meshes using more than 4416 elements are unpractical. Consequently, the mesh with 4416 elements is chosen as an optimised mesh (Fig. 4.6).

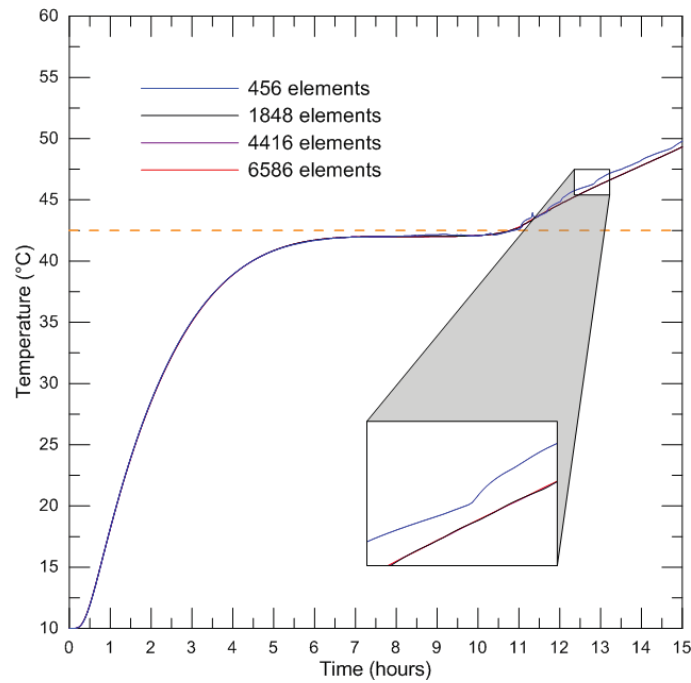


Figure 4.4: Temperature profile of T11 with different amount of elements (simulation of pure conduction test with a HTF inlet temperature of 60°C and flow rate of 1 L/min)

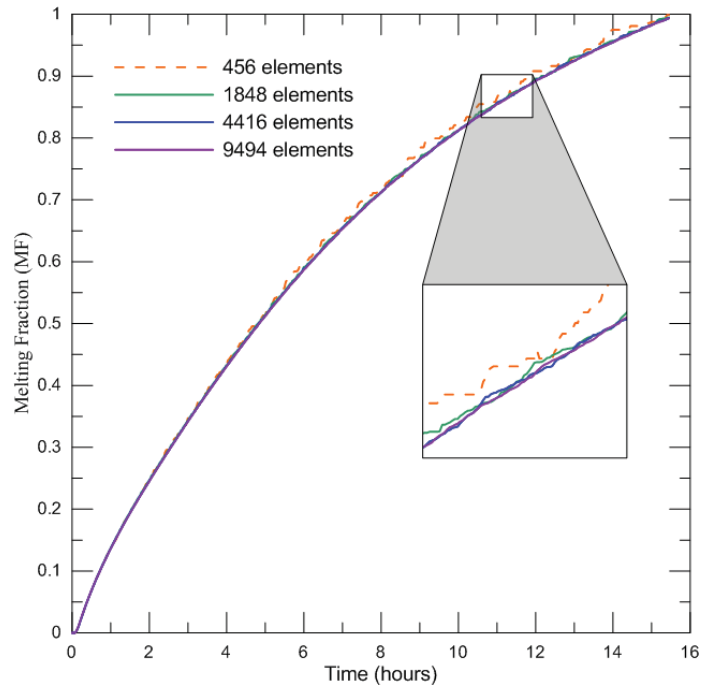


Figure 4.5: Melting fraction of the PCM as a function of time for different amount of elements(simulation of pure conduction test with a HTF inlet temperature of 60°C and flow rate of 1 L/min)

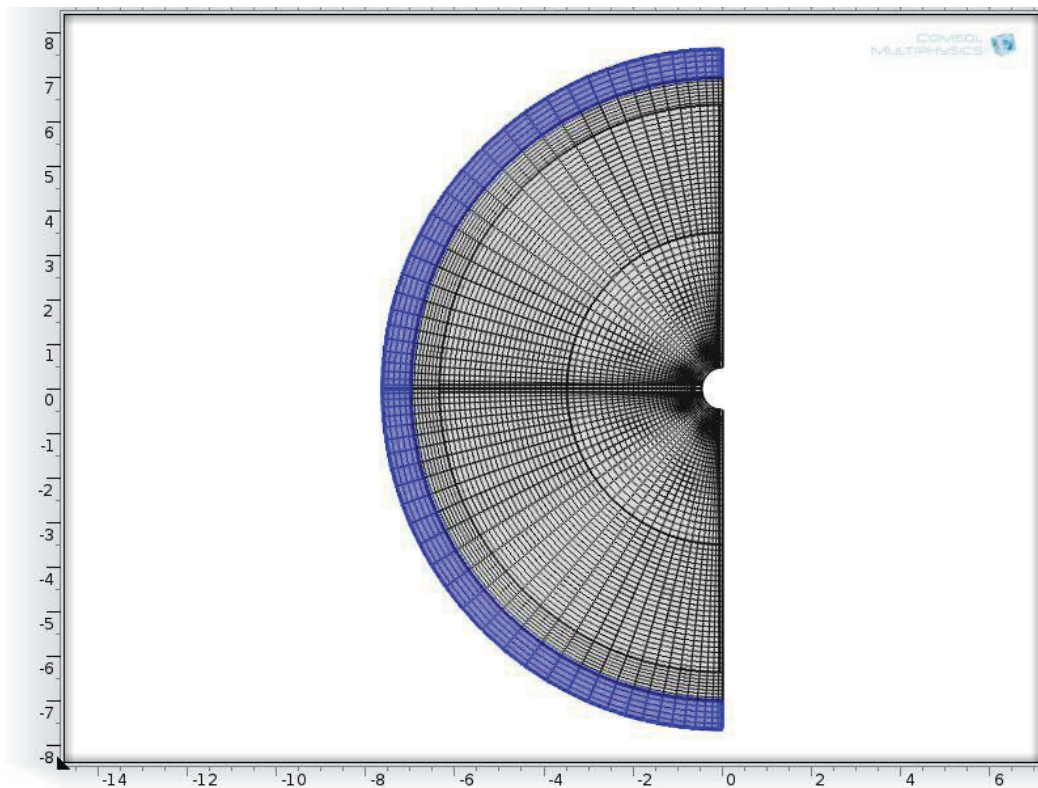


Figure 4.6: Final mapped mesh of numerical model which consists of 4416 elements

4.2. Numerical Results of Pure Conduction Models

The comparison of experimental and numerical results of temperature profiles for four probe thermocouples (T11 to T14) is presented in Figs. 4.6 to 4.9. In COMSOL simulations, two models with different boundary conditions are used: one with constant heat flux and the other one with constant temperature. Heat flux is applied by manually inputting the corresponding heat transfer coefficient which is calculated in section 4.1.2. Constant temperature boundary condition is applied as a comparison in order to determine a better match of the experimental results.

Since there is no natural convection simulated in the model presented in this section, the temperature profiles between higher and lower quadrants will be symmetric. For this reason, T11 and T12 are compared with the same numerical results, as is T13 and T14.

4.2.1. Numerical Results of Melting With Pure Conduction

First, simplified models with pure conduction are simulated: one with a constant HTF inlet temperature of 60°C; the other one with a constant heat flux based on heat transfer coefficient presented in section 4.1.2. Numerical results are compared with experimental data observed from the same testing parameters.

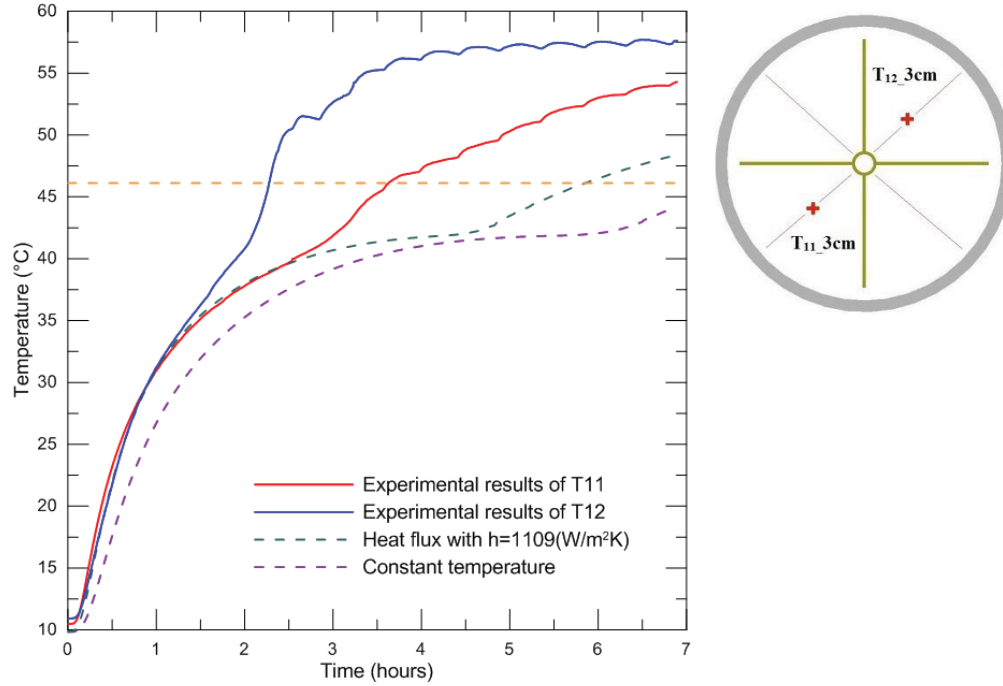


Figure 4.7: The comparison of experimental and numerical temperature profiles during charging for T11 and T12 (HTF inlet temperature of 60°C, HTF flow rate of 1 L/min)

It is observed from Fig. 4.7 and Fig. 4.8 that results of constant heat flux boundary model matches experimental results better than the constant temperature model. For T12, 3cm away from the center in the higher quadrant, the temperature profile of experiment results follows the pattern of heat conduction until $t = 1.1$ hours. This result validates the conclusion in previous section 3.2.1 that the dominant heat transfer mechanism is heat conduction at the initial stage of melting.

Similar results are seen on Fig. 4.7 for T11 which is situated 3cm away from the center in the lower quadrant. However, the initial stage when heat conduction is the dominant heat transfer mode is longer for T11 than T12. The reason is the onset of natural convection in the higher quadrants happens earlier than lower quadrants. Furthermore, this observation also confirms precious experimental results that higher quadrants have higher temperature because of more intense natural convection.

The complete melting time for the pure conduction model with constant heat flux is 11.25 hours which is significantly longer than the time observed in the experimental test. Consequently,

neglecting natural convection in numerical studies of phase change clearly does not account for the right heat transfer physics. It is still a valuable way to highlight departures in the experimental results from a pure conduction situation.

For thermocouple T13 and T14, which are situated farther away from the center than T11 and T12, numerical results with pure conduction are compared with experimental results in Fig 4.8.

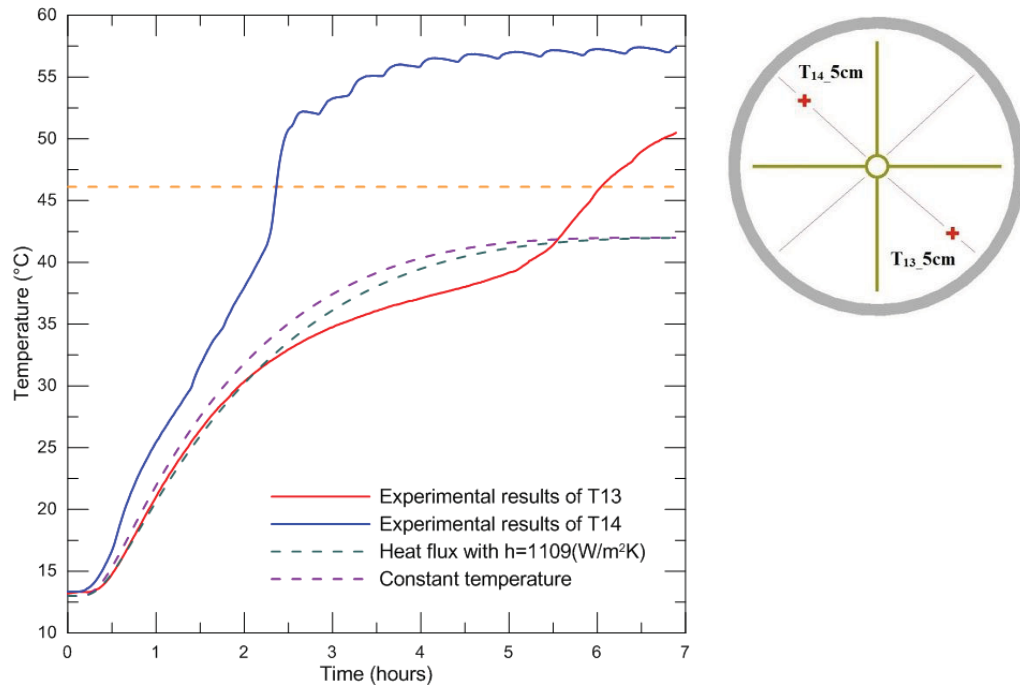


Figure 4.8: The comparison of experimental and numerical temperature profiles during charging for T13 and T14 (HTF inlet temperature of 60°C, HTF flow rate of 1 L/min)

It is noted that for T14, the temperature profile of experimental results is higher than both numerical simulations from the very beginning. This result proves the assumption that natural convection is the dominant heat transfer mode during charging. It can be also noticed that natural convection greatly reduces the time required for T14 to reach the melting point.

However, for T13 which is situated at the same distance away from the center but in the lower quadrant, fairly different results are obtained (Fig. 4.8). As expected, the initial stage of charging follows the heat conduction pattern closely. This initial stage lasts for two hours. In the next stage, the temperature recorded experimentally is lower than the one obtained numerically for

approximately three hours. The reason is that the heat transferred to T13 is suppressed by the upward buoyancy flow caused by natural convection. Hot fluid with higher temperature is displaced upwards which leaves relatively cooler PCM at the bottom. Ultimately, the PCM at the T13 probe location will melt, and the recorded temperature will increase rapidly as higher temperature liquid PCM move over the probe from natural convection.

4.2.2. Numerical Results of Solidification with Pure Convection

Simulations of discharging process without convection were conducted. Two numerical models with different boundary conditions on the pipe were simulated. One model uses a constant temperature of 9°C on the pipe and the other model uses a heat flux on the inner pipe surface. The HTF flow rate is 8 L/min and the convection coefficient can be found in Table 4.2.

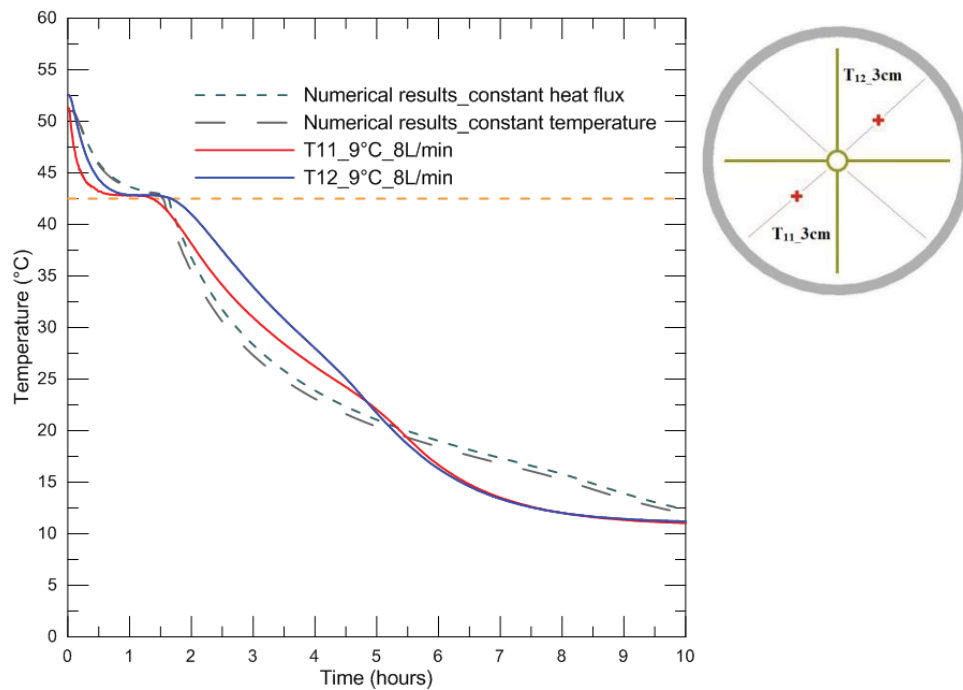


Figure 4.9: The comparison of experimental and numerical temperature profiles during discharging for T11 and T12 (HTF inlet temperature of 9°C, HTF flow rate of 8 L/min)

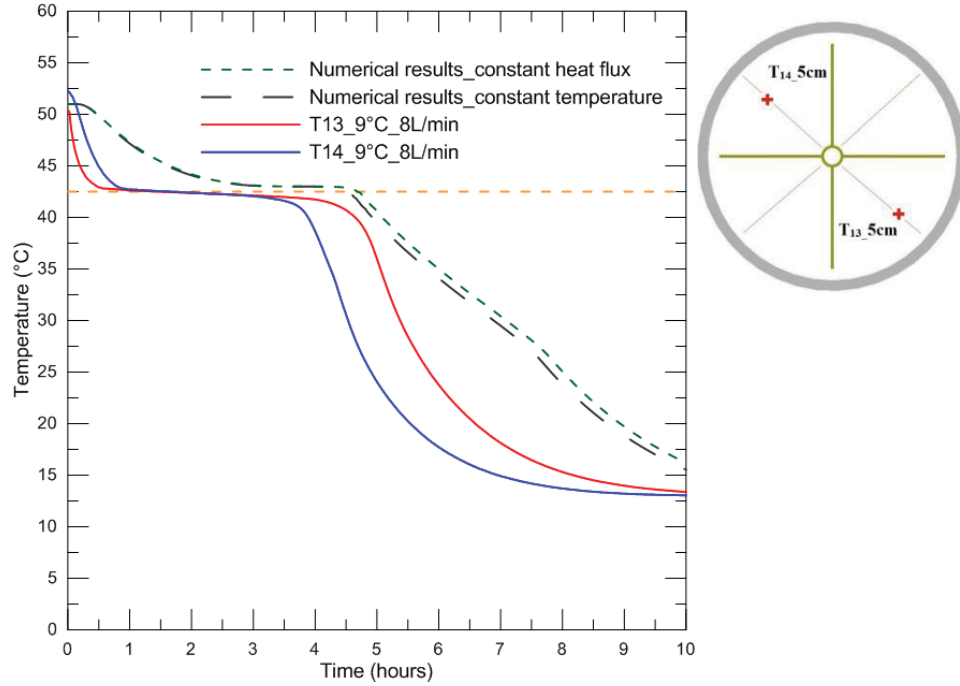


Figure 4.10: The comparison of experimental and numerical temperature profiles during discharging for T13 and T14 (HTF inlet temperature of 9°C, HTF flow rate of 8 L/min)

It is observed from Figs. 4.9 and 4.10 that the result of the convective heat flux boundary model are similar to the constant temperature model. Compared with experimental results, numerical simulations reached the solidification temperature later. The reason accounting for this is twofold: i) the probe thermocouples are acting as nucleating sites which speeds up solidification in experimental tests, and ii) there is a possible limitation of the numerical model itself which will be discussed in section 4.3.

4.3. Numerical Results with Convection

In this section, natural convection is taken into account. As discussed in section 4.1, there are three heat transfer mechanisms that are considered: conduction, natural convection and phase change heat transfer. Moreover, based on results from section 4.2, the constant heat flux boundary condition was applied on the pipe because of better match between numerical results and experimental results.

4.3.1. Numerical Results of Charging with Convection

The test with a HTF inlet temperature of 60°C and HTF flow rate of 1 L/min was simulated for nine hours using COMSOL. The computational time required to solve this model is approximately seven days. The temperature plots are shown in Fig. 4.11 (the black contour line represents the solid-liquid interface) and comparison between numerical and experimental results is shown in Fig. 4.12.

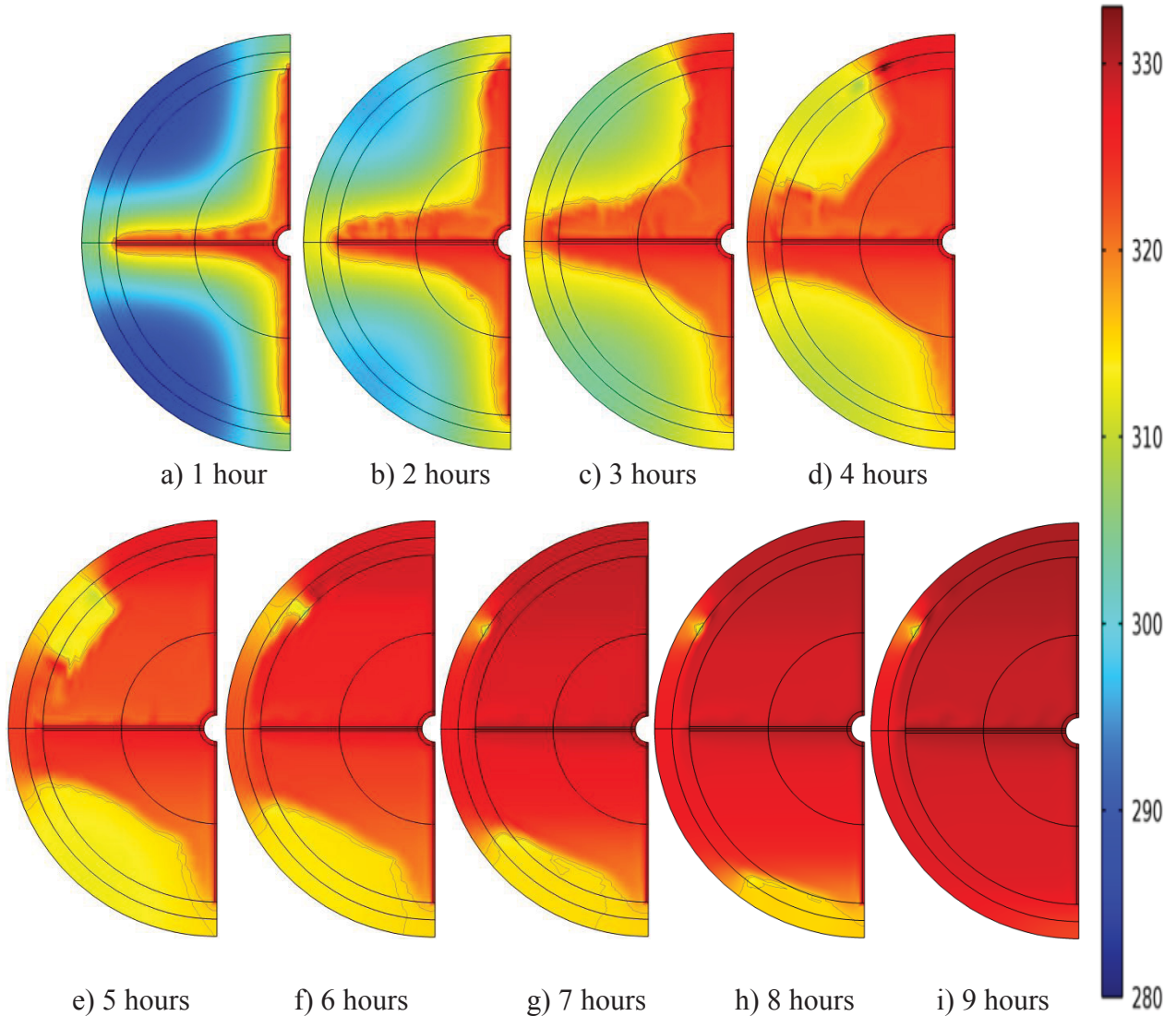


Figure 4.11: The numerical temperature plots during charging for the straight fin configuration accounting for convection (HTF inlet temperature of 60°C, HTF flow rate of 1 L/min)

It is noted that natural convection is more intense in the upper quadrants. Similar result is observed in the experimental tests. During the first hour of charging, the melting interface is

symmetrical between higher and lower quadrants. This indicates that the dominant heat transfer mode during the first hour of charging is conduction. After the first hour, there is a larger melting fraction in higher quadrants which indicates the onset of natural convection.

The very bottom part of lauric acid at the lower quadrants took approximately two hours (from $t=7$ hours to $t=9$ hours) to melt. Optimised design of heat transfer enhancement in the bottom part of the container will result in better heat transfer performance, for example, extending heat transfer surface at the bottom of PCM containers such as adding extra fins to the bottom of the container.

The complete melting time (HTF inlet temperature 60°C , flow rate 1 L/min) for the experimental test is 7.8 hours. However, it took nine hours for the numerical simulation to achieve complete melting. There are two reasons leading to this difference. The first reason is that this model cannot accurately simulate the impact of adding metal probe thermocouple into the PCM. Second, the exact boundary condition on the pipe inner surface is difficult to exactly model, which can lead to underestimation of it; there is not sufficient information to calculate an exact value.

In Fig. 4.12, experimental temperature profiles and numerical results are compared. It is noted that in lower quadrants, where T11 and T13 are placed, results between experimental tests and numerical model are relatively close. However, in higher quadrants, where T12 and T14 are situated, it appears that the strength of natural convection cannot be exactly simulated. This also leads to an underestimation of the PCM temperatures as a function of time.

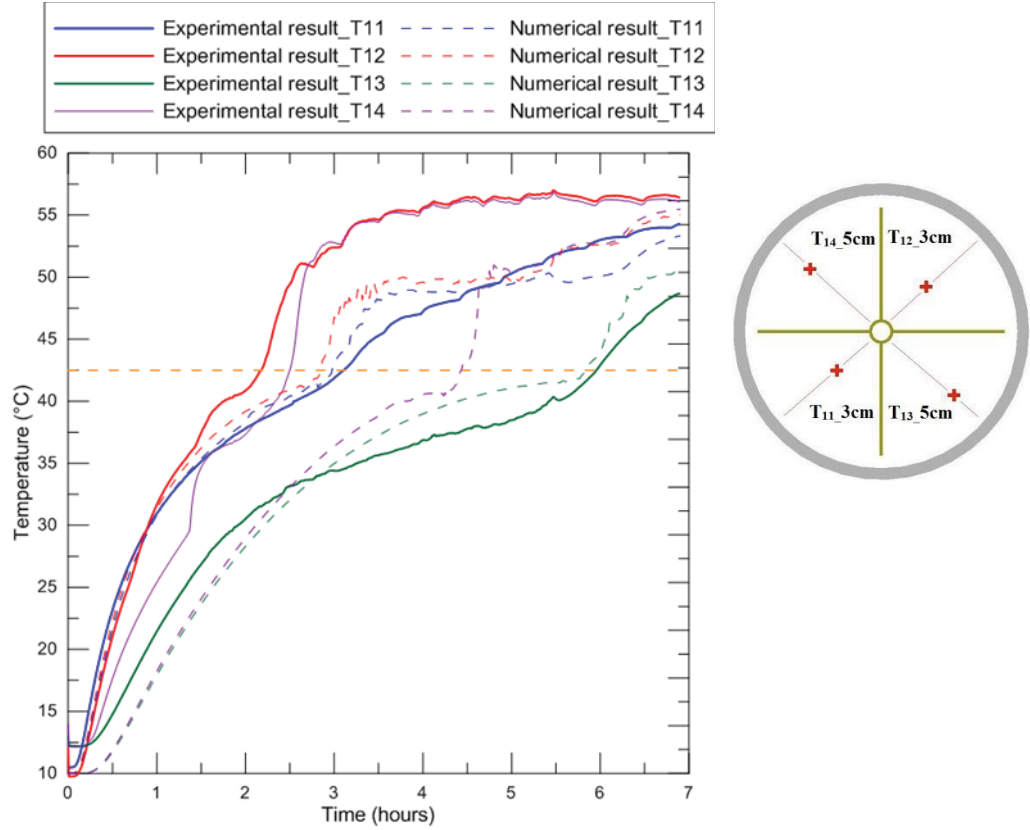


Figure 4.12: The comparison of temperature profiles between experimental and numerical results during charging (HTF inlet temperature of 60°C, HTF flow rate of 1 L/min)

4.3.2. Numerical Results of Discharging

One discharging experiment, using a HTF inlet temperature of 9°C and flow rate of 8 L/min, was simulated accounting for both conduction and convection. The computational time required to run this model was approximately four days. The temperature plots during solidification are shown in Fig. 4.13 and a comparison between experimental and numerical temperature profiles is presented in Fig. 4.14.

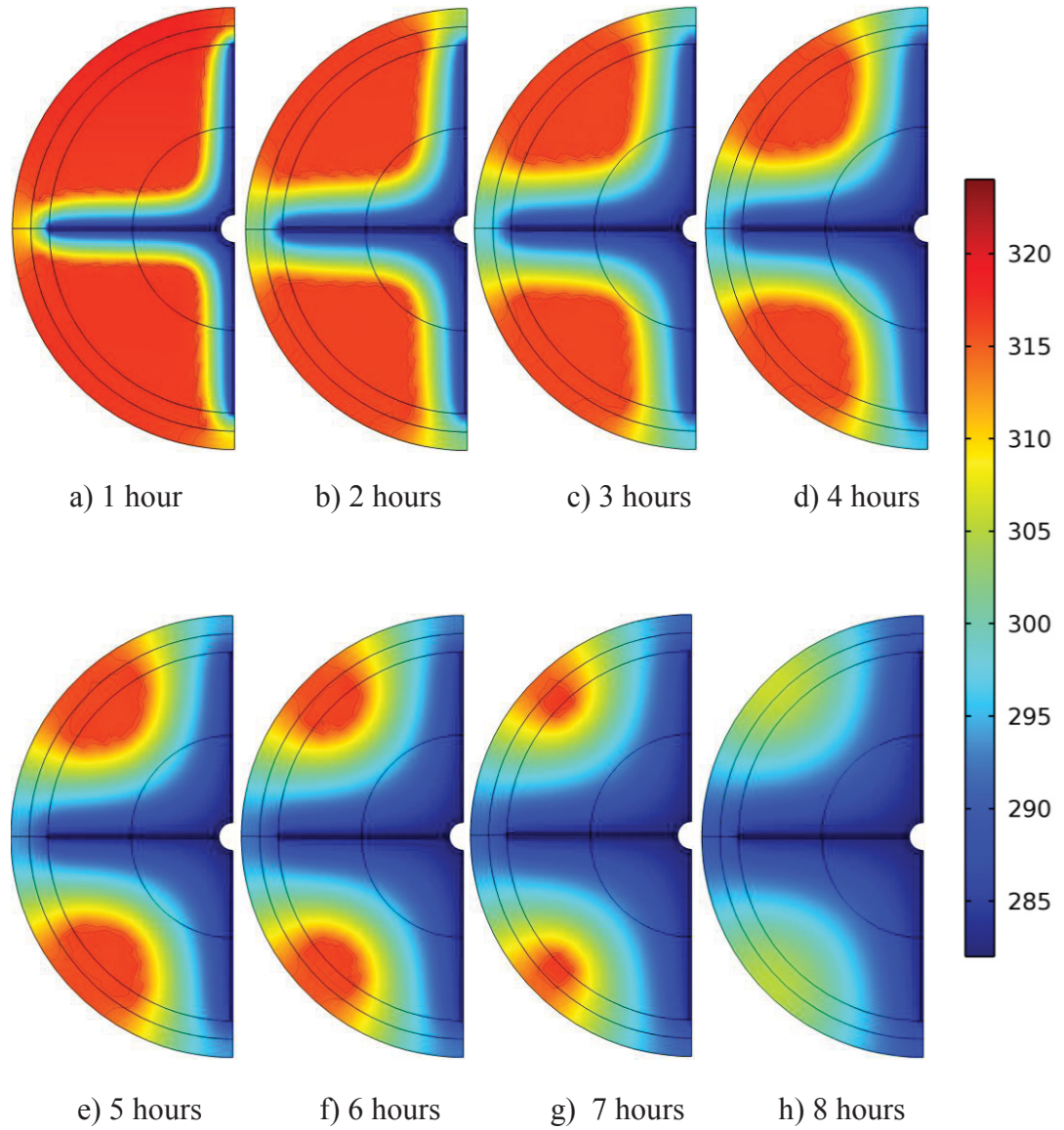


Figure 4.13: The numerical temperature plots during solidification for the straight fin configuration accounting for convection (HTF inlet temperature of 9°C, HTF flow rate of 8 L/min)

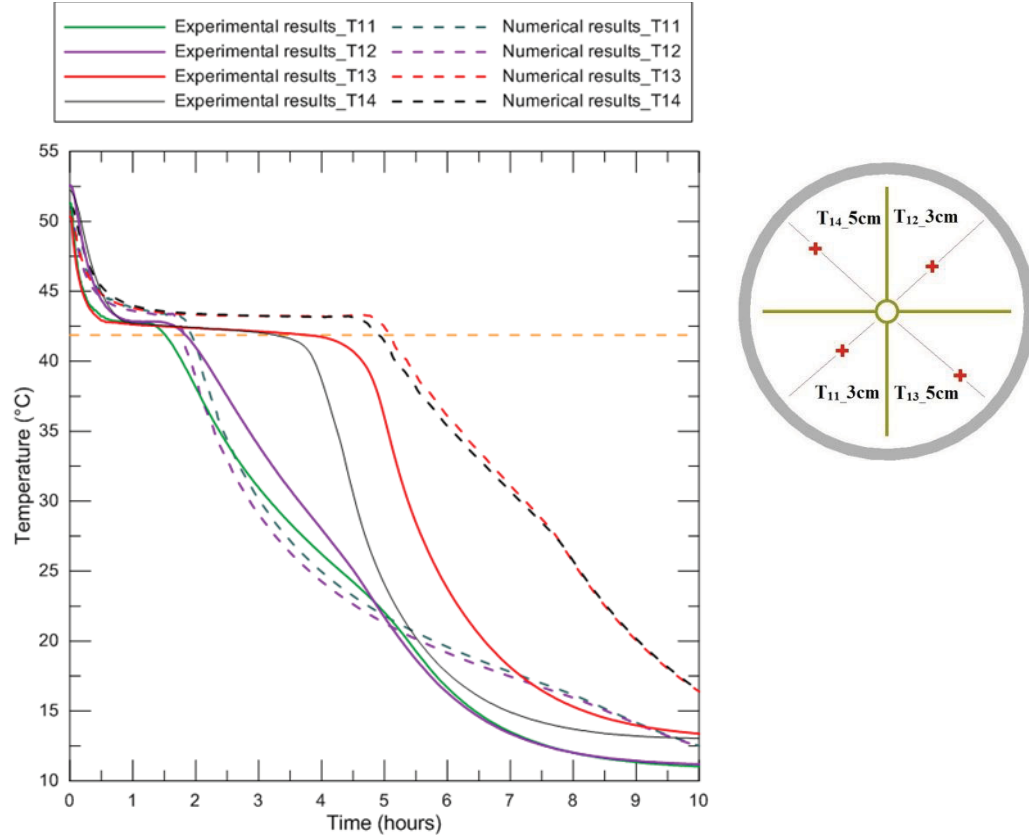


Figure 4.14: The comparison of temperature profiles between experimental and numerical results during discharging (HTF inlet temperature of 9°C, HTF flow rate of 8 L/min)

It is found in Fig. 4.13 that complete discharging time is eight hours which is very close to the solidification time in the experimental test. Besides, as seen from the temperature plots, most of the lauric acid is solidified after the first five hours, with only a small amount of PCM solidifying slowly during the last three hours. The reason is at the beginning of discharging, the temperature difference between liquid lauric acid and the HTF is high. As discharging progresses, this temperature difference becomes smaller which reduces the heat transfer rate. In addition, there is also an impact of the extra solid PCM insulation which increases the thermal resistance on the PCM side. Therefore, in order to recover stored energy faster, the LHESS design should take advantages of the first five hours to achieve better performance.

No significant difference is observed between higher and lower quadrants for the numerical simulation, which indicates the dominant heat transfer mode is heat conduction throughout the whole process. Similar results are found in section 3.4.2 for the experimental test.

It is found from Fig. 4.14 that there is mismatch between experimental results and numerical results. One reason for this discrepancy is the fact that probe thermocouples added into the PCM become nucleation sites, therefore changing the physical discharging process. However, both experimental and numerical temperatures reach their lowest and final values almost at the same time. This indicates the numerical simulation for discharging is still promising.

4.4. Conclusion

In this chapter, the results of two numerical simulations with pure conduction were presented. In one model, a constant temperature boundary was applied to the pipe. In the other model, a convective heat flux was applied. Results show that the numerical model with convective heat flux fits the experimental results better. It is noted that at the initial stage of melting, conduction is the dominating heat transfer process. As more lauric acid is melted, the experimental temperature profiles start to diverge from numerical results, indicating the presence of natural convection.

In addition, simulation of numerical models with both conduction and convection were undertaken using a convective heat flux boundary condition on the pipe. In higher quadrants during charging, it appears that the strength of natural convection cannot be exactly simulated. This also leads to an underestimation of the PCM temperatures as a function of time. A relatively close match is found in the lower quadrants where natural convection is less intense compared with higher quadrants. However, numerical model of discharging matches experimental test better and is recommended as an effective numerical method to characterize LHESS in this case.

CHAPTER 5 : EXPERIMENTAL AND NUMERICAL RESULTS FOR ANGLED FIN CONFIGURATION

Another orientation of fins, angled fins, is studied to compare heat transfer enhancement effectiveness with the straight fin orientation. This new orientation is arranged by rotating the straight fins (Chapter 3) by 45° . The side view of the angled fin configuration is shown in Fig. 5.1.

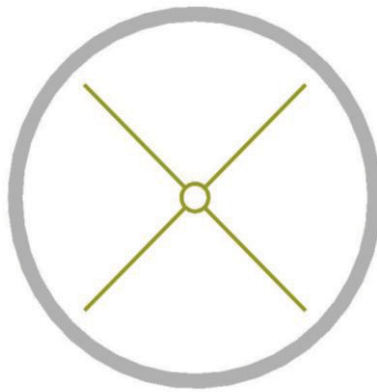


Figure 5.1: The angled fins orientation

5.1. Detailed Temperature Profiles

5.1.1. Charging

Six tests were performed with various HTF inlet temperatures and HTF flow rates and results are compared with straight fins. Figures 5.2 to 5.4 presents results at a HTF inlet temperature of 50°C while Figs. 5.5 to 5.7 show results with a higher HTF inlet temperature of 60°C .

As expected, the initial stage of melting is conduction-dominant. This conclusion can be validated by the pattern of melting profiles at the initial stage. Another validation comes from the comparison with pure conduction numerical models presented in section 5.3.

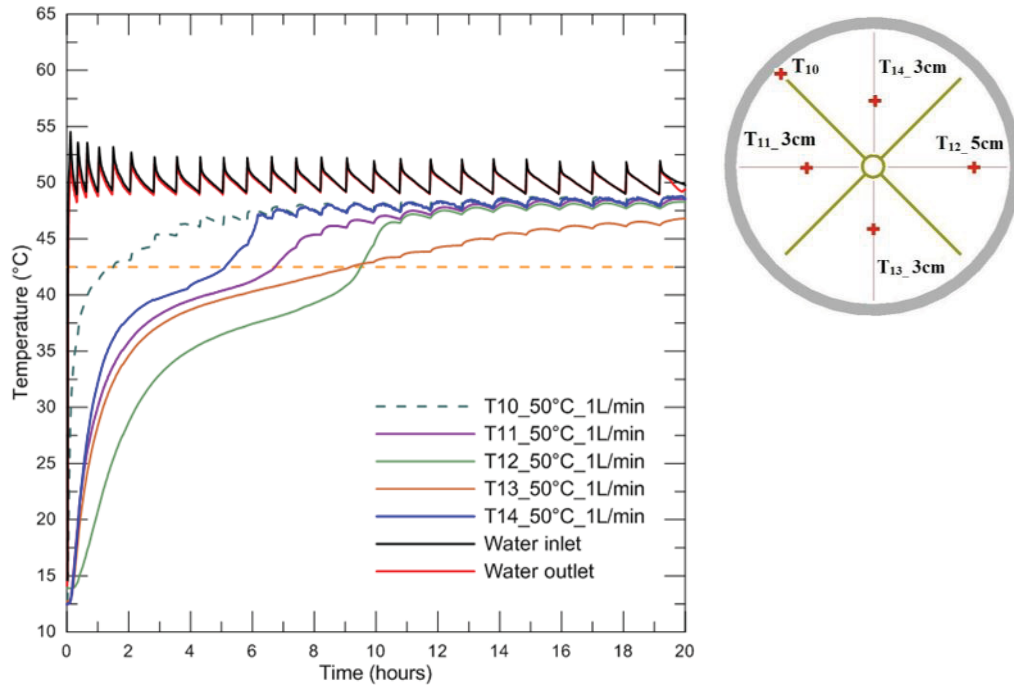


Figure 5.2: Temperature profiles of T10 to T14 at a HTF inlet temperature of 50°C and HTF flow rate of 1 L/min

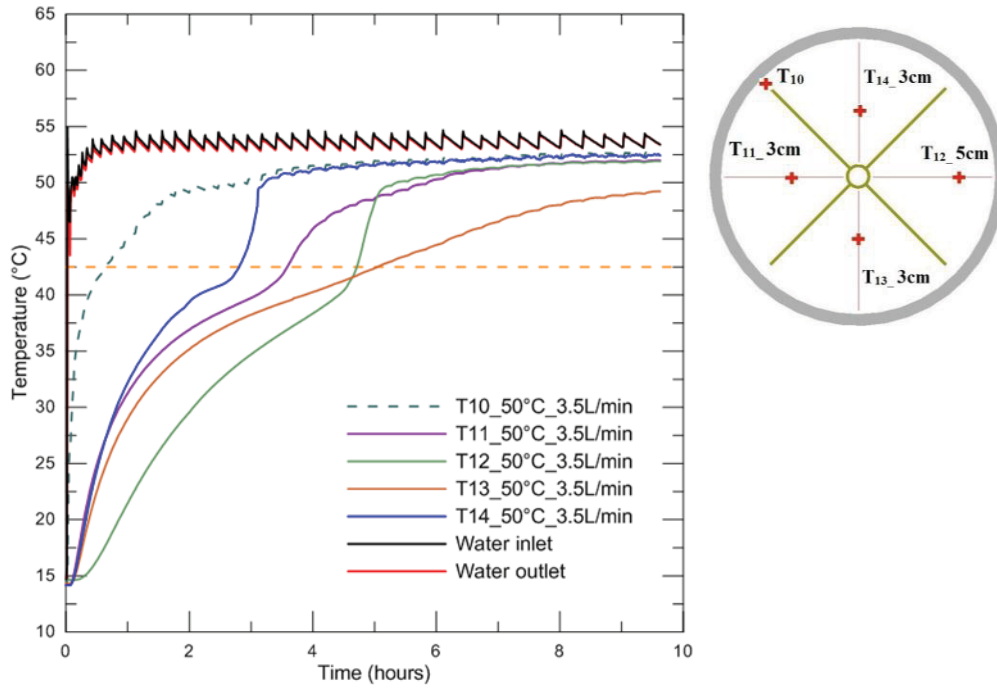


Figure 5.3: Temperature profiles of T10 to T14 at a HTF inlet temperature of 50°C and HTF flow rate of 1 L/min

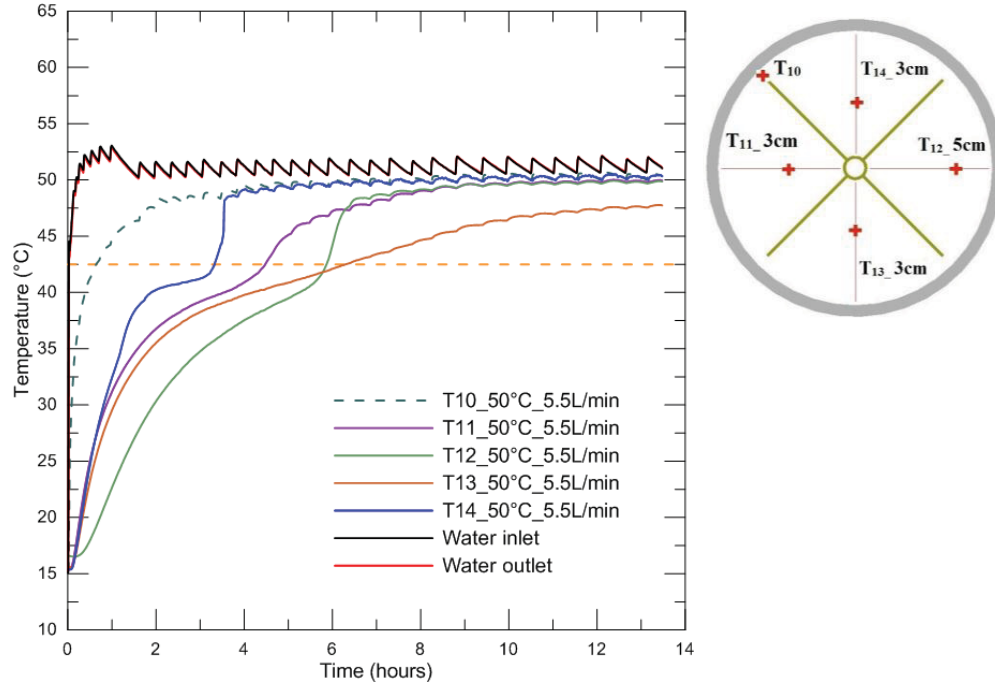


Figure 5.4: Temperature profiles of T10 to T14 at a HTF inlet temperature of 50°C and HTF flow rate of 1 L/min

It is found that T10 is the always the first thermocouple to reach the melting point because of its closeness to the fin. In order to compare the natural convection intensity in each quadrant, T11, T13 and T14 are placed at the same distance away from the center (3cm). T14 is placed in the right quadrant, 5cm away from the center (shown in the indicator on the top right corner of each figure). The most intense natural convection is found at the upper quadrant which is reflected by T14 because natural convection is enabled by two fins in this quadrant. While in the side quadrant, where T11 is placed, only one fin enables natural convection. Therefore, T11 has a lower temperature than T14.

Compared with T11, T13 shows lower temperatures and takes longer to reach the melting point. This indicates heat transfer is less intense in the lower quadrant. The reason is in the lower quadrant, there is no fin promoting natural convection and high temperature liquid PCM rises up closer to the pipe, impeding heat transfer to the bottom region. In fact, T12 is situated 2cm farther away from the center than T13 but still melts faster. This comparison provides a more clear understanding of how a heat transfer rate differs between each quadrant.

From Figs. 5.2 to 5.7, it is noted that increasing the HTF inlet temperature from 50°C to 60°C significantly reduces the complete melting time which is also observed with the straight fin experimental tests.

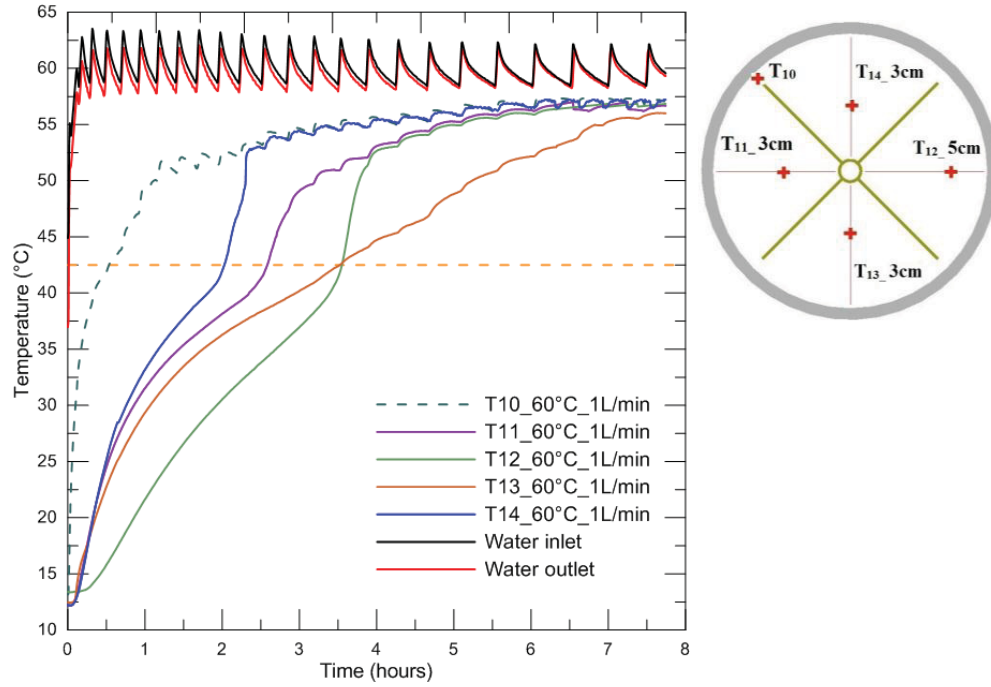


Figure 5.5: Temperature profiles of T10 to T14 at a HTF inlet temperature of 50°C and HTF flow rate of 1 L/min

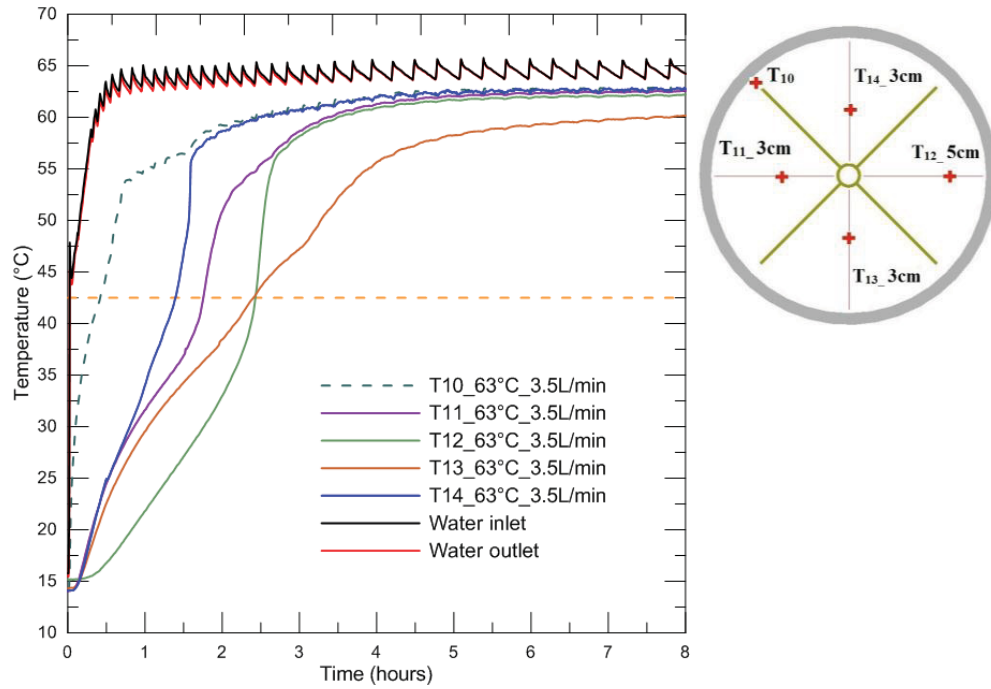


Figure 5.6: Temperature profiles of T10 to T14 at a HTF inlet temperature of 50°C and HTF flow rate of 1 L/min

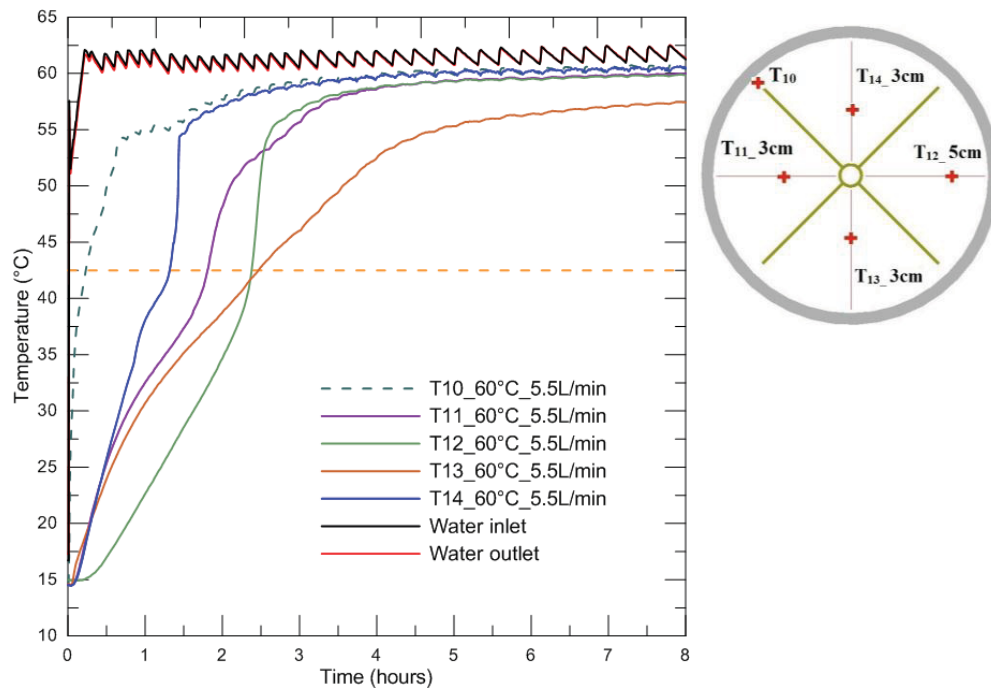


Figure 5.7: Temperature profiles of T10 to T14 at a HTF inlet temperature of 50°C and HTF flow rate of 1 L/min

5.1.2. Discharging

During discharging, two tests with different HTF flow rates are conducted and results are presented in Fig. 5.8. There is no significant difference between melting profiles of T11, T13 and T14, which indicates conduction is the dominant heat transfer mode.

It is observed that the impact of discharging HTF flow rates on temperature profiles is minimal. Similar observations are achieved for straight fins both experimentally and numerically.

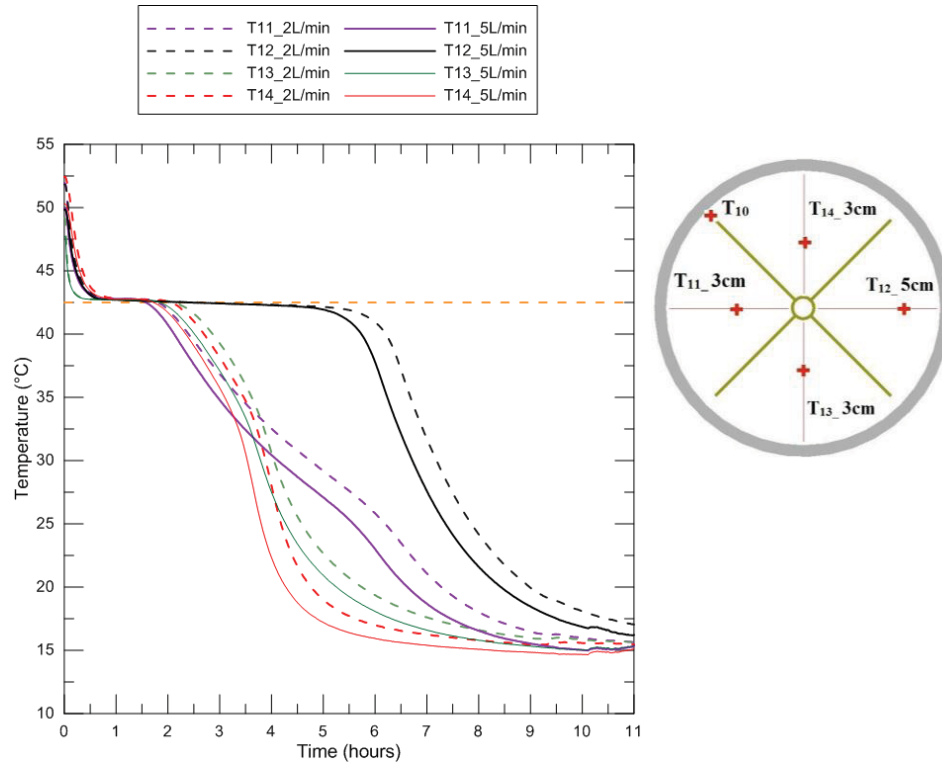


Figure 5.8: HTF flow rates effect on temperature profiles of T11-T14

5.2. Comparison with Straight Fins

The complete charging time for four tests are compared: two with straight fins and the other two with angled fins. In all these tests, the initial temperature is 10°C, the HTF flow rate is 1 L/min, and HTF inlet temperatures are 50 °C and 60 °C. Results are presented in Fig. 5.9.

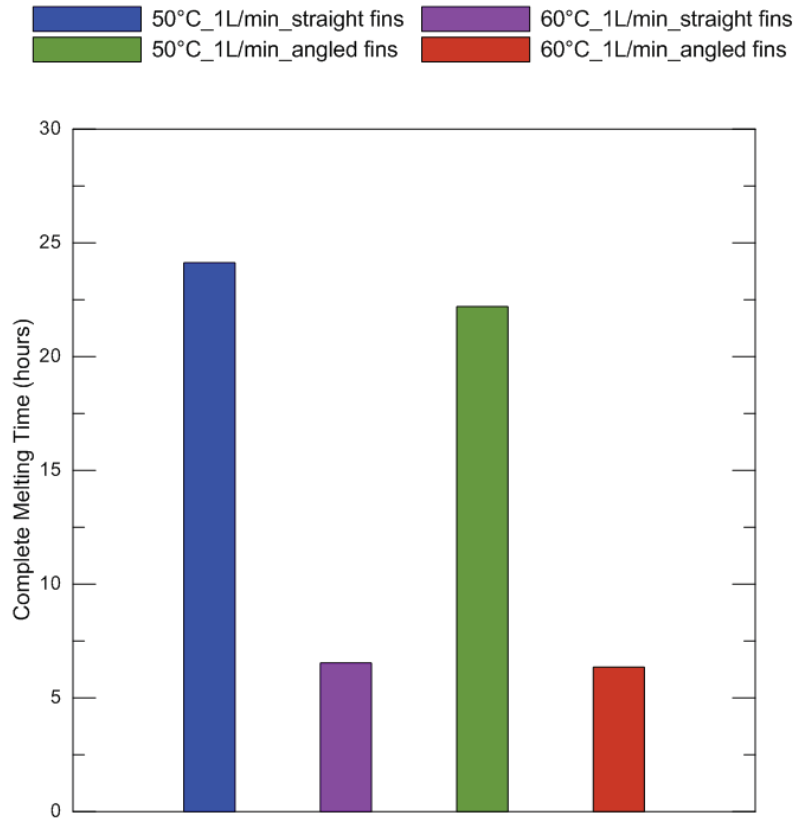


Figure 5.9: Melting time comparison between straight fins and angled fins

It is noted from Fig. 5.9 that for a relatively low HTF inlet temperature (50°C), angled fins reduces the complete melting time slightly compared with straight fins. The reason is the bottom part of lauric acid took a long time to melt with straight fins. Energy is displaced upwards by natural convection which leaves insufficient heat transfer to the very bottom part of PCM. For the angled fins, effective heat transfer area is increased for the very bottom portion of lauric acid (with two fins). More heat transfer area enhances heat transferred to the bottom part of PCM.

However, for a relatively high HTF inlet temperature of 60°C, there is no difference in the melting time, and the heat transfer enhancement effect between straight fins and angled fins becomes similar.

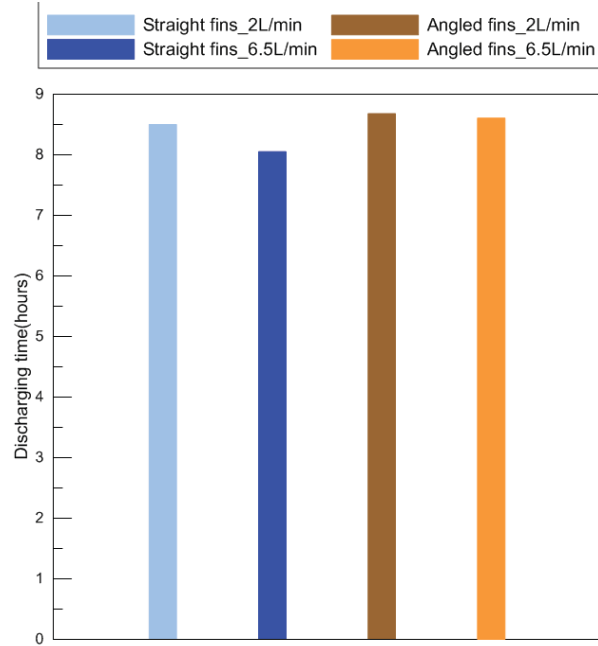


Figure 5.10: Discharging time comparison between straight fins and angled fins

Total discharging time for straight fins and angled fins is compared in Fig. 5.10. Because the discharging in all tests is conduction-dominant, it is reasonable to conclude that there is no significant difference of discharging time between these two fin configurations.

5.3. Numerical Results with Pure Conduction

In this section, numerical results obtained with a simplified model using only pure conduction are presented. In the COMSOL, two models with different boundary conditions are again used: one with convective heat flux and the other one with constant temperature. Heat flux is applied by manually inputting the heat transfer coefficient which can be found in Table 4.2. Constant temperature boundary condition is applied as a comparison in order to determine a better match to the experimental results. A similar procedure was used to model this configuration (straight fins in section 4.2).

Since there is no natural convection simulated in the model presented in this section, the temperature profiles between higher and lower quadrants will be symmetric. For this reason, T11, T12 and T13 are compared with the same numerical results. Simulations are run for charging and discharging respectively. Results are shown in Fig. 5.11 and Fig. 5.12.

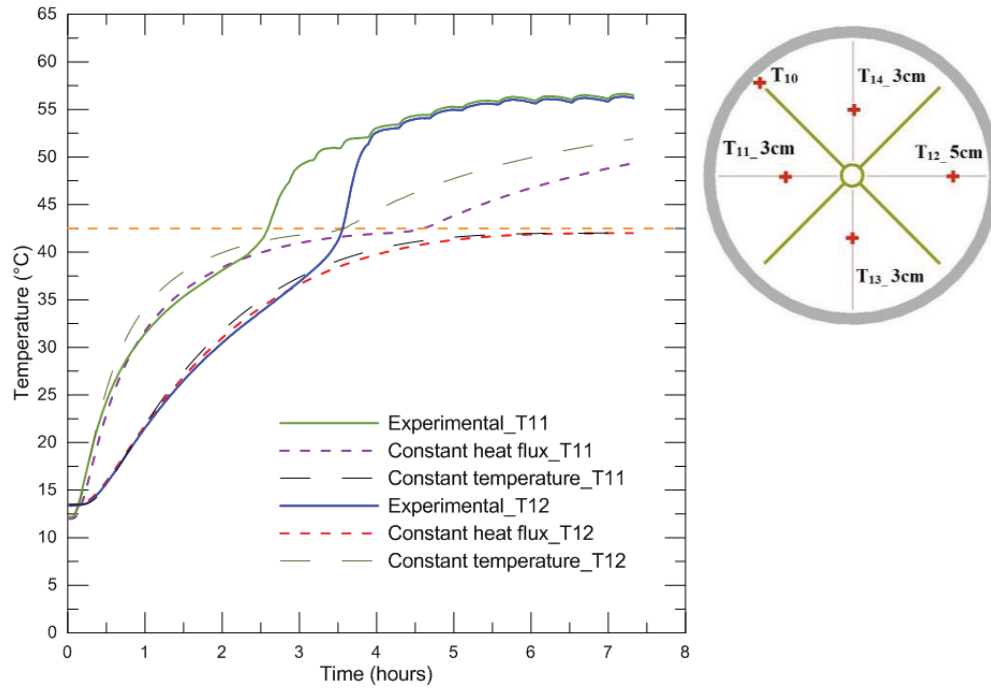


Figure 5.11: The comparison of experimental and numerical temperature profiles of T11 and T12 (charging)

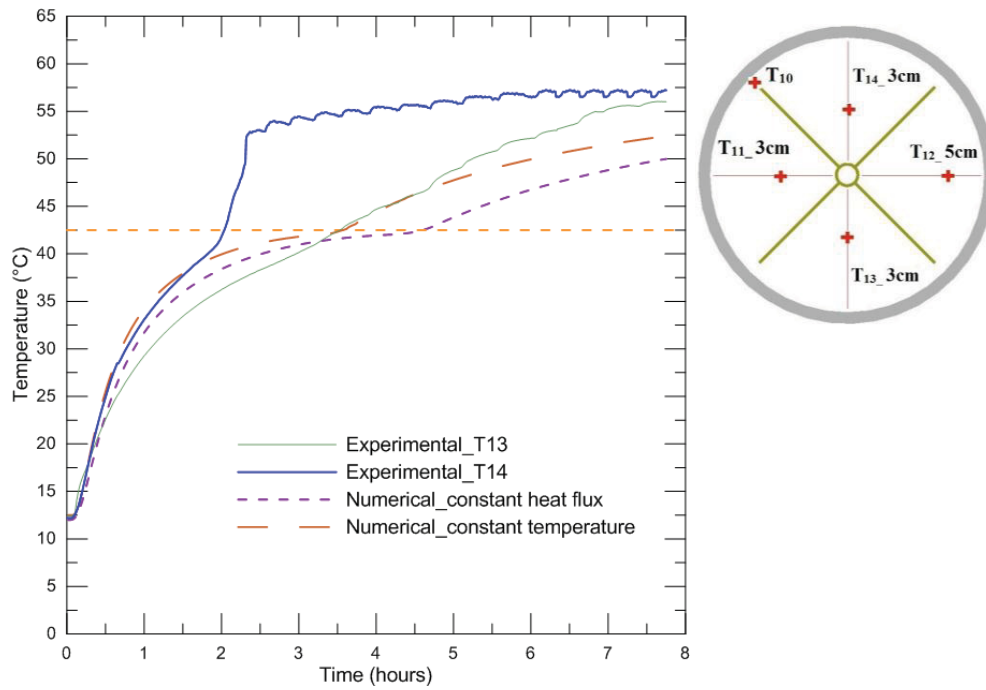


Figure 5.12: The comparison of experimental and numerical temperature profiles of T13 and T14 (charging)

It is noted that at the initial stage, temperature profiles of T11 and T12 follow conduction pattern closely. Then the temperature curve diverges from numerical results as natural convection starts to play a more important role and enhances heat transfer at these two locations.

T14 has a higher temperature than the numerical result after only $t = 0.7$ hour, which indicates the early onset of natural convection in the upper quadrant. However, at the same distance away from the pipe, T13 has a lower temperature than the numerical one between 0.5 hour and 3.3 hours. That can be explained by the impact of natural convection in this lower quadrant. Heat is displaced upwards which results in a lower temperature at the bottom in the experimental test compared with the pure conduction model. This validates the assumption that natural convection exists and is the dominant heat transfer mode. Moreover, natural convection is more intense in the higher quadrant which is also observed in the straight fins tests.

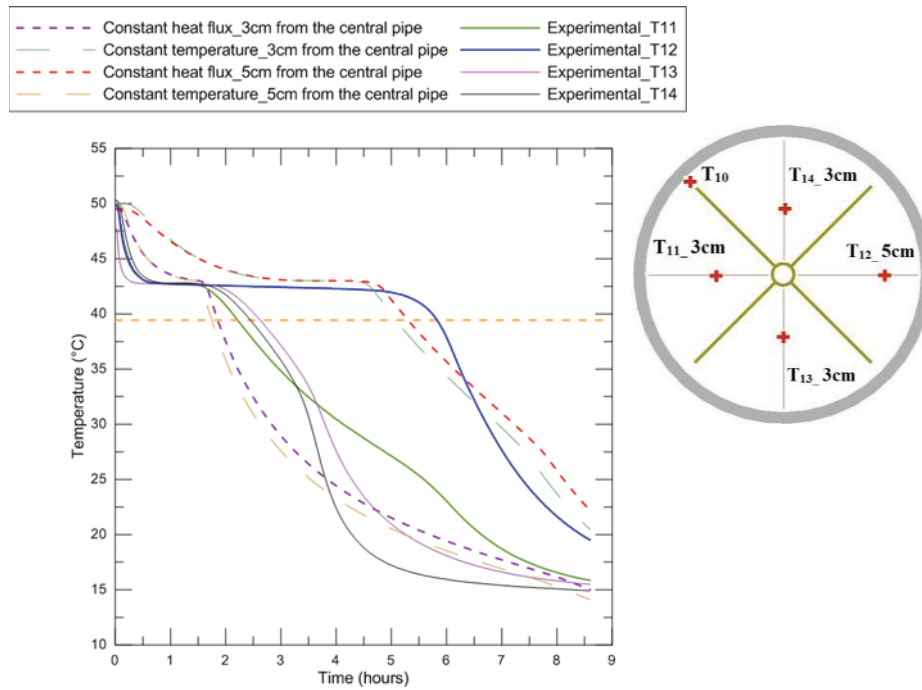


Figure 5.13: The comparison of experimental and numerical temperature profile of T11 to T14 (discharging)

As seen in Fig. 5.13, the temperature profiles of experimental test and numerical model show some differences during discharging. However, they reach the final temperature almost at the same time. In other words, the discharging time is very close for experimental and numerical

results. As expected, discharging of angled fins LHESS is conduction-dominant as it was for the straight fins LHESS.

5.4. Conclusion

In this chapter, experimental and numerical results of angled fins were analyzed and the heat transfer enhancement effectiveness between straight fins and angled fins was compared. It was found that the upper quadrant melts faster than other quadrants due to two fins enabling natural convection. Discharging process is conduction-dominant which was also observed with straight fins.

Numerical simulation validates the conclusion that at the initial stage of melting, conduction is the dominant heat transfer mode. Afterwards, natural convection plays a major role.

It is noted from that for a relatively low HTF inlet temperature (50°C), angled fins reduces the complete melting time slightly compared with straight fins. However, for a relatively high HTF inlet temperature of 60°C , there is no difference in the melting time for these two fins. During discharging, the solidification time is almost the same for these two fins since conduction is the dominant heat transfer mechanism.

CHAPTER 6 : CONCLUSION AND RECOMMENDATIONS

The phase change behaviour of a horizontal cylindrical LHESS was studied experimentally and numerically. Because of the low thermal conductivity of the PCM, the use of a heat transfer enhancement technique was necessary. In this study, longitudinal copper fins in two orientations were added into the PCM: straight fins and angled fins. And the heat transfer enhancement effectiveness was compared between these two orientations. The PCM used in this study was lauric acid, which is a suitable PCM with little or no supercooling, has chemical stability, is non-corrosive and has reasonable cost.

LHESS with straight fins were studied extensively. In the experimental tests, two experimental parameters were tested: the HTF inlet temperature and HTF flow rates. Various tests were conducted with different parameters to study their impact. Moreover, emphasis was put on understanding the phase change mechanism during charging and discharging in this LHESS which provided valuable information for future industrial design.

LHESS with angled fins were explored briefly for a purpose of comparing heat transfer enhancement effectiveness. Several tests with different HTF inlet temperatures and HTF flow rates were performed.

Numerical models were created and simulations were run with COMSOL Multiphysics. Results were used to provide a clearer understanding of the physical process taking place in the experiments.

6.1. Conclusion

In the LHESS with straight fins, detailed temperature profiles in four quadrants of the PCM container were analysed. It was found that at the same distance away from the central pipe, higher quadrants and lower quadrants have different temperature profiles. In higher quadrants,

faster melting and higher temperature were achieved. The reason was natural convection existed and heat was displaced upwards which enhanced the heat transfer rate in higher quadrants.

It was found that heat conduction was the dominant heat transfer mode at the initial stage of charging which can be validated from the nearly linear temperature profile at the beginning of the charging process. This assumption was also validated numerically by simulating a model with pure conduction. As charging progresses, more liquid PCM was formed around the heat transfer surfaces. Natural convection started to play a more important role. This can be observed by comparing temperature profiles in the higher and lower quadrants.

A higher HTF inlet temperature will lead to a higher temperature difference between the PCM and the HTF (water); resulting in more heat transferred to the LHES per unit time. From another point of view, the temperature difference between the PCM and HTF is acting as a driving force for natural convection. The higher this driving force was, the faster lauric acid melted.

It was noted that increasing the HTF flow rate leads to a faster melting rate. The reason was that higher forced convection coefficient was achieved on the HTF side by increasing the HTF flow rate. Although the largest thermal resistance existed in the PCM side, the thermal resistance on the HTF side was reduced. The PCM close to heat transfer surfaces melted faster which resulted in an earlier onset of natural convection.

During discharging, it was noted that conduction was the primary heat transfer mode. Moreover, increasing the HTF flow rate from 1.5 L/min to 12 L/min did not significantly reduce the complete discharging time. In other words, the impact of HTF flow rate on discharging was minimal. The reason was that solid PCM formed on the heat transfer surfaces which increased the thermal resistance on the PCM side and also limited the impact of natural convection during discharging.

For numerical simulations with both conduction and convection heat transfer, it appeared that the strength of natural convection cannot be exactly simulated especially in higher quadrants. This

also led to an underestimation of the PCM temperatures as a function of time. For discharging, the numerical model can predict reasonable temperature plots.

In the other LHESS with angled fins, similar results for the phase change behavior of lauric acid were observed. Besides, it was observed that for a relatively low HTF inlet temperature (50°C), angled fins reduced the complete melting time slightly compared with straight fins. However, for a relatively high HTF inlet temperature of 60°C, there was no difference in the heat transfer enhancement effect between straight fins and angled fins. For discharging, there was no difference in the solidification time between these two fin configurations since discharging was conduction-dominant.

6.2. Recommendations

A summary of recommendations for the present study is given below.

1. In this work, charging time is between 7 and 24 hours which is not practical for industry design. Future work should explore the possibility of reducing charging time. For instance, use multi-pipes with fins in the LHESS which would increase the residence time of the HTF inside the PCM container.
2. To stabilize the HTF inlet temperature, a larger constant water bath should be used. A more precise electric heater will also help to eliminate the fluctuations in the HTF inlet temperature.
3. To get more accurate melting plots inside the PCM, it is recommended that inserting more probe thermocouples inside the PCM at various locations along the pipe axis direction.
4. Future work can also extend the study of the impact of HTF flow rates on discharging. Instead of using municipal cold water as cold HTF, a cold water bath should be used with a precisely temperature-controlled cooler.
5. For future work, accurately modeling natural convection numerically using COMSOL Multiphysics (or other software) should be implemented to get a more accurate numerical model that has a better agreement with experimental results.

REFERENCE

ABHAT A. (1983), “Low temperature latent heat thermal energy storage: heat storage materials”, *Solar Energy*, Vol. 30, pp.313-332.

AGYENIM F., HEWITT N., EAMES P. and SMYTH M. (2010) “A review of materials, heat transfer and phase change problem formulation for latent thermal energy storage systems (LTESS)”, *Renewable and Sustainable Energy Reviews*, Vol.14, pp.615-628.

AGYENIM F., EAMES P. and SMYTH M. (2009) “A comparison of heat transfer enhancement in a medium temperature thermal energy storage heat exchanger using fins”, *Solar Energy*, Vol. 83, pp.1509-1520.

AGYENIM F., EAMES P. and SMYTH M. (2010) “Heat transfer enhancement in medium temperature thermal energy storage system using a multi-tube heat transfer array”, *Renewable Energy*, Vol. 35, Issue 1, pp. 198-207.

AKGUN M., AYDIN O. and KAYGUSUZ K. (2008) “Thermal energy storage performance of paraffin in a novel tube-in-shell system”, *Applied Thermal Engineering*, Vol. 28, pp. 405-413.

ALKAN C. and SARI A. (2008) “Fatty acid/poly (methyl methacrylate) (PMMA) blends as form-stable phase change materials for latent heat thermal energy storage”, *Solar Energy*, Vol.82, pp.118-124.

ASSIS E., KATSMAN L., ZISKIND G. and LETAN R. (2007) “Numerical and experimental study of melting in a spherical shell”, *International Journal of Heat and Mass Transfer*, Vol. 50, pp.1790-1804.

ATHIENITIS A.K., LIU C., HAWES D., BANU D. and FELDMAN D. (1997) “Investigation of the thermal performance of a passive solar test-room with wall latent heat storage”, *Building and Environment*, Vol. 32, pp. 405-410.

A11672 – Dodecanoic Acid, Material Safety Data Sheet, Alfa Aesar, 2009, www.alfa.com/en

BADESCU V. (2003) “Model of a thermal energy storage device integrated into a solar assisted heat pump system for space heating”, *Energy Conversion and Management*, Vol. 44, pp.1589-1604.

BABASZEK J., DOMAN R., REBOW M., and EI-SAGIER F. (1999) “Experimental study of solid and liquid phase change in a spiral thermal energy storage unit”, *Applied Thermal Engineering*, Vol. 19, pp. 1253-1277

BAETENS R., Jelle B. and Gustavsen A. (2010) “Phase change materials for building applications: A state-of-the-art review”, *Energy and Buildings*, Vol. 42, pp.1361-1368.

BARAN G. and SARI A.(2003) “Phase change and heat transfer characteristics of a eutectic mixture of palmitic and stearic acids as PCM in a latent heat storage system”, *Energy Conversion and Management*, Vol. 44, pp. 3227-3246.

BATHELT A.G. and VISKANTA R. (1980) "Heat transfer at the solid-liquid interface during melting from a horizontal cylinder", *International Journal of Heat and Mass Transfer*, Vol.23, pp.1493-1503.

BEDECARRATS J.P., LASVIGNOTTES J.C., STRUB F. and DUMAS J.P. (2009) "Study of a phase change energy storage using spherical capsules. Part I: Experimental results", *Energy Conversion and Management*, Vol. 50, pp. 2527-2536.

BENMANSOUR A., HAMDAN M.A. and BENGUEUDDACH A. (2006) "Experimental and numerical investigation of solid particles thermal energy storage unit", *Applied Thermal Engineering*, Vol. 26, pp. 513-518.

CHAN C.W. and TAN F.L. (2006) "Solidification inside a sphere-an experimental study", *International Communications in Heat and Mass Transfer*, Vol. 33, pp. 335-341.

Chemical Properties Handbook, edited by C. L. Yaws, McGraw-Hill, 1999

CHO K. and CHOI S.H. (2000) "Thermal characteristics of paraffin in a spherical capsule during freezing and melting processes", *International Journal of Heat and Mass Transfer*, Vol. 43, pp. 3183-3196.

CAMPBELL T.A. and KOSTER J.N. (1994) "Visualization of liquid-solid interface morphologies in gallium subject to natural convection", *Journal of Crystal Growth*, Vol.140, pp.414-425.

DESGROSSEILLIER L., MURRAY R., SAFATLI A., MARIN G., STEWART J., OSBOURNE N., WHITE M.A., GROULX D. (2011), "Phase Change Material Selection in the Design of a Latent Heat Energy Storage System Coupled with a Domestic Hot Water Solar Thermal System", 2011 ASHRAE Annual Conference, Montreal, Canada.

DINCER I. and ROSEN M.A. (2002) "Thermal energy storage: systems and applications", Jone Wiley and Sons, New York.

DUTIL Y., ROUSSE D.R., SALAH N.B., LASSUE S., and ZALEWSKI L. (2011) "A review on phase-change materials: Mathematical modeling and simulations", *Renewable and Sustainable Energy Reviews*, Vol. 15, pp. 112-130.

EI-DESSOUKY H. and AI-JUWAYHEL F. (1997) "Effectiveness of a thermal energy storage system using phase-change materials", *Energy Conversion and Management*, Vol. 38, pp. 601-617.

EAMES I.W. and ADREF K.T. (2002) "Freezing and melting of water in spherical enclosures of the type used in thermal (ice) storage systems", *Applied Thermal Engineering*, Vol. 22, pp. 733-745.

ESEN M., DURMUS A. and DURMUS A. (1998) "Geometric design of solar-aided latent heat store depending on various parameters and phase change materials", *Solar Energy*, Vol.62,pp. 12-28.

- ESEN M. and AYHAN T. (1996) "Development of a model compatible with solar assisted cylindrical energy storage tank and variation of stored energy with time for different phase change materials", *Energy Conversion and Management*, Vol.37, pp. 1775-1785.
- ETTOUNEY H.M., ALATIQUI I., AI-SAHALI M. and AI-HAJIRIE K. (2006) "Heat transfer enhancement in energy storage in spherical capsules filled with paraffin wax and metal beads", *Energy Conversion and Management*, Vol.47, pp.211-228.
- ETTOUNEY H.M., ALATIQUI I., AI-SAHALI M and AL-ALI S.A. (2004) "Heat transfer enhancement by metal screens and metal spheres in phase change energy storage systems", *Renewable Energy*, Vol. 29, pp. 841-860.
- FANG G.Y., WU S.M. and LIU X. (2010) "Experimental study on cool storage air-conditioning system with spherical capsules packed bed", *Energy and Buildings*, Vol.42, pp.1056-1062.
- FELDMAN D., SHAPIRO M.M., BANU D. and FUKS C.J. (1989) " Fatty acids and their mixtures as phase-change materials for thermal energy storage", *Solar Energy Materials*, Vol. 18, pp. 201-216.
- FELDMAN D., BANU D., HAWES D., and GHANBARI E. (1991) "Obtaining an energy storing building material by direct incorporation of an organic phase change material in gypsum wallboard", *Solar Energy Materials*, Vol. 22, pp. 231-242.
- FELDMAN D., BANU D., and HAWES D. (1995) " Low chain esters of stearic acid as phase change materials for thermal energy storage in buildings", *Solar Energy Materials and Solar Cells*, Vol.36, pp. 311-322.
- FELDMAN D., BANU D., and HAWES D. (1995) "Development and application of organic phase change mixtures in thermal storage gypsum wallboard", *Solar Energy Materials and Solar Cells*, Vol.36, pp. 147-157.
- GOLDSTEIN R. and RAMSEY J. (1979) "Heat transfer to a melting solid with application to thermal energy storage systems", *Studies in Heat Transfer: a Festschrift for E. R. G. Eckert*. Hemisphere Publishing Corp., New York, pp. 199-20.
- GONG Z.X. and MUJUMDAR A.S. (1997) "Finite-element analysis of cyclic heat transfer in a shell-and-tube latent heat energy storage exchanger", *Applied Thermal Engineering*, Vol. 17, pp. 583-591.
- GROULX D. and LACROIX M. (2007) "Study of the effect of convection on close contact melting of high Prandtl number substances", *International Journal of Thermal Sciences*, Vol. 46, pp.213-220.
- GROULX D. and OGOH W. (2010) "Thermal behavior of phase change material during charging inside a finned cylindrical latent heat energy storage system: Effects of the arrangement and number of fins, *Proceedings of the International Heat Transfer Conference*, Washington, DC, USA.

- HAMDAN M. A. and ELWERR F. A. (1996) "Thermal energy storage using a phase change material", *Solar Energy*, Vol. 56, pp. 183-189.
- HASNAIN S. (1998) "Review on sustainable thermal energy storage technologies, part 1: heat storage materials and techniques", *Energy Conversion and Management*, Vol. 39, pp.1127-1138
- HASAN A. (1994) "Phase change material energy storage system employing palmitic acid", *Solar Energy*, Vol. 52, pp.143-154.
- HALAWA E. and SAMAN W. (2010) "Thermal performance analysis of a phase change thermal storage unit for space heating", *Renewable Energy*, In Press.
- HE B. and SETTERWALL F. (2002) "Technical grade paraffin waxes as phase change materials for cool thermal storage and cool storage systems capital cost estimation", *Energy Conversion and Management*, Vol.43, pp.1709-1723.
- HO C.J. and CHU C.H. (1996) "Numerical simulation of heat penetration through a vertical rectangular phase change material/air composite cell", *International Jouney of Heat and Mass Transfer*, Vol. 39, pp. 1785-1795.
- INCROPERA F., DEWITT D., BERGMAN T. and LAVINE A. (2005), "Fundamentals of Heat and Mass Transfer 6th Edition", John Wiley and Sons, New Jersey, pp. 949.
- ISMAIL K.A.R. and HENRIQUEZ J.P. (2000) "Solidification of PCM inside a spherical capsule", *Energy Conversion and Management*, Vol.41, pp. 173-187.
- ISMAIL K.A.R., ALVES C.L.F., and MODESTO M.S. (2001) "Numerical and experimental study on the solidification of PCM around a vertical axially finned isothermal cylinder", *Applied Thermal Engineering*, Vol.21, pp. 53-77.
- ISMAIL K.A.R. and MORAES R.I.R. (2009) "A numerical and experimental investigation of different containers and PCM options for cold storage modular units for domestic applications", *International Journal of Heat and Mass Transfer*, Vol. 52, pp. 4195-4202.
- JONES B.J., SUN D., KRISHNAN S. and GARIMELLA S.V.(2006) "Experimental and numerical study of melting in a cylinder", *International Journal of Heat and Mass Transfer*, Vol.49, pp.2724-2738.
- KALAISELVAM S., VEERAPPAN M., AARON A.A. and INIYAN S. (2008) "Experimental and analytical investigation of solidification and melting characteristics of PCMs inside cylindrical encapsulation", *International Journal of Thermal Sciences*, Vol.47, pp.858-874.
- KOUSKSOU T., JAMIL A., EIRHAFIKI T. and ZERAOULI Y. (2010) "Paraffin wax mixtures as phase change materials", *Solar Energy Materials and Solar Cells*, Vol.94, pp.2158-2165.
- LACROIX M. (1993) "Numerical simulation of a shell-and-tube: latent heat thermal energy storage unit", *Solar Energy*, Vol. 50, pp. 357-367.

LACROIX M. and DUONG T. (1998) "Experimental improvement of heat transfer in a latent heat thermal energy storage unit with embedded heat sources", *Energy Conversavation*, Vol. 39, pp. 703-716.

LANE GA (1983). *Solar heat storage:latent heat materials*, vol. I. Boca Raton, FL: CRC Press, Inc.

LEE T., HAWES D.W., BANU D. and FELDMAN D. (2000) "Control aspects of latent heat storage and recovery in concrete", *Solar Energy Materials and Solar Cells*, Vol.62, pp.217-237.

LIU Z., WANG Z., and MA C. (2006) "An experimental study on heat transfer characteristics of heat pipe heat exchanger with latent heat storage. Part I: Charging only and discharging only modes", *Energy conservation and management*, Vol. 47, pp.944-966.

MILLS A.F. and CHANG B.H. (2004) "Error analysis of experiments: a manual for engineering students", Los Angeles, California.

NEEPER D.A. (2000) "Thermal dynamics of wallboard with latent heat storage", *Solar Energy*, Vol. 68, pp. 393-403.

PASUPATHY A. and VELRAJ R. (2008) "Effect of double layer phase change material in building roof for year round thermal management", *Energy and Buildings*, Vol. 40, pp.193-203.

RADY M. (2009) "Granular phase change materials for thermal energy storage: Experiments and numerical simulations", *Applied Thermal Engineering*, Vol. 29, pp.3149-3159.

REGIN A.F., SOLANKI S.C. and SAINI J.S. (2008) "Heat transfer characteristics of thermal energy storage system using PCM capsules: A review", *Renewable and Sustainable Energy Reviews*, Vol. 12, pp. 2438-2458.

SAITOH T. and KATO K. (1993) "Experiment on melting in heat storage capsule with close contact and natural convection", *Experimental Thermal and Fluid Science*, Vol. 6, pp. 273-281.

SARI A. and KAYGUSUZ K. (2002) "Thermal and heat transfer characteristics in a latent heat storage system using lauric acid", *Energy Conversion and Management*, Vol. 43, pp. 2493-2507.

SARI A. and KAYGUSUZ K. (2003) "Some fatty acids used for latent heat storage: thermal stability and corrosion of metals with respect to thermal cycling", *Renewable Energy*, Vol.28, pp. 939-948.

SARI A. and KARAIPEKLI A. (2009) "Preparation, thermal properties and thermal reliability of palmitic acid/expanded graphite composite as form-stable PCM for thermal energy storage", *Solar Energy Materials and Solar Cells*, Vol. 93, pp. 571-576.

SARI A. and KARAIPEKLI A. (2001) "Thermal performance of myristic acid as a phase change material for energy storage application", *Renewable energy*, Vol. 24, pp. 303-317.

SARRIS I.E., LEKAKIS I. and VLACHOS N.S. (2004) “Natural convection in rectangular tanks heated locally from below”, *International Journal of Heat and Mass Transfer*, Vol. 47, pp. 3549-3563.

SHARMA A., TYAGI V.V., CHEN C.R., and BUDDHI D. (2009) “Review on thermal energy storage with phase change materials and applications”, *Renewable and sustainable energy reviews*, Vol. 13, pp.318-345.

SHMUELI H., ZISKIND G. and LETAN R. (2010) “Melting in a vertical cylindrical tube: Numerical investigation and comparison with experiments”, *International Journal of Heat and Mass Transfer*, Vol. 53, pp. 4082-4091.

STRITIH U. (2003) “Heat transfer enhancement in latent heat thermal storage system for buildings”, *Energy Buildings*, Vol. 35, pp. 1097-1104.

STRITIH U. and NOVAK P. (1996) “Solar heat storage wall for building ventilation”, *Renewable Energy*, Vol.8, pp.268-271.

TONG X, KHAN J.A. and AMIN M.R. (1996) “Enhancement of heat transfer by inserting a metal matrix into a phase change material”, *Numerical Heat Transfer*, Vol.30, pp. 125-141.

VELRAJ R., SEENIRAJ R.V., HAFNER B., FABER C. and SCHWARZER K.R. (1999) “Heat transfer enhancement in a latent heat storage system”, *Solar Energy*, Vol. 65, pp. 171-180.

VELRAJ R., SEENIRAJ R.V., HAFNER B., FABER C. and SCHWARZER K.R. (1997) “Experimental analysis and numerical modelling of inward solidification on a finned vertical tube for a latent heat storage unit”, *Solar Energy*, Vol.60, pp.281-290.

VEERAPPAN M., KALAISELVAM S., INIYAN S. and GOIC R. (2009) “Phase change characteristic study of spherical PCMs in solar energy storage”, *Solar Energy*, Vol.83, pp.1245-1252.

WANG Y., AMIRI A. and VAFAI K. (1999) “An experimental investigation of the melting process in a rectangular enclosure”, *International Journal of Heat and Mass Transfer*, Vol. 42, pp.3659-3672.

WEBB B.W. and VISKANTA R. (1986) “Natural-convection-dominated melting heat transfer in an inclined rectangular enclosure”, *International Journal of Heat and Mass Transfer*, Vol.29, pp.183-192.

WENG Y.C., CHO H.P., CHANG C.C. and CHEN S.L. (2010) “Heat pipe with PCM for electronic cooling”, *Applied Energy*, in press.

YAWS, C.L. (2003). *Yaws' Handbook of Thermodynamic and Physical Properties of Chemical Compounds*, Knovel.

YE H. and GE X.S. (2000) “Preparation of polyethylene–paraffin compound as a form-stable solid-liquid phase change material”, *Solar Energy Materials and Solar Cells*, Vol.64, pp.37-44.

ZALBA B., MARIN J.M., LUISA F., CABEZA B. and MEHLING H. (2003) "Review on thermal energy storage with phase change: materials, heat transfer analysis and applications", Applied Thermal Engineering, Vol. 23, pp. 251-283.

ZIVKOVIC B. and FUJI I. (2001) "An analysis of isothermal phase change of phase change material within rectangular and cylindrical containers", Solar Energy, Vol. 70, pp. 51-61.

ZHANG Z.G. and FANG X.M. (2006) "Study on paraffin/expanded graphite composite phase change thermal energy storage material", Energy Conversion and Management, Vol. 47, pp.303-310.

APPENDIX A Calibrations of Probe Thermocouples

Table A.1: Calibration results of 10°C bath temperature

No.	T _{bath} (°C)	Thermocouple reading of 5 repeatable tests					Maximum error (°C)
T10	10	9.85	9.79	9.80	9.82	9.78	0.22
T11	10	9.65	9.79	9.80	9.7431	9.76	0.35
T12	10	9.87	9.81	9.69	9.59	9.75	0.41
T13	10	9.66	9.68	9.69	9.74	9.71	0.32
T14	10	9.72	9.74	9.76	9.88	9.74	0.28
T15	10	9.88	9.93	9.92	9.90	9.83	0.17
T16	10	9.79	9.90	9.89	9.88	9.77	0.23
T ₁₅ -T ₁₆		0.09	0.03	0.03	0.02	0.06	0.09

Table A.2: Calibration results of 20°C bath temperature

No.	T _{bath} (°C)	Thermocouple reading of 5 repeatable tests					Maximum error (°C)
T10	20	19.88	19.84	19.81	19.75	19.81	0.25
T11	20	19.88	19.87	19.90	19.88	19.87	0.13
T12	20	19.78	19.79	19.80	19.81	19.75	0.25
T13	20	19.94	19.74	19.67	19.70	19.70	0.33
T14	20	19.92	19.89	19.90	19.89	19.82	0.18
T15	20	19.84	19.86	19.86	19.82	19.82	0.18
T16	20	19.77	19.75	19.79	19.80	19.73	0.27
T ₁₅ -T ₁₆		0.07	0.11	0.07	0.02	0.09	0.11

Table A.3 Calibration results of 30°C bath temperature

No.	T _{bath} (°C)	Thermocouple reading of 5 repeatable tests					Maximum error (°C)
T10	30	29.63	29.63	29.69	29.71	29.67	0.37
T11	30	29.75	29.78	29.84	29.88	29.79	0.25
T12	30	29.68	29.61	29.70	29.68	29.61	0.39
T13	30	29.73	29.77	29.82	29.75	29.71	0.29
T14	30	29.73	29.78	29.74	29.80	29.77	0.26
T15	30	29.95	29.89	29.73	29.82	29.73	0.27
T16	30	29.76	29.82	29.73	29.80	29.68	0.32
T ₁₅ -T ₁₆		0.19	0.07	0.00	0.02	0.05	0.19

Table A.4: Calibration results of 40°C bath temperature

No.	T _{bath} (°C)	Thermocouple reading of 5 repeatable tests					Maximum error (°C)
T10	40	39.59	39.61	39.65	39.60	39.67	0.41
T11	40	39.82	39.79	39.81	39.80	39.80	0.21
T12	40	39.67	39.68	39.62	39.67	39.68	0.38
T13	40	39.86	39.61	39.74	39.71	39.73	0.39
T14	40	39.79	39.78	39.71	39.77	39.80	0.29
T15	40	39.90	39.88	39.82	39.90	39.86	0.18
T16	40	39.78	39.81	39.80	39.85	39.81	0.22
T ₁₅ -T ₁₆		0.12	0.07	0.02	0.05	0.05	0.12

Table A.5: Calibration results of 50°C bath temperature

No.	T _{bath} (°C)	Thermocouple reading of 5 repeatable tests					Maximum error (°C)
T10	50	49.58	49.65	49.58	49.62	49.59	0.42
T11	50	49.80	49.66	49.78	49.63	49.78	0.37
T12	50	49.61	49.63	49.61	49.66	49.68	0.39
T13	50	49.83	49.93	49.86	49.86	49.77	0.23
T14	50	49.77	49.78	49.80	49.76	49.70	0.30
T15	50	49.92	49.87	49.89	49.78	49.78	0.22
T16	50	49.76	49.81	49.84	49.80	49.80	0.24
T ₁₅ -T ₁₆		0.16	0.06	0.05	-0.02	-0.0121	0.16

Table A.6: Calibration results of 60°C bath temperature

No.	T _{bath} (°C)	Thermocouple reading of 5 repeatable tests					Maximum error (°C)
T10	60	59.57	59.66	59.69	59.66	59.60	0.40
T11	60	59.69	59.66	59.74	59.72	59.70	0.34
T12	60	59.63	59.59	59.78	59.67	59.71	0.41
T13	60	59.71	59.69	59.75	59.80	59.74	0.31
T14	60	59.64	59.64	59.74	59.70	59.75	0.36
T15	60	59.77	59.93	59.91	59.99	59.83	0.23
T16	60	59.75	59.82	59.82	59.84	59.81	0.25
T ₁₅ -T ₁₆		0.02	0.11	0.09	0.15	0.02	0.15

APPENDIX B Flowmeter Electrical Circuit Connecting Diagram

In order to show how the turbine flow meter is connected to the LabView program, an electrical circuit is presented here. An impulse counter is used to measure the signal from the flowmeter.

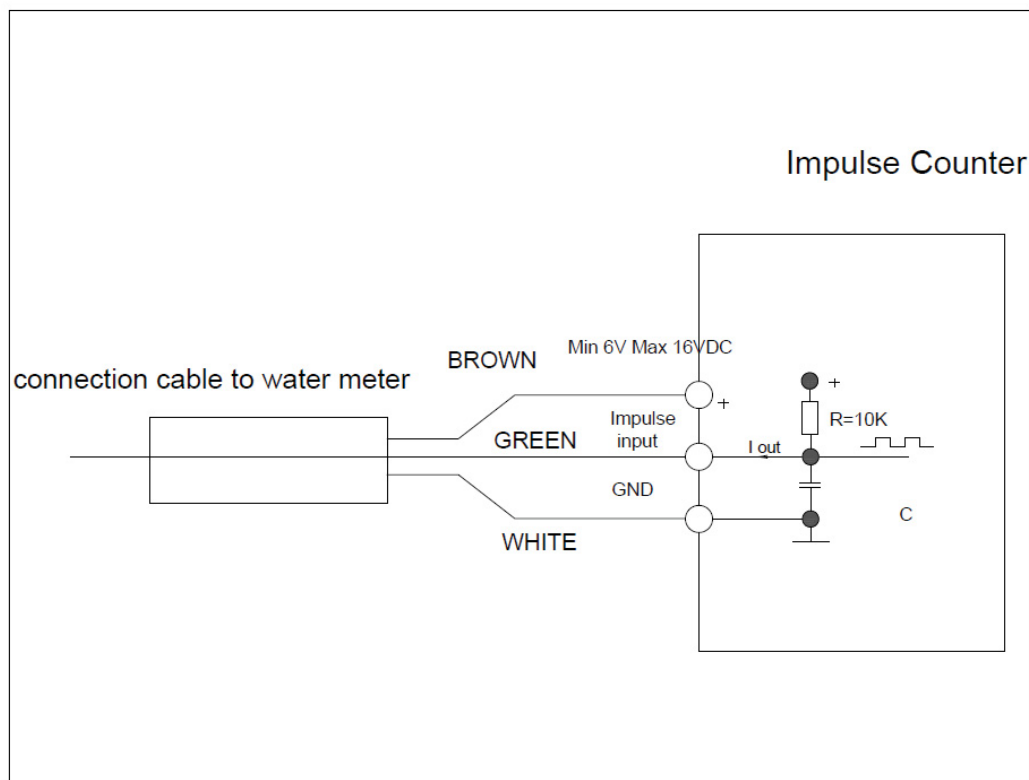


Figure B.1: Diagram of the electrical circuit connecting flowmeter to DAQ system

APPENDIX C Example of Experimental Uncertainty of Energy Stored

An example of experimental uncertainty calculation for energy stored during a test with a HTF inlet temperature of 60 °C and a flow rate of 1 L/min is shown here. During experimental tests, data is recorded every 30 seconds, so the calculation presented is based on the captured results for a 30 second interval.

So at $t = 1$ hour. The HTF inlet temperature was 61.177°C and outlet temperature was 60.195 °C. Therefore, temperature difference between water inlet and water outlet is calculated as

$$\Delta T = T_{inlet} - T_{outlet} = 61.177 - 60.195 = 0.982 \text{ }^{\circ}\text{C} \quad (\text{C.1})$$

As shown in the LabView, flow rate is 1 L/min (0.0167kg/s). The energy supplied during this 30 seconds is calculated as

$$Q = mc_p \Delta T = 0.0167 \times 30s \times 4.184 \times 0.982 = 2.05 \text{ kJ} \quad (\text{C.2})$$

As introduced in Chapter 2, the experimental uncertainty is calculated as

$$\dot{Q} = \dot{m}c_p(T_{in} - T_{out}) + u_{\dot{Q}} \quad (\text{C.3})$$

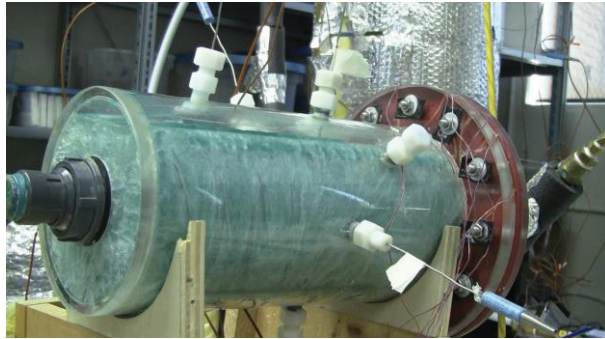
$$u_{\dot{Q}} = c_p \sqrt{\left(\frac{\partial \dot{Q}}{\partial \dot{m}} u_{\dot{m}}\right)^2 + \left(\frac{\partial \dot{Q}}{\partial T_{in}} u_{T_{in}}\right)^2 + \left(\frac{\partial \dot{Q}}{\partial T_{out}} u_{T_{out}}\right)^2} \quad (\text{C.4})$$

As mentioned before, the accuracy level of the turbine flow meter is 2%. From Table 2.3, it is shown that the maximum uncertainty of the probe thermocouple at water inlet is 0.27°C and 0.32°C for the water outlet. Then the experimental uncertainty is calculates as

$$u_{\dot{Q}} = 30s \times 4.184 \times \sqrt{(0.982 \times 0.0167 \times 0.02)^2 + (0.0167 \times 0.27)^2 + (0.0167 \times 0.32)^2} = 0.87 \text{ kJ} \quad (\text{C.5})$$

Giving an energy uncertainty of $0.87 \text{ kJ} / 2.05 \text{ kJ} = 42.4\%$.

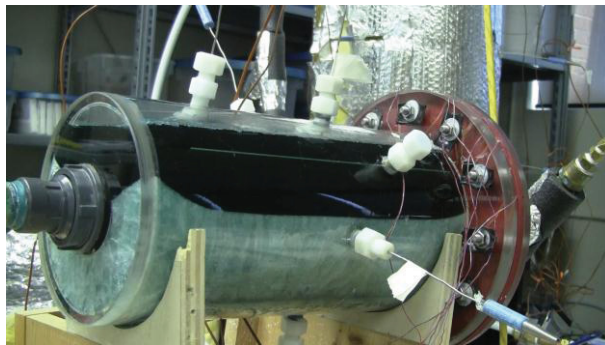
APPENDIX D Photographs of Charging and Discharging



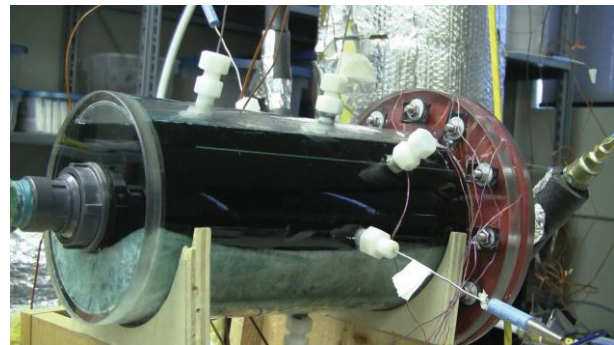
a) $t=0$ min



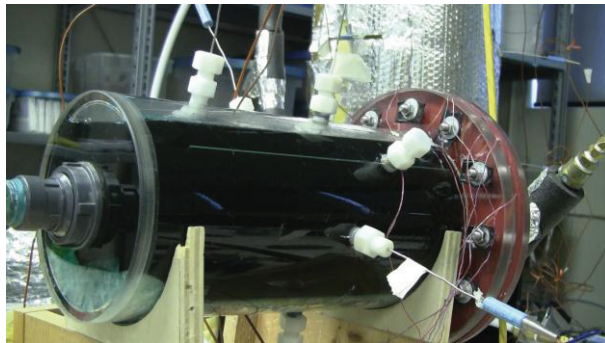
b) $t=60$ mins



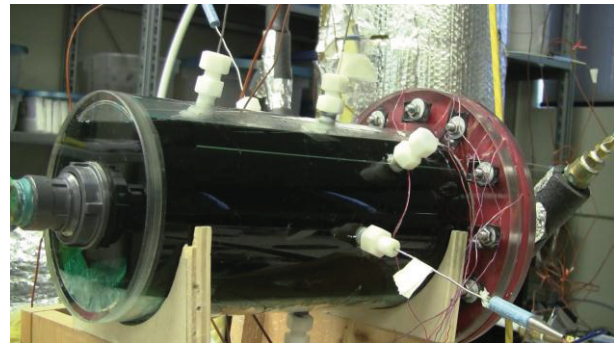
c) $t=120$ mins



d) $t=180$ mins

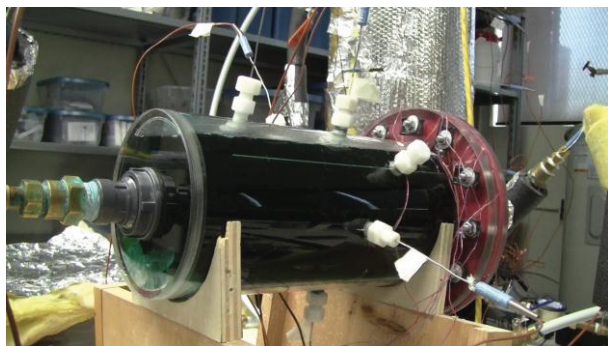


e) $t=240$ mins

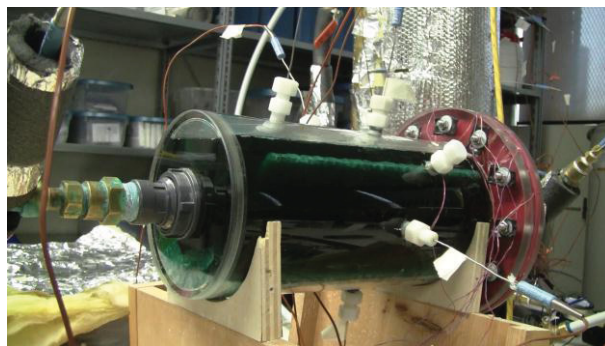


f) $t=300$ mins

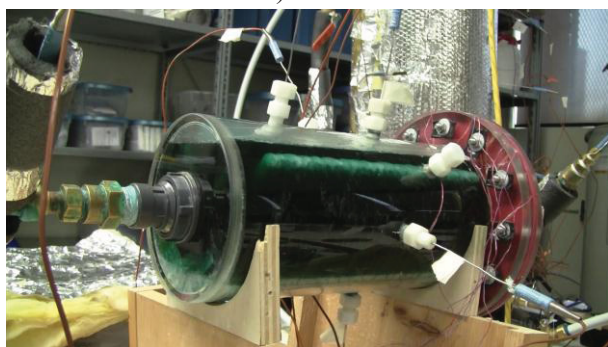
Figure D.1: Photos taken during charging with a HTF inlet temperature of 60°C and HTF flow rate of 5.5L/min



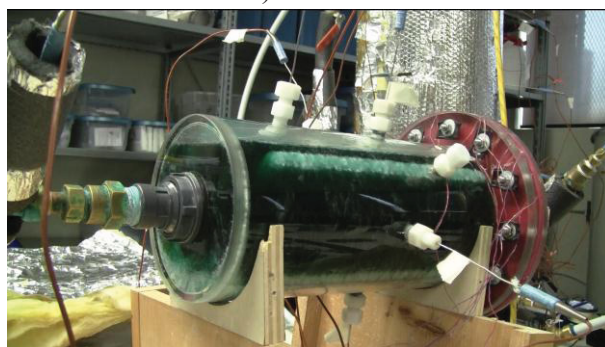
a) $t=0$ min



b) $t=30$ mins



c) $t=60$ min



d) $t=90$ mins



e) $t=120$ min



f) $t=150$ mins

Figure D.2: Photos taken during discharging with a HTF inlet temperature of 9°C and HTF flow rate of 13L/min



g) $t=180$ min



h) $t=210$ mins



i) $t=180$ min



j) $t=210$ mins

Figure D.3: Photos taken during discharging with a HTF inlet temperature of 9°C and HTF flow rate of 13L/min (continued)